NASA Technical Memorandum 104616

# Relative Elemental Abundance and Heating Constraints Determined for the Solar Corona From SERTS Measurements

**David A. Falconer**
*Universities Space Research Association*
*Greenbelt, Maryland*


National Aeronautics and
Space Administration

**Goddard Space Flight Center**
Greenbelt, Maryland 20771
**1994**

David Allen Falconer

Relative Elemental Abundance and Heating Constraints

Determined for the Solar Corona from SERTS Measurement

(under the direction of George Goldenbaum, and Joseph Davila

# ABSTRACT

Intensities of EUV spectral lines were measured as a function of radius off the solar limb by two flights of Goddard's Solar EUV Rocket Telescope and Spectrograph (SERTS) for three quiet sun regions. The density scale height, line-ratio densities, line-ratio temperatures, and emission measures were determined. The line-ratio temperature determined from the ionization balances of Arnaud and Rothenflug (1985) were more self-consistent than the line-ratio temperatures obtained from the values of Arnaud and Raymond (1992). Limits on the filling factor were determined from the emission measure and the line-ratio densities for all three regions.

The relative abundances of silicon, aluminum, and chromium to iron were determined. Results did agree with standard coronal relative elemental abundances for one observation, but did not agree for another. Aluminum was overabundant while silicon was underabundant.

Heating was required above 1.15 solar radii for all three regions studied. For two regions, local nonconductive heating is needed for any filling factor, and in all three regions for filling factor of 0.1.

# Contents

# List of Figures

# List of Tables

# List of Abbreviations

| Abbreviation | Meaning |
|---|---|
| CDS/NIS | Coronal Diagnostic Spectrometer/Normal Incidence Spectrometer |
| CDS/GIS | Coronal Diagnostic Spectrometer/Grazing Incidence Spectrometer |
| EUV | Extreme-ultraviolet light |
| FIP | First Ionization Potential |
| GSFC | Goddard Space Flight Center |
| IBAL1 | First Set of Ionization Balances |
| IBAL2 | Second Set of Ionization Balances |
| ISAS | Institute of Space and Astronautical Science |
| IR | Infrared |
| MSIS-86 | Mass Spectrometer and Incoherent Scatter |
| NASA | National Aeronautics and Space Administration |
| SEP | Solar Energetic Particles |
| SERTS | Solar Extreme-ultraviolet Rocket Telescope and Spectrograph |
| SOHO | Solar and Heliospheric Observatory |
| SOLEX | Solar X-rays |
| SURF-II | Synchrotron Ultraviolet Radiation Facility |

# Chapter 1

# Introduction

Unlike other stars, the Sun is close enough for us to spatially resolve its features. This allows us to do a more detailed comparison of measurement and modeling of the Sun than is possible with other stars. The study of the Sun involves a wide range of physics, including atomic physics, nuclear physics, and plasma physics, all of which are required to fully understand solar phenomena. Since a variety of conditions exist on the Sun which cannot be reproduced in a terrestrial laboratory, the Sun offers a unique opportunity to test theories for the corresponding physical processes [45]. A variety of interesting questions about the Sun are now being studied, including: the method by which energy is transferred outward from the convection zone into the upper solar atmosphere, the source and nature of variations in the solar wind, solar activity, flares, and variations of elemental abundances from region to region on the Sun.

The work in this dissertation is based upon analysis of data from the Solar Extreme-ultraviolet Rocket Telescope and Spectrograph (SERTS), an instrument built by members of the Solar Physics Branch of National Aeronautics and Space Administration (NASA)'s Goddard Space Flight Center (GSFC), and flown on sounding rockets in 1989 and 1991 [43, 55]. SERTS obtains in first order Extreme-ultraviolet (EUV) (250 Å to 450 Å) images and spectra of different regions of the Solar corona. From imaged spectra of the solar corona off the solar disk, the relative elemental abundance of, and heating constraints on, the observed corona have been determined.

Relative elemental abundances in the solar corona have, over the last decade, been found to differ from those in the photosphere. Recently, variations in relative elemental abundance from region to region in the corona have been shown to exist. These variations are important for several reasons, which include their effects on coronal diagnostics, and knowing them can lead to a better understanding of where the coronal material originates.

To put these results into context, we will first provide some general background information on the Sun. This will include a description of the general structure of the Sun and of features on the solar disk, as well as description of the methods with which some different parts of the electro-magnetic spectrum are used to study the Sun. We will also provide a more in-depth discussion of the solar corona.

## 1.1 Overview of Solar Structure

The Sun is not homogeneous, but instead contains many physically distinct regions. Each region will be discussed separately. The boundaries of these regions are somewhat arbitrary, but for the purpose of this dissertation the exact boundary locations are not important (Figure 1.1 for solar cross section [11]). To fully understand any one region, the effects on that region by other regions need to be understood. The following

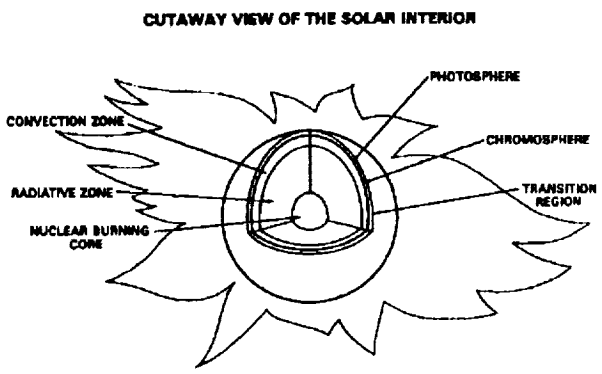


Figure 1.1. The solar cross section. Interior layers of the sun, with the solar corona in the background [11].

brief description of the principal solar regions is greatly expanded in a recent text by Stix [52]. See Appendix A for typical plasma parameters for photosphere, chromosphere, and corona and some useful equations.

The innermost solar region is the central core, where the energy output of the Sun is produced by the fusion of four hydrogen nuclei into a helium nucleus in a chain of reactions. The core density at Sun center is on the order of 100 $gm\ cm^{-3}$ and the temperature is more than $10^7\ K$. The core extends outward beyond the region of nuclear reactions, through a zone where energy is transferred radiatively by photons.

Above the core lies the convection zone, where the temperature has dropped sufficiently for recombination of helium and hydrogen to occur, increasing the plasma opacity. This, in turn, increases the temperature gradient, so convection instead of radiative heat transfer becomes the primary mode of energy transport. The convective motions produce a variety of waves which are transmitted upward out of this layer. Throughout this region, the temperature decreases with height from the order of several times $10^5\ K$ to less than $10^4\ K$, and the density decreases with height from 0.1 to 0.01 $gm\,cm^{-3}$. The solar magnetic field is believed to be generated at the base of this region, and then to rise and emerge from the visible solar surface.

The photosphere lies at the top of the convection zone. This is the part of the Sun which can be observed in visible wavelengths, since the optical depth has approached unity in the visible continuum. The majority of the Sun's energy that is radiated into space comes from this region. The motions of the convection zone can be detected in the photosphere in various oscillations and in turbulent granulation. Magnetic flux tubes appear to emerge in this region. These flux tubes do not emerge uniformly and are associated with different features seen on the Sun, such as active regions, coronal holes, and regions of the quiet Sun. The temperature continues to drop to a mean value of about 4500 $K$ at the uppermost part of this region with an atomic density of $10^{16} cm^{-3}$ or a mass density of $10^{-8} gm\ cm^{-3}$. However, observations of IR molecular lines of CO suggest that there may be a significant component of the upper photosphere at temperatures no greater than 3500 $K$ [5].

The chromosphere starts at the temperature minimum. The temperature in the chromosphere increases with radius to a few times $10^4\ K$, causing the region to produce the hydrogen Lyman alpha line emission in the uppermost part. This temperature rise requires that mechanical energy be transported to and deposited in the chromosphere, since the chromosphere cannot be heated from below by either radiation or thermal conduction. By definition, the chromosphere is hotter than most of the photosphere. The ultimate energy source for non-radiative heating in this region and the regions above is the convective motions in the photosphere [27, 12, 44]. The method by which this energy is transmitted and dissipated differs from region to region and is still being studied. The particle density varies from $10^{16}$ to $10^{10} cm^{-3}$ in the chromosphere.

The outermost region of the Sun's atmosphere is the corona, where the typical temperature is observed to vary from one to several times $10^6\ K$, and the electron density is between $10^7$ to $10^{10} cm^{-3}$ in nonflaring regions. The coronal

plasma is made up almost entirely of electrons and ions, as essentially all neutral atoms have been ionized. This region is probably heated by either waves propagating up the magnetic field lines, by local current dissipation, or by some combination of these two mechanisms, where plasma motions in the photosphere are the ultimate power source [57]. The magnetic field dominates the solar plasma at these heights with the plasma parameter "beta" (the plasma pressure divided by magnetic pressure) less than one. The corona extends outward until it merges into the solar wind. On large scales, and perhaps on smaller as well, spherical symmetry breaks down in the corona.

The corona and the solar wind have no sharp boundary. The plasma motion in the corona starts a mean upward flow in coronal holes and, to a lesser degree, over the magnetically "quiet" Sun. As the collective outward velocity increases the solar wind "begins", and at a few solar radii (depending on the underlying region) it becomes supersonic. This wind is known to affect the Earth's magnetosphere.

Between the corona and the chromosphere is the transition region, where the temperature increases from a few times $10^4$ $K$ to $10^6$ $K$ in the short distance of about 1000 km or less according to most models. There is evidence that the transition region temperature gradient is much less in coronal holes than elsewhere. The transition region is thought to be heated by energy conducted downwards from the more thermally conductive corona through the transition region, in which the thermal conductivity decreases downward because of the decrease in temperature. The lower temperatures cause the electron thermal conductivity to drop, since the mean-free-path of the cooled electrons is less. The effect of density on the thermal conductivity is small since density affects both the number of electrons conducting energy and the mean-free-path (See Appendix A for solar plasma parameters).

## 1.2 Features

The Sun's atmosphere is not homogeneous, but shows distinct features which manifest themselves in different ways in different atmospheric regions (Figure 1.2). Some of these are coronal holes, active regions, quiet regions, and polar plumes. The properties of many of these features are thought to be determined by magnetic fields. For further details than appear here, see again Stix [52].

Coronal holes are regions of unipolar, comparatively open magnetic flux tubes, which extend outward away from the Sun. They do not appear different from surrounding areas at photospheric and chromospheric heights. In the corona, however, they are dark in soft X-ray emission, because of lower temperatures and densities than other solar regions. Coronal holes exist at both poles and often extend north or south in bands. Coronal holes are known to be the source of high speed solar wind streams.

Active regions are regions with strong magnetic fields and closed loop flux tubes, which reconnect to another part of the solar surface. They are associated with photospheric sunspots, which are slightly cooler than the rest of the photosphere and emit less visible light. They extend into the the chromosphere and corona where they are brighter than the surrounding areas (hence have larger radiation losses). Transient phenomenon such as flares, which release great amounts of energy stored up in magnetic fields, occur in active regions. These regions contain the hottest coronal plasma.

The part of the Sun not covered by active regions or coronal holes is called the quiet Sun. Quiet Sun regions cover the majority of the Sun, and lie between the two extremes of active regions and coronal holes. However, there is an almost continuous range of smaller scale "activity" in the chromospheric network as one goes from very quiet Sun to the boundaries of active regions.

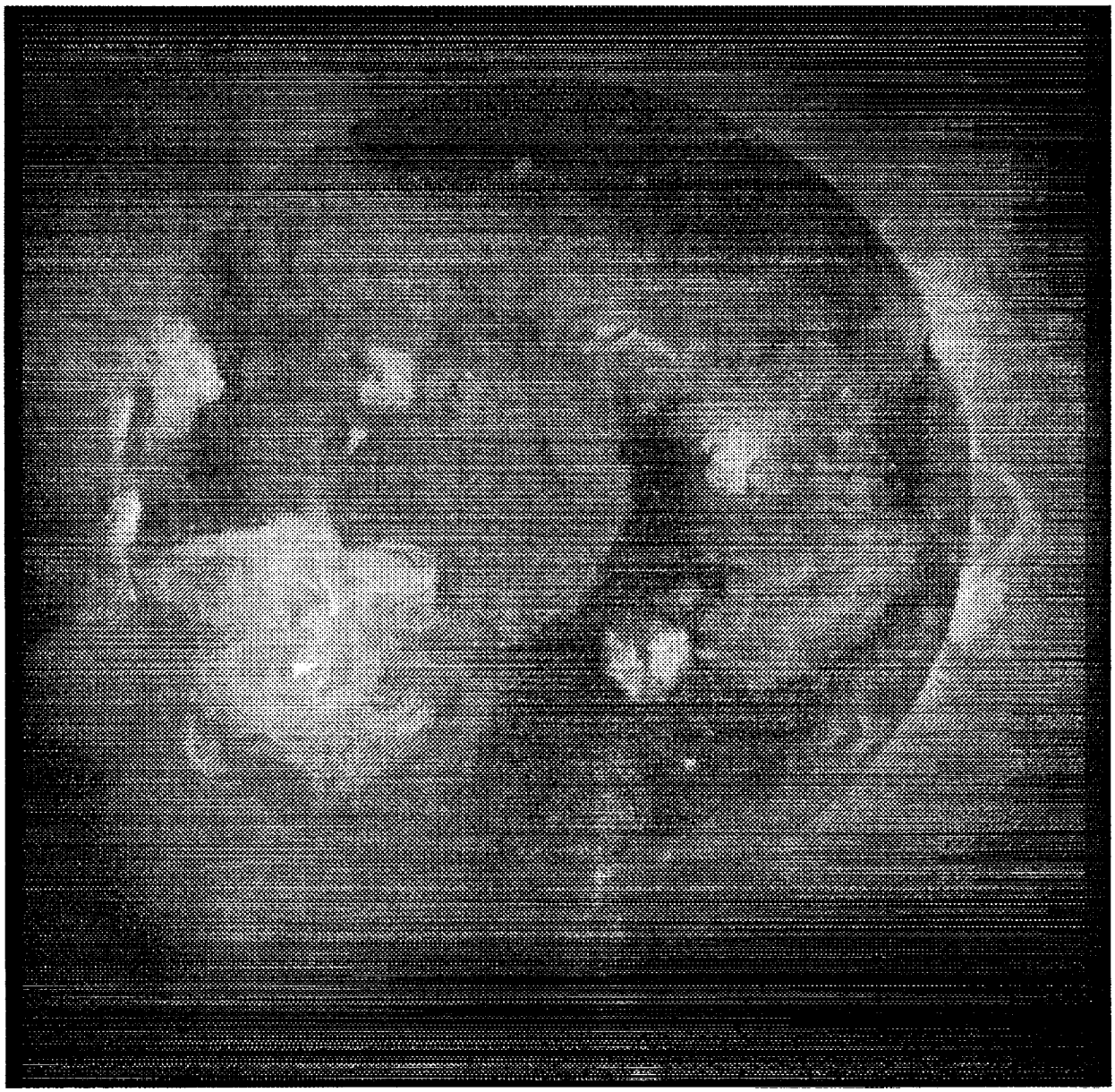

Figure 1.2. A Yohkoh X-ray image of the Sun taken on October 25, 1991. The dark regions at the poles and extending towards the equator are coronal holes. The bright region in the lower left-hand quadrant of the image is a bright active region while lesser active regions are scattered across the solar disk. The regions of intermediate brightness are quiet Sun. The quiet Sun shows structure. Loops are apparent off the solar limb.
The solar X-ray images are from the Yohkoh mission of ISAS, Japan. The Soft X-ray Telescope (SXT) was prepared by the Lockheed Palo Alto Research Laboratory, the National Astronomical Observatory of Japan, and the University of Tokyo with support of NASA and ISAS.

## 1.3 Solar Emission

The study of emission from the Sun includes observations over a wide range of the electromagnetic spectrum from radio waves to gamma rays, as well as measurements of solar wind particles. Because of the variations of emissivity and opacity with wavelength and temperature, different wavelength ranges allow observation of different parts of the solar atmosphere. The higher energy part of the electromagnetic spectrum can only be observed from space. Solar emission and many of the associated atomic processes are treated in detail in Zirin [63].

The Sun's photosphere emits most of the Sun's energy, and most of this emission is in the visible part of the electromagnetic spectrum. The visible spectrum is made up of a continuum and many absorption lines. The photosphere can also be observed and studied in the infrared, which is the way we observe the deepest depths of the photosphere. Magnetograms are made in the visible and infrared part of the spectrum to determine the magnetic fields of the solar photosphere.

The solar chromosphere was discovered by observing the Sun during solar eclipses, which occur when the solar disk is blocked by the Moon. The corona above the solar limb can be observed during solar eclipses as well. Coronagraphs are also used, which simulate a solar eclipse by blocking light from the solar disk using an occulting disk. The Sun's ultraviolet light output comes mainly from the chromosphere, with some ultraviolet emission coming from the transition region and the corona. Since this output is emission line dominated, the relative strengths of appropriately chosen lines can be used for density and temperature diagnostics, as will be discussed in Section 2.5.

When observed in the extreme-ultraviolet (EUV) the Sun emits a large number of optically thin spectral lines, which are produced at temperatures between several $10^4$ $K$ to $10^6$ $K$. Model calculations show that these lines are emitted in the upper chromosphere, the transition region, and the corona, although most are formed in the corona [52]. According to these models, each spectral line is preferentially produced at a different range of temperatures, so observations of many lines reveal information about different temperature regions of the atmosphere. Analysis of these spectral lines can be used to obtain the density and the temperature of the emitting plasma.

The corona emit in the radio range of the electromagnetic spectrum, and the corona is optically thick to radio waves. The background component of the quiet sun radiation comes from thermal emission [32]. As the wavelength increases, the height observed increases, since the plasma cutoff frequency increases with an increase in density. Thus, the cutoff wavelength decreases with an increase in density, so shorter wavelengths permit us to observe closer to the Sun where the density is higher. When EUV observations are compared to radio observations, additional insight is gained, since both are produced by the same plasma. For more discussion see Kundu [32].

The X-rays observed from the Sun come from the hotter regions of the solar corona around active regions and from flares. They can provide useful diagnostics of the hot solar corona to determine the temperature and structure of the emitting region. These measurements can also be compared to observations of other wavelengths to obtain a better understanding of active regions.

Gamma rays and hard X-rays are produced during solar flares and can be used as a diagnostic to study flares. These studies require either high time resolution or relatively high time and spatial resolution, in order to study solar flare development. Results obtained from these observations then can be used to constrain flare models.

Measurements of the solar wind from spacecraft which measure the mass, charge, and energy of detected particles provide much useful information. These observed elemental, isotopic, and ionization stage abundances of the solar wind provide constraints on models of solar wind ac-

celeration, because they can be used to indicate coronal abundances of the source regions for the wind.

## 1.4 Solar Corona

Two of the fields of study of the solar corona are heating and relative elemental abundance, which are the subjects of this dissertation. These two subjects will be introduced in this section. The general coronal magnetic field structure will also be discussed.

### 1.4.1 Heating

Since the corona is hotter than the chromosphere and transition region, heat is conducted downward towards the Sun's surface. Since energy is also radiated away by the solar corona, mechanical or magnetic field energy must be dissipated there in order to balance the radiative and conductive losses. The ultimate source of this energy is probably the convective motions in the photosphere, but the method by which this energy is transmitted into the corona and then dissipated has not been determined. The two primary models are (1) the dissipation of waves propagated along the coronal magnetic field lines, or (2) the dissipation of currents conducted along these field lines. A variety of hybrid models also exist. See Zirker [62] for a recent survey of coronal heating theories, and the conditions a successful theory must satisfy.

The coronal structure is controlled by the magnetic field topology with the plasma density and temperature determined by the amount of energy deposited in the structure. If, in a given coronal structure, additional energy is deposited, the temperature will rise causing the temperature gradient to increase, which will lead in turn to an increase in the conducted heat flux to the transition region. This will cause additional plasma to be heated and rise into the corona, increasing the coronal density in the structure. When less energy is deposited into a coronal structure, the plasma will cool radiatively and will sink, thus removing plasma from the coronal structure whose density will then decrease.

Where the energy is deposited determines the position of the temperature maximum in the solar corona, and, as discussed earlier, the coronal density and temperature gradient. Constraints on coronal heating from observed densities and temperatures are determined from SERTS data in Section 5.2.

### 1.4.2 Elemental Abundance Variation

The following brief description of relative elemental abundance is discussed in more detail in Section 2.5.4 and by Meyer [39]. During the last few years the elemental composition of the corona has been determined to differ from that of the photosphere. This variation seems to be in the direction of an enhancement of elements with low first ionization potential (FIP) compared to elements with high FIP. High FIP elements are found toward the right and top of the periodic table. This abundance variation is probably due to the fact that at temperatures around $10^4$K the low FIP elements are ionized, while most high FIP elements are neutral atoms.

Recent evidence indicates a variation in the enhancement factor depending on the solar feature, with the highest enhancement factor of about 10 in polar plumes found in polar coronal holes [59, 60]. This would indicate that the mechanism (or mechanisms) causing the enhancement depend on local conditions of the coronal plasma source sites to bring material into the corona. These variations could then be used as an indicator of underlying processes in the lower chromosphere, where the temperature is low enough for the elements with high FIP to be neutral.

These variations show that care must be taken with coronal diagnostics that assume fixed elemental abundance ratios, since elemental abundance can vary. Coronal diagnostics using the

same element are more reliable for this reason.

### 1.4.3 Magnetic Field Structures

The magnetic field dominates the coronal structure for the following reasons. First, as mentioned earlier, energy is transmitted by waves or currents along the magnetic field and deposited into the corona. Second, electron heat conduction dominates the conductive flux in the corona, therefore heat is preferentially conducted along the magnetic field lines. Third, the plasma is frozen in and travels along the magnetic field lines, so that each set of flux tubes is fed plasma independently, usually from lower regions of the Sun. Fourth, the magnetic pressure is usually much larger than the plasma pressure in the corona, so that different plasma densities in adjacent flux tubes are possible. For a more in-depth discussion than is given here, see Giovanelli [24].

The magnetic flux tubes come in two types: open and closed flux tubes. Some of these flux tubes return to the surface of the Sun in closed loops and are called closed flux tubes. So called open flux tubes exist when the magnetic field extends outward into the solar wind. These flux tubes are dragged outward by the wind.

Some flux tubes may have a coronal plasma density much lower than average, or at the wrong temperature to emit in the observed wavelength band. This situation could occur if energy is not being deposited into a flux tube so the coronal plasma cools radiatively and drains out of the tube, or if the coronal plasma temperature increases too much.

While the magnetic field dominates the corona on a small size scale, most of these variations exist on scales smaller than the scale size of the SERTS observations. This causes the corona to appear to vary smoothly in our results, with only one large-scale loop observed, which will be discussed in later sections. This has given rise to the concept of filling factor, which is the fraction of the volume filled with observed coronal plasma.

## 1.5 Outline of Dissertation

This dissertation consists of six chapters. Chapter 1 is a general introduction to the Sun, and to the solar corona in particular. Next, the theoretical tools from solar physics are reviewed, which will be used to convert the observed relative spectral line intensities into derived coronal properties. The third chapter describes the SERTS instrument and calibration of the instrument. Next comes the analysis chapter where the observed coronal density, temperature, emission measure and elemental abundance are determined, using the tools developed in the second chapter. In Chapter 5 the filling factor and heating constraints are determined from the coronal properties determined in Chapter 4. The assumption of a Maxwellian electron distribution is examined in Chapter 6. Finally, the conclusions are given in the Chapter 7.

## 1.6 Acknowledgment

I thank my advisors, Professor George Goldenbaum and Dr. Joe Davila for their guidance and help. Professor George Goldenbaum's questions led me to a deeper understanding of the research. Dr. Joe Davila supported my research with NASA funding (879-11-38) and offered useful insights into different ways of looking at the research problems encountered, especially concerning coronal heating. He also showed me by personal example and suggestions better ways to present my research to others. I am also grateful to the members of the Advisory Committee for their time and suggestions on the dissertation.

I gratefully acknowledge the following people. Dr. Roger Thomas also supported my research with NASA funding (170-38-52). The many discussions with him on spectroscopy and the SERTS instrument helped tremendously. Dr. Stuart Jordan, provided advice and insights into my research, and on ways to present the results in both talks and this dissertation. My discussions

on relative elemental abundance with Dr. Julia Saba helped me develop a better understanding of the present knowledge of this important subject. She also providing many other suggestions for improving the dissertation.

I thank Drs. Bill Thompson and Jeff Brosius who answered many general SERTS, and computer questions, and Dr. Werner Neupert for explaining the history of the SERTS instrument. Dr. Anand Bahtia helped with understanding the atomic physics.

I also thank Drs. Brunella Monsignori-Fossi, Ken Widing, Uri Feldman, George Doschek, Spiro Antiochos, Monique Arnaud, and Francis Keenan who all answered my questions concerning their area of research.

Finally, I thank everyone who read parts of my dissertation and suggested ways to improve it, including many of the people mentioned in this Acknowledgment and Drs. Ed Stanford and Wilbur Affens.

# Chapter 2

# Theory

This chapter will review the theoretical tools used to analyze the data and develop the coronal models used and discussed in later chapters. In the first section we will discuss the density scale height and how this can be related to temperature under certain conditions. We also provide here a more in-depth discussion of the elemental composition than in the introductory chapter. In the second section the primary emission mechanism, collisional excitation of the observed lines, is discussed, along with the general physics involved in calculating the spectral line emission so that the reader can better understand how we do the calculation. Tabulated values are used where more accurate calculations have been done. In the third section, the equation for the observed spectral line intensity is determined by integrating along the line of sight, assuming a hydrostatic atmosphere with a known scale height. The intensity is a function of several different parameters such as the electron temperature, electron density, and the elemental abundance. Methods of obtaining these different parameters from ratios of spectral line intensities are then reviewed in the fourth section. This chapter then concludes with a discussion of the effect of variation of line emissivity on scale height.

## 2.1 Density Scale Height and the Scale-height Temperature

From SERTS observations, the emission from the solar corona is observed to decrease exponentially with height above the solar limb. This leads to the possibility of determining the corona density scale height. The experimentally determined scale height can be related to a theoretical parameter called "the scale-height temperature", if we assume hydrostatic conditions as discussed in this section.

The following derivation of a hydrostatic atmosphere is done in spherical geometry. In a hydrostatic atmosphere the net force is zero, so the force due to gravity on a unit volume must be balanced by the change of pressure on that volume. Neglecting radial magnetic forces and assuming spherical symmetry, we can write

$$\rho g A dr = -A dP, \tag{2.1}$$

where $\rho$ is the mass density of the gas, $A$ is the area, $r$ is the radius, $dP$ is the change in pressure, and $g$ is the gravitational acceleration. For the Sun $g$ is

$$g = GM_{\odot}/r^2, \tag{2.2}$$

where $G$ is the universal constant of gravity and $M_{\odot}$ is the solar mass. Assuming the ideal gas approximation.

$$P = \rho kT/\mu, \tag{2.3}$$

where $\mu$ is the average atomic weight of the plasma, $k$ is the Boltzmann constant, and $T$ is the temperature, we get

$$\frac{-R_\odot^2 dr}{r^2 H_s(T)} = \frac{d\rho}{\rho} + \frac{dT}{T}, \tag{2.4}$$

where

$$H_s(T) = \frac{R_\odot^2 kT}{\mu G M_\odot} \tag{2.5}$$

is called the density scale height and has units of length, $R_\odot$ is the solar radius. Using

$$dT = \frac{dT}{dr} dr, \tag{2.6}$$

we can integrate from a reference radius $r_o$ to get

$$-\int_{r_o}^{r} \left( \frac{R_\odot^2}{H_s(T)} + \frac{r^2 \frac{dT}{dr}}{T} \right) \frac{dr}{r^2} = ln(\frac{\rho}{\rho(r_o)}), \tag{2.7}$$

where $\rho_o$ is the density at $r_o$.

For an isothermal atmosphere $\frac{dT}{dr} = 0$ so, the expression simplifies to

$$\rho = \rho(r_o)\, exp\left[ \frac{-R_\odot^2}{H_s(T_0)} \left( \frac{1}{r_0} - \frac{1}{r} \right) \right]. \tag{2.8}$$

Equation 2.8 in the limit of $r_o$ going to infinity becomes the expression for the standard plane-parallel atmosphere. Guhathakurta et al. [25] uses the same equation. Since

$$\rho = N_e \mu, \tag{2.9}$$

where $N_e$ is the electron density we have

$$N_e = N_e(r_0)\, exp\left[ \frac{-R_\odot^2}{H_s(T_0)} \left( \frac{1}{r_0} - \frac{1}{r} \right) \right]. \tag{2.10}$$

For the nonisothermal case, we derived the approximate relationship

$$\rho \cong \rho_0\, exp\left[ \frac{-R_\odot^2}{H_s'} \left( \frac{1}{r_0} - \frac{1}{r} \right) \right], \tag{2.11}$$

where the effective scale height, $H_s'$, is defined as

$$\frac{1}{H_s'} = \frac{T_0}{H_s(T_0)T} + \frac{r^2 \frac{dT}{dr}}{R_\odot^2 T}, \tag{2.12}$$

and the $H_s'$ radial dependence is assumed small over the distance of interest. For the observed conditions reported here (which will be discussed in Section 4.4), this effect would be less than 5%.

The analysis described above assumes that the only change in the total pressure is due to the change in the gas pressure. This may be invalid if, for example, either the gradient of the magnetic pressure or turbulence is important. Then the hydrostatic scale height would be larger than the effective scale height and we obtained

$$\frac{1}{H_s'} = \frac{T_0}{H_s(T_0)T} + \frac{r^2 \frac{dT}{dr}}{R_\odot^2 T} + \frac{r^2 \mu}{R_\odot^2 \rho k T} \frac{dP}{dr}. \tag{2.13}$$

The effective scale height depends weakly on $r$, but for the purpose of this dissertation this effect can be neglected. The scale height temperature is determined from the effective scale height by

$$T_s = \frac{R_\odot^2 k H_s'}{\mu G M_\odot}, \tag{2.14}$$

where $H_s'$ is determined from the radial dependence of the intensity. Even if the scale-height temperature differs from the electron temperature, the density scale height is still useful in modeling the solar corona to obtain other parameters. The validity of the various assumptions to the observations will be discussed in Section 4.4.4.

## 2.2 Coronal Elemental Composition

During the last decade it was discovered that the coronal elemental composition often differs from the photospheric composition [37]. This difference has been determined from both solar wind particle measurements and emission line observations. Since, in Section 4.6, the relative elemental abundance will be determined, some background on the present theories for variations in the relative elemental abundance needs to be discussed, along with other sets of observations. Attempts

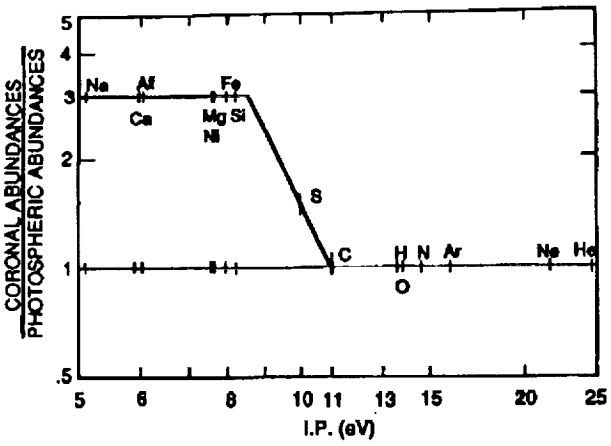


Figure 2.1. A schematic representation of the coronal elemental abundance divided by the photospheric elemental abundance, illustrating the difference between high FIP elements and low FIP elements. (After Feldman 1992 ...)[17]

to determine the nature of these differences and their causes continue.

The elemental abundance variation seems to depend most strongly on the first ionization potential (FIP) of the element. In Figure 2.1 taken from Feldman [18] the coronal relative elemental abundance compared to the photospheric abundance is shown. A "step" function is observed with the low FIP elements ($< 10eV$) enhanced compared to the high FIP elements ($> 11eV$). The size of the step is the enhancement factor which is found to be in the range of 3-5 [17, 38, 40]. The elements S and P, with FIPs intermediate between the low FIP and high FIP elements, show an intermediate enhancement factor. Very low FIP elements ($< 6.1eV$) can have an even greater enhancement factor than the "normal" low FIP elements [16, 46, 15].

The situation regarding hydrogen is still open to debate. Since it is the most abundant element on the Sun, it might act differently. The hydrogen FIP, and only ionization potential, is 13.6 eV, which would make it a high FIP element. Since, at coronal temperatures hydrogen, is completely ionized, direct measurements are difficult. Initial work suggested hydrogen acted as a low FIP element [58]. More recent work has suggested that hydrogen probably acts as a high FIP element (see discussion by Meyer [39]), or at least somewhere in between (Fludra and Schmelz [19]). In this dissertation, we determined the ratio of the elements abundance to iron, since only low FIP elements are used and most of the spectral lines observed by SERTS come from iron. The plots and figures use Meyer's 1985 [38] elemental abundance, which treats hydrogen as a low FIP element.

The enhancement factor of the low FIP to high FIP elements seems to vary with observation and the region of the corona. The enhancement factor can be as large as 10 for polar plumes [59, 60] and as small as unity [48, 34]; in the quiet Sun upper atmosphere it is approximately 4. An enhancement factor of approximately 4.5 is used by Meyer 1993 [39] to define his reference set of "coronal" abundances. Elemental abundances in active regions seem to vary between Meyer coronal and photospheric composition, according to Saba and Strong [48] and McKenzie and Feldman [34]. Feldman also reports that in plumes and impulsive flares, elements with very low FIP show a factor of 2 increase over other low FIP elements [17].

These variations suggest that a mechanism exists whereby the enhancement factor could vary, depending on the conditions described below, from one solar region or feature to another. Another possibility is that there may be two or more mechanisms for obtaining coronal plasma from the photospheric plasma, one of them with low FIP/high FIP enhancement and a second which brings up less differentiated or undifferentiated plasma into the corona.

One general mechanism to produce the FIP bias effect requires the temperature of the source of plasma to be less than $10^4K$ and not be subjected to intense UV and X-ray radiation. Generally, this condition is met in the chromosphere, photosphere, and possibly in spicules according to Meyer [39]. In this case, the low FIP elements

would be ionized and affected by electromagnetic forces while the high FIP elements would be neutral and not directly affected. Hence, partial separation of neutral atoms from ions can occur. Then this ion rich plasma is preferentially transported upwards so that the corona is enriched in low FIP elements.

Photospheric abundances could be produced in the corona by a rapid heating event such as occurs during flares. In this case, the photospheric plasma is heated and raised into the corona before the ions have time to separate from the neutral atoms, so no enrichment of the low FIP elements has taken place. This would just raise photospheric plasma into the corona and heat it to coronal temperatures.

Photoionization could also affect the relative elemental abundance of some elements such as neon. A proposed mechanism is that X-ray radiation produced in the corona penetrates to the coronal plasma source site and ionizes neon atoms which have a larger ionization cross section than the oxygen atoms. McKenzie and Feldman [34] report that the relative elemental abundance of high FIP elements, oxygen and neon, could vary in active regions and flares. Schmelz [50] reported enhancement of neon relative to oxygen for certain flares. If photoionization is important, then some high FIP elements will sometimes act as low FIP elements.

Sometimes, the relative elemental abundances of low FIP elements have also been observed to vary. The variation in low FIP elements Mg (7.646 ev) and Fe ( 7.87ev) found by McKenzie and Feldman [34] in P78-1 SOLEX data was less than the uncertainties of measurement, but an upper limit of 1.5 was placed on the variation. On the other hand, Saba and Strong [48] found possible variations in Fe:Mg of about a factor of 3 using Solar Maximum Mission data. These two studies had a number of differences, and the meaning of these results has yet to be firmly established.

In solar wind data, according to Meyer 1985 [37], the elemental composition of solar energetic particles (SEP) is highly variable from event to event. This effect might result from some acceleration mechanism of the solar wind, or it might be because of the mechanism responsible for the coronal composition.

The results reported in this dissertation indicate that there is a FIP dependence of the enhancement, but not as a simple "step" function. This will be shown in Section 4.6.

## 2.3 The Atomic Physics of Coronal Emission Lines

A variety of solar coronal properties such as plasma density, temperature, and relative elemental abundance can be determined if enough emission lines are available and the emission line formation processes are known. In the extreme ultraviolet (EUV) most of the emission lines are produced by collisional excitation, while others result from photoionization followed by recombination or charge exchange. The latter processes are negligible for most of the cases considered here, however.

Resonance scattering or photoexcitation occurs when a photon excites an ion which then rapidly decays, emitting another photon at the same wavelength but possibly in another direction; this mechanism is discussed in detail by Gabriel [22] and Nakada [42], and can be as important as electron collision excitation for sufficiently low densities or an especially intense background source. If emission is resonance scattered, the observed spectral line intensity will be affected.

At the heights in the solar corona discussed here the corona is optically thin, so radiation emitted directly towards the observer will probably not be affected by absorption and scattering. However, since some of our observed lines are more intense nearer the Sun than at the height of our observations, resonance scattering towards the observed can at least in principle be significant in those cases. This effect is most important

relative to emission from collisional excitation at larger radii where the electron density is low, since emissions because of the electron collisional excitation (discussed next) vary as the density squared, while resonance scattering is proportional to the first power of the density.

**Some Comments on Notation**

Before the derivation of the spectral line intensity from electron collisional excitation, the general notation used to indicate the spectral line or atomic energy level in question needs to be introduced. Since this dissertation compares lines from different elements, ionization stages, levels of excitation, and radial positions, the notation needs up to four subscripts. An example of the notation is given by $E_{Fe,XV,5,1}$, where $E$ indicates the energy per photon, Fe is the element, XV is the ionization stage minus one, 5 denotes the initial level and 1 the ground state that the ion de-excites to. The general case of an arbitrary emission line produced by an arbitrary transition in an arbitrary element would be written $E_{X,Z,i,j}$ where $X$ is the element and $Z$ is the ionization stage minus one. Densities are specified with three subscripts or less, for example with $N_{Fe,XV,5}(r)$ indicating the volume density of Fe XV in the fifth excitation level at radius $r$. The density of an element in a particular ionization stage, summed over all excitation levels will be $N_{X,Z}$, where

$$N_{X,Z} = \sum_j N_{X,Z,j}. \qquad (2.15)$$

Finally, radial position is denoted in the common way as an argument in parenthesis. For example $N_X(r)$ is the volume density of element X at radius r.

Electron collisional excitation occurs when an electron hits an ion with sufficient kinetic energy to move one of the ion's electrons into an excited level. Later the electron will de-excite radiatively to either its ground level or to another lower level. This process will produce a photon at a specific energy, giving rise to an emission line. The emission rate per unit volume, $\epsilon$, of the transition is

$$\epsilon_{X,Z,i,j} = E_{X,Z,i,j} N_{X,Z,i} A_{X,Z,i,j}, \qquad (2.16)$$

where $E$ is the energy per photon, $N$ is density of the emitter, and $A$ is the Einstein spontaneous emission rate ($s^{-1}$).

Equation (2.16) can be rewritten to separate the terms which are dependent on the specific line observed and those which depend only on the physical conditions of the emitting plasma, as

$$\epsilon_{X,Z,i,j} = Q_{X,Z,i,j}(T_e, N_e) \frac{N_X}{N_e} N_e^2, \qquad (2.17)$$

where $Q_{X,Z,i,j}(T_e, N_e)$ is called the contribution function which is determined theoretically. It is strongly dependent on $T_e$ and normally weakly dependent on $N_e$, and is defined as

$$Q_{X,Z,i,j}(T_e, N_e) = \left[\frac{N_{X,Z}(T_e)}{N_X}\right] \times \left[\frac{E_{X,Z,i,j} A_{X,Z,i,j}}{N_e} \frac{N_{X,Z,i}(T_e, N_e)}{N_{X,Z}}\right], \qquad (2.18)$$

where $T_e$ and $N_e$ are the electron temperature and density. The expression inside the second bracket of Equation 2.18 is the emission per ion, while the expression inside the first bracket is the ionization fraction. In the low density limit, the emission per ion is not dependent on $N_e$, as will be shown in Equation 2.24. Often $Q$ is just a function of $T_e$ for some spectral lines. The contribution functions for many lines have been calculated by Mewe [35] and Landini and Monsignori-Fossi [41]. These authors usually present their calculations using an assumed set of elemental abundances, which replaces $Q_{X,Z,i,j}(N_X/N_e)$ in Equation (2.17). They assume a single temperature and a Maxwellian electron distribution in their calculations. The Landini and Monsignori-Fossi [41] set of calculations give both density and temperature dependence.

To understand the underlying physics in determining the contribution function, the general method of calculating it is given in Sections 2.3.1 and 2.3.2. Section 2.3.1 discusses how to obtain

the emission per ion, and Section 2.3.2 the ionization fraction. These two calculations are normally done separately and often by different research groups, because the rates that affect the emission per ion are fast compared to the rates affecting the ionization fraction in the "coronal approximation", where the two factors can be decoupled.

### 2.3.1 Collisional Excitation of Coronal Ions

The second part of the the contribution function of equation (2.18) is the emission per ion. This is dependent on the rate the excited level is filled, the rate at which electrons decay from the excited level to produce the emission line of interest, and the energy per photon as shown in this section. For more details, see Landini and Monsignori-Fossi [33] and Gabriel and Jordan [23]. As mentioned earlier, calculations for different emission lines can be found in the literature [35, 33]. Since the excitation and de-excitation rates occur on time scales of less than a second, the effect of transportation of ions from one region to another is negligible.

Any excited level can be populated by collisional excitation from lower levels, by radiative decays from higher levels, or by collisional de-excitation from higher ionization stage (charge exchange has negligible effects in the solar corona on the population of the excited level). The excited level can be depopulated by collisional excitation, by collisional de-excitation, and by radiative decay to lower levels. If the ionization rate and recombination rate (which change the ionization state and will be discussed later) are slow compared to the radiative and collision rates, the rate of change of the excited level is

$$\frac{dN_{X,Z,i}}{dt} = N_e \sum_{j \neq i} N_{X,Z,j} C_{j,i} - N_e N_{X,Z,i} \sum_{j \neq i} C_{i,j} + \sum_{j>i} N_{X,Z,j} A_{X,Z,j,i} - N_{X,Z,i} \sum_{j<i} A_{X,Z,i,j}, \quad (2.19)$$

where the ground state is given by $j = 1$, and $C_{i,j}$ is the electron collision excitation rate ($cm^3\ s^{-1}$). The electron collision excitation rate coefficient is given by Kato [28] as

$$C_{i,j} = \frac{8.63 \times 10^{-6} exp(-E_{X,Z,i,j}/kT_e)}{\omega_i \sqrt{T_e}} \overline{\gamma_{j,i}}, \quad (2.20)$$

where $i > j$, and $\overline{\gamma_{j,i}}$ is the effective collision strength, which can be calculated quantum mechanically and is symmetric with respect to exchange between $i$ and $j$. By the law of detailed balance, an equilibrium argument, the rate of transitions from level $i$ to level $j$ because of the excitation must be equal to the rate of de-excitation of level $j$ to level $i$ [10, 6],

$$\omega_j exp(-E_{X,Z,j}/kT_e) C_{j,i} = \omega_i exp(-E_{X,Z,i}/kT_e) C_{i,j}, \quad (2.21)$$

where $\omega_j$ is the statistical weight of the ground level, $E_{X,Z,i}$ and $E_{X,Z,j}$ are the energies of the two levels, and the collisional de-excitation rate coefficient can be written

$$C_{j,i} = \frac{8.63 \times 10^{-6}}{\omega_j \sqrt{T_e}} \overline{\gamma_{j,i}}, \quad (2.22)$$

where $i > j$.

For a steady state plasma, where $\frac{dN_{X,Z,i}}{dt} = 0$, Equation (2.19) becomes

$$N_{X,Z,i}(T_e, N_e) = \frac{N_e \sum_{j \neq i} N_{X,Z,j} C_{j,i}(T_e) + \sum_{j>i} N_{X,Z,j} A_{X,Z,j,i}}{N_e \sum_{j \neq i} C_{i,j}(T_e) + \sum_{j<i} A_{X,Z,i,j}}. \quad (2.23)$$

To obtain a closed set of equations we include Equation (2.15).

For a low electron density plasma, the first term of the numerator and the second term of the denominator dominate, with the primary source of excitation being from the ground level $j = 1$ and with the ground level population being near

unity. Then Equation (2.24) reduces to what is called the coronal approximation

$$N_{X,Z,i} = \frac{N_e C_{1,i} N_{X,Z}}{\sum_{j<i} A_{X,Z,i,j}}. \quad (2.24)$$

From this, the contribution function from Equation (2.18) becomes

$$Q_{X,Z,i,j} = [E_{X,Z,i,j} C_{1i} b_{X,Z,i,j}] \left[\frac{N_{X,Z}}{N_X}\right], \quad (2.25)$$

where $b_{X,Z,i,j}$ is the branching ratio

$$b_{X,Z,i,j} = \frac{A_{X,Z,i,j}}{\sum_{k<i} A_{X,Z,ik}}. \quad (2.26)$$

This is the usual approximation used to calculate the intensity of a line.

### 2.3.2 Ionization Balance

The next step in determining the contribution function is evaluating the ionization fraction, i.e., the first expression in brackets in equations (2.18) or (2.25), which is the fraction of an element in a particular ionization state. These calculations assume an equilibrium situation and are described in more detail by Arnaud and Rothenflug [3].

Since it is rare for an ion to doubly ionize or doubly recombine in one step under normal coronal conditions, the ion density is strongly dependent on the adjacent ion densities, with the rate of change being

$$\frac{dN_{X,Z}}{dt} = N_e(N_{X,Z-1} q_{X,Z-1} + N_{X,Z+1} \alpha_{X,Z+1} - N_{X,Z} q_{X,Z} - N_{X,Z} \alpha_{X,Z}), \quad (2.27)$$

where $q_{X,Z}$ is the ionization rate coefficient which is the sum of the direct ionization rate coefficient and the autoionization rate coefficient, and $\alpha_{X,Z}$ is the sum of the radiative recombination rate coefficients and dielectronic rate coefficients, both of which depend on electron temperature. (Radiative recombination dominates three body recombination at densities less than $10^{20} cm^{-3}$ and temperatures greater than $10^6$K [10].) As before, the plasma is assumed to be in steady state, so $\frac{dN_{X,Z}}{dt} = 0$, giving

$$N_{X,Z} = \frac{N_{X,Z-1} q_{X,Z-1} + N_{X,Z+1} \alpha_{X,Z+1}}{q_{X,Z} - \alpha_{X,Z}}. \quad (2.28)$$

To close the set of equations given by expression (2.28) for each stage of ionization of the element, we sum over all ion densities from the same element

$$N_X = \sum_{Z=1}^{Z+1} N_{X,Z}. \quad (2.29)$$

Numerical ionization balance calculations have been done by Arnaud and Rothenflug [3] for various elements that are abundant in the solar corona. They discuss in more detail the calculation of the ionization fraction. Arnaud and Raymond [2] have recently revised these calculations for iron.

## 2.4 The Line of Sight Intensity

The SERTS instrument, which is described in more detail in Section 3.1, can be used to observe the corona off the solar limb, as shown in Figure 2.2. The emission lines observed are optically thin, so most of the light emitted toward the observer will reach the observer. Since the instrument looks along a line of sight and not at a particular volume, the total intensity observed is an integral of all the properly directed emissions along the line of sight. Since the emissions are dependent on the density squared, and since the density is falling off rapidly with height, the region closest to the Sun along a given line of sight will normally dominate.

As just described, the observed spectral line intensity is the emission per unit volume integrated along the line of sight,

$$I_{X,Z,i,j} = \frac{1}{4\pi} \int_{-\infty}^{\infty} \epsilon_{X,Z,i,j} \, dx \quad (ergs \; cm^{-2} s^{-1} sr^{-1}), \quad (2.30)$$

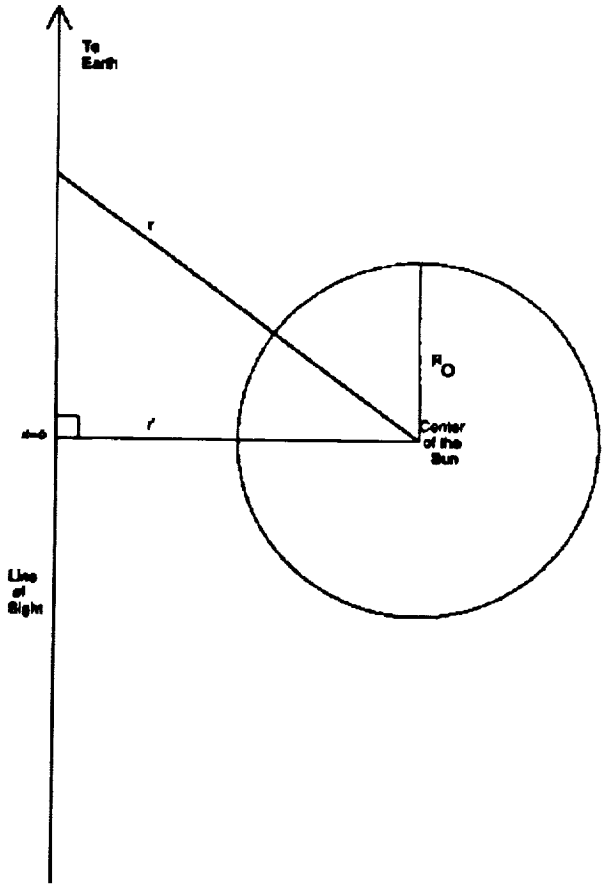


Figure 2.2. Illustrates the Line of Sight to the Sun and other geometrical quantities.

where $x$ is the path length along the line of sight and $x = 0$ is the point along the line of sight closest to the sun (Figure 2.2). In the coronal approximation, with the expression for intensity from Equation 2.17, this becomes

$$I_{X,Z,i,j} = \frac{1}{4\pi}\int_{-\infty}^{\infty} N_e^2 Q_{X,Z,i,j}(T_e, N_e)\frac{N_X}{N_e}dx \quad (ergs\ cm^{-2}s^{-1}sr^{-1}). \quad (2.31)$$

As a first approximation to the elemental abundance variations between different coronal regions, we can assume that the elemental abundance along the line of sight is constant, then we have

$$I_{X,Z,i,j} = \frac{\overline{Q_{X,Z,i,j}(T_e, N_e)}}{4\pi}\frac{N_X}{N_e}\int_{-\infty}^{\infty} N_e^2 dx \quad (ergs\ cm^{-2}s^{-1}sr^{-1}). \quad (2.32)$$

The density-weighted average contribution function is by definition

$$\overline{Q_{X,Z,i,j}(T_e N_e)} = \frac{\int_{-\infty}^{\infty} Q_{X,Z,i,j} N_e^2 dx}{\int_{-\infty}^{\infty} N_e^2 dx}, \quad (2.33)$$

we use the approximation

$$\overline{Q_{X,Z,i,j}(T_e N_e)} \approx Q_{X,Z,i,j}(\overline{T_e}, \overline{N_e}). \quad (2.34)$$

Since the emission from electron collision goes as $N_e^2$, the line-of-sight temperature is weighted by the $N_e^2$ and is

$$\overline{T_e} = \frac{\int_{-\infty}^{\infty} T_e N_e^2 dx}{\int_{-\infty}^{\infty} N_e^2 dx}, \quad (2.35)$$

and the line-of-sight density or line-ratio density which will be discussed in Section 2.5.1, is

$$\overline{N_e} = \frac{\int_{-\infty}^{\infty} N_e N_e^2 dx}{\int_{-\infty}^{\infty} N_e^2 dx}. \quad (2.36)$$

The line-of-sight electron density can be determined by numerical integration if we assume an exponential atmosphere of the form given by equation (2.10). If the scale height is less than

$0.2R_\odot$ the line-of-sight electron density can be related to the density as a function of radius as

$$\overline{N_e}(r') \approx 0.7 N_e(r), \qquad (2.37)$$

where $r'$ is the line-of-sight radius, or the minimum distance from the Sun's center to any point along the line of sight. Coronal scale heights were less than $0.2R_\odot$ for all three observed regions.

The equation for the intensity along the line-of-sight used in this dissertation is obtained by substituting Equation (2.34) into Equation (2.32). Doing this yields

$$I_{X,Z,i,j} = \frac{Q_{X,Z,i,j}(\overline{T_e}, \overline{N_e})}{4\pi} \frac{N_X}{N_e} \eta \quad (erg\ cm^{-2} sec^{-1}), \qquad (2.38)$$

where the column emission measure $\eta$ is defined as

$$\eta = \int_{-\infty}^{\infty} N_e^2 dx. \qquad (2.39)$$

The column emission measure is a quantity that can be determined from intensity observations whenever reasonable estimates of the contribution function can be obtained. The advantage of using a column emission measure is that the intensities of different lines are simply related by the ratios of their contribution functions. Thus, within the proper range of temperature and density, we can calculate the expected line intensities of other lines. The density can be inferred from the column emission measure by modeling, but cannot be directly determined from the line-of-sight intensity of one line. See Section 2.5.1 for the method to determine the density from more than one line. The column emission measure, $\eta$, can be rewritten, assuming spherical symmetry, as

$$\eta(r') = 2 \int_{r'}^{\infty} N_e^2(r) \frac{r}{\sqrt{r^2 - r'^2}} dr. \qquad (2.40)$$

This then becomes

$$\eta(r') = \overline{N_e^2}(r') L(r') f(r'), \qquad (2.41)$$

where $f(r')$ is the filling factor (Section 5.1) and $L(r')$ is the effective line-of-sight length, and $\overline{N_e^2}(r')$ is the average of the electron density squared at radius $r'$, which is approximately twice the average line-of-sight electron density squared, $(\overline{N_e})^2$. The effective line-of-sight length, $L(r')$, can be determined by numerical integration to within 1% for scale heights between 0.01 and 0.4 $R_\odot$, as

$$L(r') = (1.7064 * H_s^{0.5} + 1.7134 * H_s^{1.5}) r'^{1.5}, \qquad (2.42)$$

if we assume an exponential atmosphere with all units in solar radius units.

Substituting Equation (2.41) into Equation (2.38) we get

$$I_{X,Z,i,j}(r') = \frac{Q_{X,Z,i,j}(\overline{T_e}, \overline{N_e})}{4\pi} \frac{N_X}{N_e} \overline{N_e^2}(r') L(r') f(r'). \qquad (2.43)$$

If $\overline{N_e^2}$ has the radial dependence of $N_e$ in Equation 2.10, the intensity will be

$$I_{X,Z,i,j}(r') = \frac{Q_{X,Z,i,j}(\overline{T_e}, \overline{N_e})}{4\pi} \frac{N_X}{N_e} \overline{N_e^2}(r_o) L(r') f(r')\, exp\left[\frac{-2R_\odot^2}{H_s(T_0)}\left(\frac{1}{r_0} - \frac{1}{r}\right)\right] \qquad (2.44)$$

The above derivation was done independently by the author. Guhathakurta et al. [25] derived a similar result including resonance scattering indicating Equation 2.44 can be written as

$$I_{X,Z,i,j}(r') = C \frac{Q_{X,Z,i,j}(\overline{T_e}, \overline{N_e})}{4\pi} \frac{N_X}{N_e} N_e^{\zeta}(r_o) L(r_o, \zeta) r'^{1.5} exp\left[\frac{-\zeta}{H_s}\left(\frac{1}{r_o} - \frac{1}{r'}\right)\right] \qquad (2.45)$$

to include the effects of resonance scattering, where $C$ is a correction factor and the value of $\zeta$ is between one and two because of the density squared dependence of electron collisional excitation and the density dependence of resonance scattering.

## 2.5 Spectroscopic Diagnostics

With the development in the last section of the theoretical dependence of a spectral line intensity, we can now determine the properties of the emitting coronal plasma. This can be done by comparing different spectral lines which are suspected to be emitted by the same coronal plasma, and by determining what range of coronal conditions could produce the lines in the intensity ratios observed. Since there will always be a range of plasma conditions along any line of sight, values determined from comparing different spectral line intensities would be an average of the conditions along the line of sight weighted by emission from each region. Most of the coronal lines we observed are produced by electron collisional excitation. The spectral line intensity from such a line is dependent on the local electron temperature and electron density and on the relative elemental abundance.

Two general methods of modeling exist. One is the differential emission measure method, which usually assumes the low density limit, but allows for emitting plasma to exist at different temperatures distributed as a slowly varying function. The differential emission measures can be determined by forcing the theoretical distribution of emission measures to reproduce the observed spectral line intensities. The result then provides an indication of how the plasma along a given line of sight is distributed as a function of temperature. The uncertainty is dependent on the number of spectral lines used and normally the differential emission measure is least constrained at the highest and lowest temperature ranges where few spectral lines exist.

The other way to determine coronal plasma properties, which is used in this dissertation, needs fewer emission lines. In this method, we selectively compare the ratio of observed spectral line intensities whose theoretical ratio should depend only on one free parameter, in order to determine that parameter. Next, using that result, and then comparing lines with relative intensities depending on two parameters, we can determine the unknown parameters. This process is continued until all the parameters that can be determined from the available data set have been determined. The general method for determining each parameter will be discussed in the following sections. The steps are the following:

| | |
|---|---|
| 1. Determine $N_e$ | Using spectral lines from same element and ionization stage |
| 2. Determine $T_e$ | Using spectral lines from same element but different ionization stage and knowing $N_e$ |
| 3. Determine $\eta$ ($\int N_e^2 dx$) | Using the spectral line intensity and knowing $N_e$ and $T_e$ and assuming some ion to hydrogen abundance |
| 4. Determine the Relative Elemental Abundance | Using spectral lines from different elements and knowing $N_e$ and $T_e$ |

### 2.5.1 Density-Sensitive Lines

The ratio of intensities from two lines of the same ion are used to obtain the density measurement. Normally the line ratios are only density sensitive over two to three orders of magnitude of electron density and are approximately constant outside of this range. Each ion has its own range of density sensitivity. As an example, in Figure 2.3 the density sensitivity of a ratio of two lines of Fe XIII is given [41]. These line ratios are normally temperature insensitive.

The condition for spectral line ratios to be density sensitive in dense plasma is for the collisions between electrons and excited ions to become

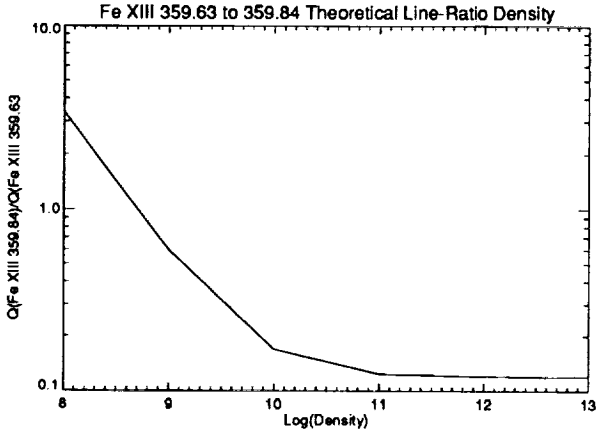


Figure 2.3. The theoretical ratio of intensities of Fe XIII 359.63 Å and 359.84 Å at Log($T_e$)=6.3. The ratio changes by an order of magnitude between electron densities of $10^8$ to $10^{10} cm^{-3}$ [41].

dominant. Then the first term in the denominator of Equation (2.24) is nonnegligible. If two lines from the same ion are used, the density, $\overline{N_e}$, can be determined from the observed line ratios, which eliminates the emission measure integral and relative elemental abundance in Equation (2.38), so we have

$$\frac{I_{X,Z,i,j}}{I_{X,Z,k,l}} = \frac{Q_{X,Z,i,j}(\overline{T_e}, \overline{N_e})}{Q_{X,Z,k,l}(\overline{T_e}, \overline{N_e})}, \tag{2.46}$$

where $k$ and $l$ are the levels of the second emission line. The temperature dependence in Equation (2.46) is normally small for lines from similar energy levels, since the temperature dependence is the factor $[exp(-(E_{i1} - E_{k1})/kT_e)]$. Reviews of calculations of line-ratio density sensitivity from different ions have been made by Keenan [29] and Doschek [14]. $N_e(r)$ can be determined from modeling of the solar corona.

### 2.5.2 Electron Temperature Determination

After establishing an appropriate density to use, either by the above method or by assuming some reasonable density, the electron temperature can be determined. In this dissertation limits on the electron density will be determined in Section 4.2 then the temperature will be determined. To obtain the electron temperature, one can take line ratios from

lines either from the same ion or from different ionization states of the same element to eliminate concern of variations in the relative elemental abundance. The disadvantages of using lines from the same ion are: 1) the weak temperature dependence of the collision rate, which requires a large energy difference between the originating levels to obtain a sensitive measure of temperature and 2) the fact that such diagnostic line pairs usually have a wide separation in wavelength and are then susceptible to experimental calibration uncertainties.

The method using lines from two different stages of ionization of the same element, which depends on the temperature dependence of the ionization fraction, is easier to use experimentally, since here one can choose diagnostic lines that are close in wavelength and still have strong temperature sensitivity. For this method to be accurate, however, the observed plasma does need to be in steady state and reliable calculation of the ionization balance must exist. In addition, both lines need to be emitted from the same volume of plasma, which will be shown to be the case in Section 4.2. The temperature-sensitive ratio is determined from Equation 2.38

$$\frac{I_{X,Z1,i,j}}{I_{X,Z2,k,l}} = \frac{Q_{X,Z1,i,j}(\overline{T_e}, \overline{N_e})}{Q_{X,Z2,k,l}(\overline{T_e}, \overline{N_e})}, \tag{2.47}$$

where the density dependencies of $Q_{X,Z1,i}$ and $Q_{X,Z2,k}$ are assumed to be small and the relative elemental abundance and emission measure divides out.

The uncertainties in the above equation come from two sources. First are the uncertainties in the measured intensities which are, for most cases in this dissertation, 15% for each spectral line relative to one another. The second source is the theoretical uncertainty in the determination of $Q$. This theoretical uncertainty can be divided

into two parts: the uncertainty in the emissivity and the uncertainty in the ionization balance. These are difficult to estimate; in this dissertation the following values will be used: 30% for the emissivity uncertainty, and $(Z2-Z1)^{0.5}\times 50\%$ for the ionization balance uncertainty and was determined from private communication with Arnaud [4], Raymond [47], and Monsignori-Fossi [41].

To find the total uncertainty from instrumental and theoretical sources, where both are assumed to be independent of each other and Gaussian, add the squares of the different uncertainties and take the square root. The upper and lower limits to the line-ratio temperature are then determined by multiplying or dividing the ratio of the intensities by the total uncertainty. In Section 6.2, the log of the ratio of the intensities is shown to be approximately linearly related to the log of the ratio of the contribution function over a range of temperatures. The uncertainty in the line-ratio temperature can often be written in the form $log(T) = 6.30 \pm 0.05$ where the $\pm 0.05$ is the uncertainty in the $log(T)$.

Since the line-ratio temperature versus radius curves are noisy, a least-squares fit to the line-ratio temperature was used, where the radial dependence of the temperature is assumed to take the form:

$$T(r) = T_o + a(r-1). \qquad (2.48)$$

The fitted line-ratio temperature is used instead of the raw line-ratio temperature versus radius data to determine the "actual" scale height (Section 4.4.4), the emission measure (Section 4.5), and the radiative flux (Section 5.2). The uncertainties of the fit are the measurement uncertainties. These are then added to the instrumental and the theoretical uncertainties to determine the uncertainties in the line-ratio temperature. For the cases in this dissertation, the uncertainty in $T_o$ is dominated by the theoretical uncertainty, while the uncertainty in $a$ is dominated by the uncertainty in the fit. For each region analyzed in this dissertation, multiple line-ratio temperatures are determined. One of them is selected as the best fitted line-ratio temperature and used in the rest of the analysis.

### 2.5.3 Emission Measure

The emission measure, $\eta$, can be determined using Equation 2.38 which can be rewritten as

$$\eta = \frac{4\pi I_{X,Z,i,j}}{Q_{X,Z,i,j}(\overline{T_e},\overline{N_e})}\left(\frac{N_X}{N_e}\right)^{-1}. \qquad (2.49)$$

The line-ratio density and the line-ratio temperature need to be determined as described in Sections 2.5.1 and 2.5.2. The contribution function $Q$ is often only weakly dependent on $\overline{N_e}$, so only a rough estimate is needed. Also the relative elemental abundance, $\frac{N_X}{N_e}$, is assumed in Section 2.5.4 it will be determined. The best fit line-ratio temperature is used to determine the radial dependence of $Q$.

The uncertainty in the emission measure can be best represented as an error factor, where the actual emission measure is within some error factor of the derived emission measure. The error factor contains the uncertainties due to both the measured intensity and the contribution function. The uncertainty in the line intensity comes from two sources: the uncertainty in the relative intensity of the line when compared to other lines, and the uncertainty in the absolute calibration of the instrument, which is a factor of 2. The absolute calibration uncertainty will affect all emission measures from the same flight equally and should not be used in the relative uncertainties of emission measures determined from different spectral lines. For the following analysis the absolute calibration uncertainty will only be included when the absolute value of the emission measure is important.

The uncertainty in $Q$ is determined from the uncertainty in the line-ratio temperature. The total relative uncertainty in emission measure is the square root of sum of the squares of the uncertainties in $Q$ and in the measured intensities.

The theoretical uncertainty in $Q$ which comes from the uncertainties in the ionization balance

and emissivity has not been used. It could be as large as a factor of 2. It would not be independent for the different stages of ionization and would probably have a temperature-dependent effect. It will be mentioned in the Table 4.7.

### 2.5.4 Relative Elemental Abundance

So far we have considered only spectral lines from one element. After the appropriate electron density and temperature have been determined, the relative elemental abundance of different elements can be determined. This is simply done by asking what relative elemental abundance would be needed to produce the observed spectral line intensities with the emitting corona plasma at a particular temperature and density. This is done by using Equation (2.38) rewritten as

$$\frac{N_X}{N_e} = \frac{4\pi I_{X,Z,i,j}}{Q_{X,Z,i,j}(\overline{T_e}, \overline{N_e})\eta}. \qquad (2.50)$$

By taking ratios of two lines from different elements, we have

$$\frac{N_{X1}}{N_{X2}} = \frac{I_{X1,Z1,i,j}}{I_{X2,Z2,k,l}} \frac{Q_{X2,Z2,k,l}(\overline{T_e}, \overline{N_e})}{Q_{X1,Z1,i,j}(\overline{T_e}, \overline{N_e})}, \qquad (2.51)$$

with $\eta$ dropping out.

The sources of uncertainties in the elemental abundance are the same as for the emission measure (Section 2.5.3). However, some of them are not independent. The uncertainty in the absolute calibration of the instrument cancels out. The uncertainty due to the line-ratio temperature from the two emission measures is not independent and will be determined by taking the ratio of the emission measures at $T$, and $T \pm \sigma_T$. The theoretical uncertainty in $Q$ discussed in Section 2.5.3 would become $2^{1.5}$ and will be mentioned in the Table 4.8.

## 2.6 Line Emissivity Effect on Scale Height

The original density scale height determined in Section 2.1 assumed a contribution function that is constant with radius. If this is not the case, the observed scale heights can disagree. By taking into account the variation in the contribution function for different spectral lines as a function of height, we can determine the actual density scale height from the observed scale heights. After the effects of the contribution function are removed, the spectral lines should have the same scale height unless they are produced by different coronal structures.

To obtain the scale height from the line intensity, we first determine the observed density scale height using Equation (2.43), where the radial dependence is

$$I_{X,Z,i,j}(r') \propto Q_{X,Z,i,j}(\overline{T_e}, \overline{N_e}) r'^{1.5} exp[\frac{-2}{H_s}(\frac{1}{r_o} - \frac{1}{r'})]. \qquad (2.52)$$

Here the radial dependence of the line of sight and electron density is used. If a constant contribution function, $Q$, is assumed, the observed scale height, $H_{os}$ is

$$\frac{-2y}{H_{os}} = ln\left(\frac{I}{r'^{1.5}}\right) + const, \qquad (2.53)$$

where

$$y = \frac{1}{r_o} - \frac{1}{r'}, \qquad (2.54)$$

and the radius to the 1.5 power comes from integrating along the line of sight.

If the contribution function is dependent on radius, the observed density scale height will differ from the real density scale height. For example, if the contribution function decreases with radius, a lower scale height would be observed. This could occur with emission lines whose temperature of maximum abundance is cooler than the coronal temperature when the temperature

increases with radius. If the line ratio temperature is known as a function of radius, this effect can be removed. First, finding the slope of the contribution function, c, with respect to y, Equation (2.53) becomes

$$\frac{-2y}{H_{os}} = \frac{-2y}{H_s} + cy. \qquad (2.55)$$

For lines for which resonance scattering is important, the derivation is more complicated; the result is that the factor of two in equations (2.53) and (2.55) becomes a number between 1 and 2, depending on the ratio of resonance scattering rate and collisional excitational rate according to Guhathakurta et. al. [25].

# Chapter 3

# Instrument

Before describing the analysis, a description of the SERTS instrument and the method of recording the raw data on film will be given. First, the instrument is described. Second, a general description of how the data are obtained and then converted into absolute intensities are included.

## 3.1 The SERTS Instrument

The Solar Extreme-ultraviolet Rocket Telescope and Spectrograph (SERTS) instrument obtains both images and spectra of solar coronal regions. The SERTS instrument (see Figure 3.1) consists of a Wolter Type II telescope that focuses the light on an entrance aperture which has two wide rectangular apertures (lobes) connected by a narrow slit. The front face of the entrance aperture is polished so that a reflected image of the region surrounding what the instrument "sees" on the Sun is obtained for initial pointing determination, using a broad band filter (3835 $\pm$ 30 Å). A 1500 Å thick filter of aluminum-silicon behind the entrance slit was used to prevent the visible and near-ultraviolet light from entering the spectrograph.

The extreme-ultraviolet (EUV) light which enters the spectrograph then reflects off of a near-normal incidence toroidal grating with a groove ruling density of 3600 grooves per *mm*. The spectrally dispersed radiation is recorded on Eastman Kodak 101-07, EUV sensitive photographic film. This film is advanced, frame by frame, during the flight to produce multiple exposures. For each spectral line there appears an image of the region of the Sun viewed through the entrance aperture. The size and shape of this aperture are shown in Figure 3.2. The film records images in emission lines from 235 Å to 450 Å in first order, and from 170 to 225 Å in second order. In Figure 3.3 a grey scale picture of the SERTS 1991 spectrum from one of the pointing positions is shown. Figure 3.4 shows the spectrum averaged over a number of rows of pixels in the wide-lobe region of the picture.

A gold-coated grating was used in the 1989 flight. In the 1991 flight, a different grating with a multilayer coating was used, which increased the efficiency in the range of 290 Å to 350 Å compared to the gold coated grating used on the first flight. The SERTS instrument is further described in Neupert et al. (1992) [43]. The SERTS 1991 instrument modifications are described in greater detail by Thomas et al. 1991 [55].

The instrument was launched on a Terrier-boosted Black Brant rocket on May 5, 1989, a flight designated as SERTS 1989, and a modified version was flown on May 7, 1991, a flight designated as SERTS 1991. During both flights, two different pointing positions were used, where the second pointing position was shifted along the long axis of the slit relative to the first pointing position (see Figure 3.6 for the SERTS 1991 pointing positions and Figure 3.5 for SERTS 1989 pointing position). This allowed images of the region of the sun where spectra had previously been taken and vice versa during the same flight.

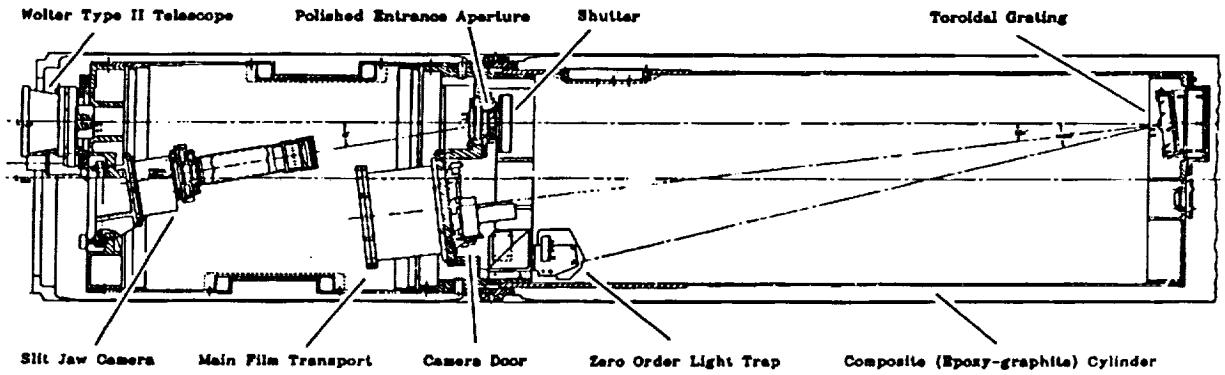


Figure 3.1. The light enters the SERTS instrument through a Wolter Type II telescope and is focused on the polished entrance aperture which selects a region of the Sun to observe. The light then is reflected off a toroidal grating and the first order image is recorded on film [43].

## 3.2 Data Reduction

The process of converting the exposed film to absolute solar intensity is a multiple step process. It is necessary to understand this process in order to understand sources of uncertainties in absolute intensities and the limits they place on the analysis.

The SERTS images were digitized by Thompson et al (1993) [56] with a Perkin-Elmer 1010M microdensitometer using a 10 by 10 $\mu m$ pixel area on the film, individual pixels were then averaged into 50 by 50 $\mu m$ pixel film-density units, corresponding roughly to 5 arc sec (3000 km by 3000 km), comparable to the typical 5-10 arc sec instrument resolution. During the analysis for this dissertation the 50 by 50 $\mu m$ pixels were further averaged to 150 by 150 $\mu m$ pixels. The film-density units were then converted into exposure units, using the film characteristic curve, which was determined experimentally also by Thompson et al. The uncertainty involved in these conversions is approximately 10%.

Next, the exposure units were converted to flux units by taking into account both instrumental efficiency and atmospheric extinction. The efficiency of the SERTS optics was measured at the Synchrotron Ultraviolet Radiation Facility (SURF-II) of the National Institute of Standards and Technology. The instrumental efficiency was then determined from the combination of the efficiencies of the different SERTS optics. The atmospheric extinction is model dependent, and was based on the Mass Spectrometer and Incoherent Scatter (MSIS) thermospheric model of Hedin (1987) [26].

Finally, a transformation from relative flux units to absolute solar irradiance was performed by normalizing the He II and Si XI 304 line intensity to previously observed, average quiet Sun values. The absolute calibration is estimated to have an uncertainty of no greater than a factor of two [54]. The following analysis will normally ignore this uncertainty, since it is the relative line strengths that are important in most cases. When this is not the case it will be noted.

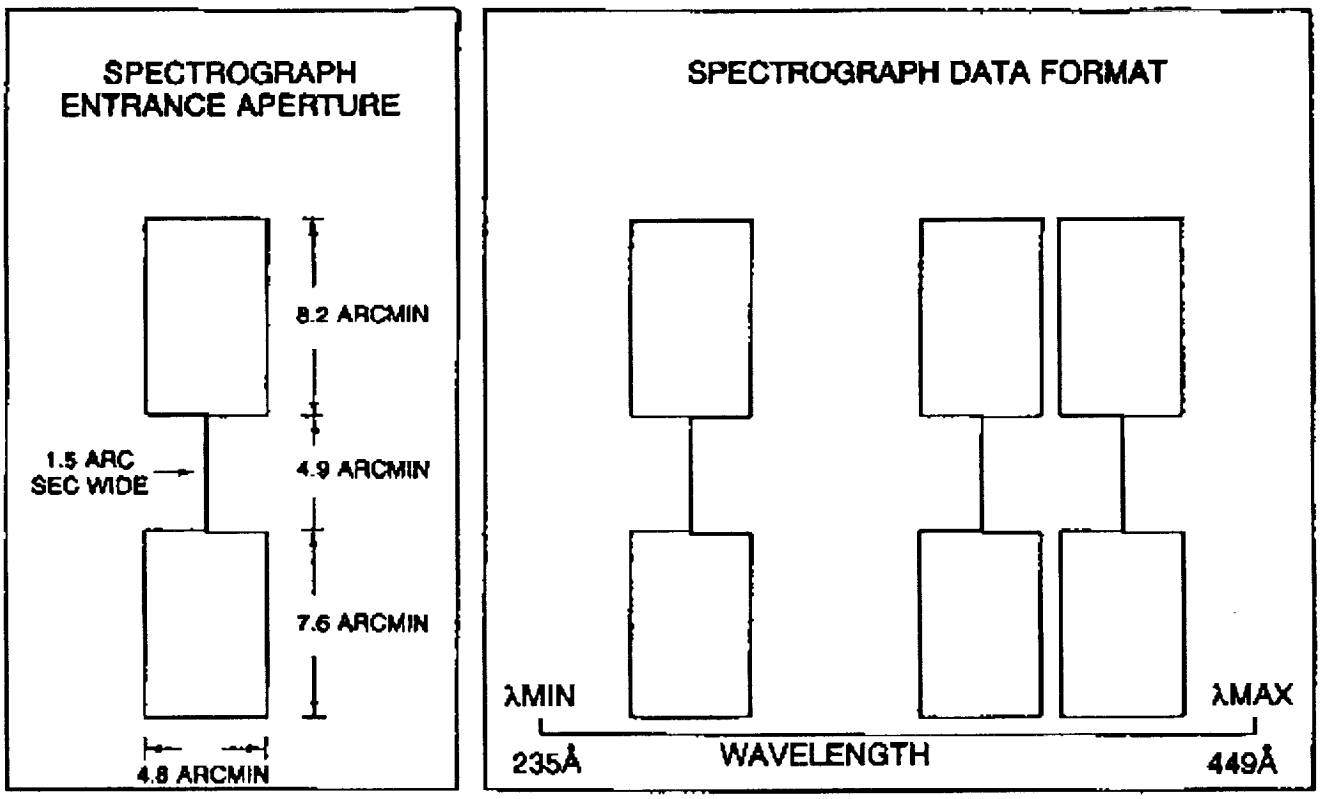


Figure 3.2. The schematic on the left shows the dimension of the SERTS entrance aperture. For each spectral line, there appears an image of the region of the Sun viewed through the aperture. The narrow slit provide a standard spectrum of high spectral resolution. The upper and lower wide lobes are wide compared to the spectral line width and allow imaging of two different regions of the Sun. The schematic on the right shows the relative position of images from three spectral lines and the instrument wavelength range in first order. The widths of the wide lobes are 6.8Å (not to scale in this schematic), and if two spectral lines lie closer than 6.8Å, then adjacent wide lobes will overlap. The analysis done in Chapter 4 uses the edges of the lower wide lobe, which for SERTS 1989 and 1991 yielded images of regions off the solar limb, as shown in Figures 3.5 and 3.6.

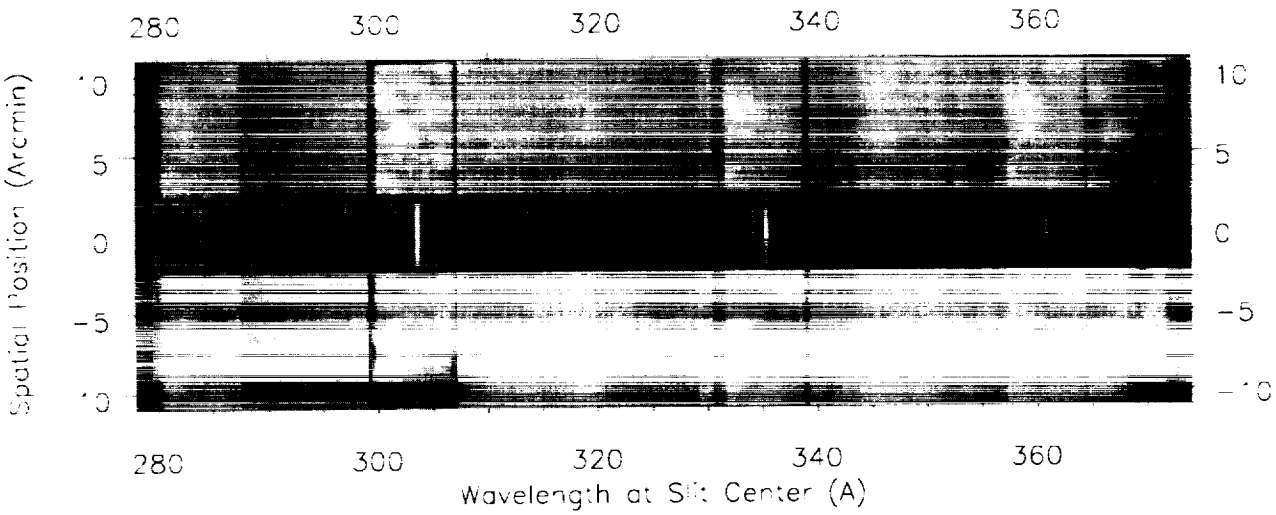


Figure 3.3. A portion of the SERTS 1991 spectrum with the intensity of many spectral lines reduced to show features in the wide-lobe images [13]. The central region of the picture contains the narrow slit spectrum with spectral resolution of 50mÅ. Additional spectral lines exist but are too faint to see for the brightness scale shown. The upper and lower wide lobes permit us to image regions of the Sun in many different spectra lines. Some overlapping of the wide lobes exists, but the brightest spectral lines produce easily observed edges. The data analyzed in this thesis were taken from the short wavelength edges off the solar limb. The solar limb starts at -8 arcmin on the short wavelength edge of the image and ends at -6 arcmin on the long wavelength edge of the image. The hot loop mentioned in Section 3.3.2 is apparent in the Fe XVI 335 Å image off the solar limb but is not seen in the He II 304 Å which is preferentially produced by cooler plasma.

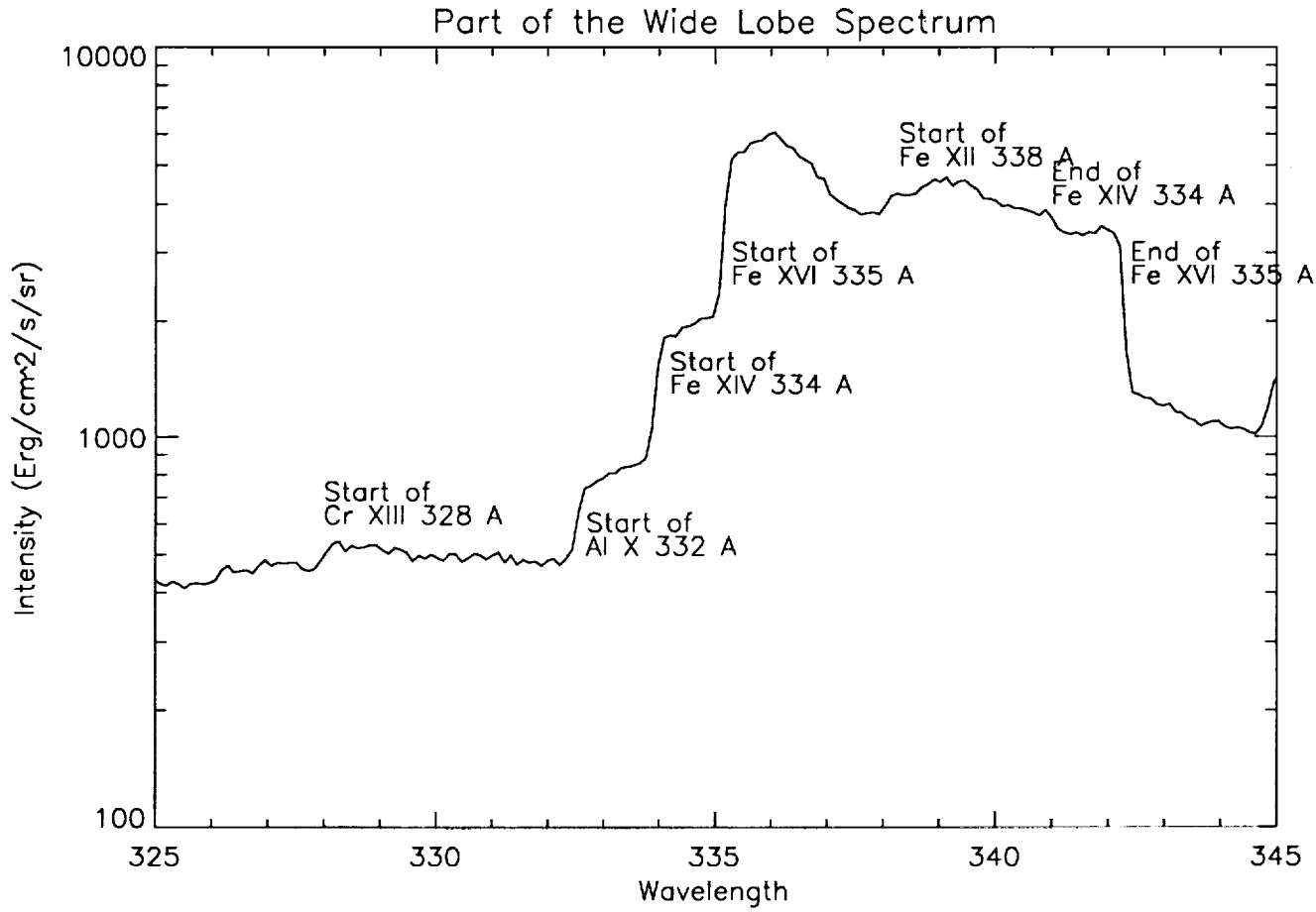


Figure 3.4. A portion of the SERTS 1991 wide-lobe spectrum is shown above with the edges of the lobes from different spectral lines marked. The wavelength scale in the abscissa is aligned with the short-wavelength edge of the lobe. The spectrum from the wide-lobe region of the picture is different from a standard spectrum. The intensity of any pixel is the background intensity and the summation of intensities from any spectral lines for which a portion of the wide lobe is imaged on that pixel. The spectrum for any row of pixels in the wide-lobe region shows a series of steps due to the wide-lobe edges of the different spectral lines followed by corresponding decreases in the intensity 6.8 Å away (equivalent to the physical width of the lobe). Any solar feature causes additional features to appear in the spectrum at the apparent wavelength corresponding to the appropriate physical location in the wide lobe. The intensity of selected spectral lines is determined from the increase in intensity across the edge of the image, as described in Section 4.1. In this thesis, only the line intensities at the lobe edges are used so variations across the lobe are unimportant.

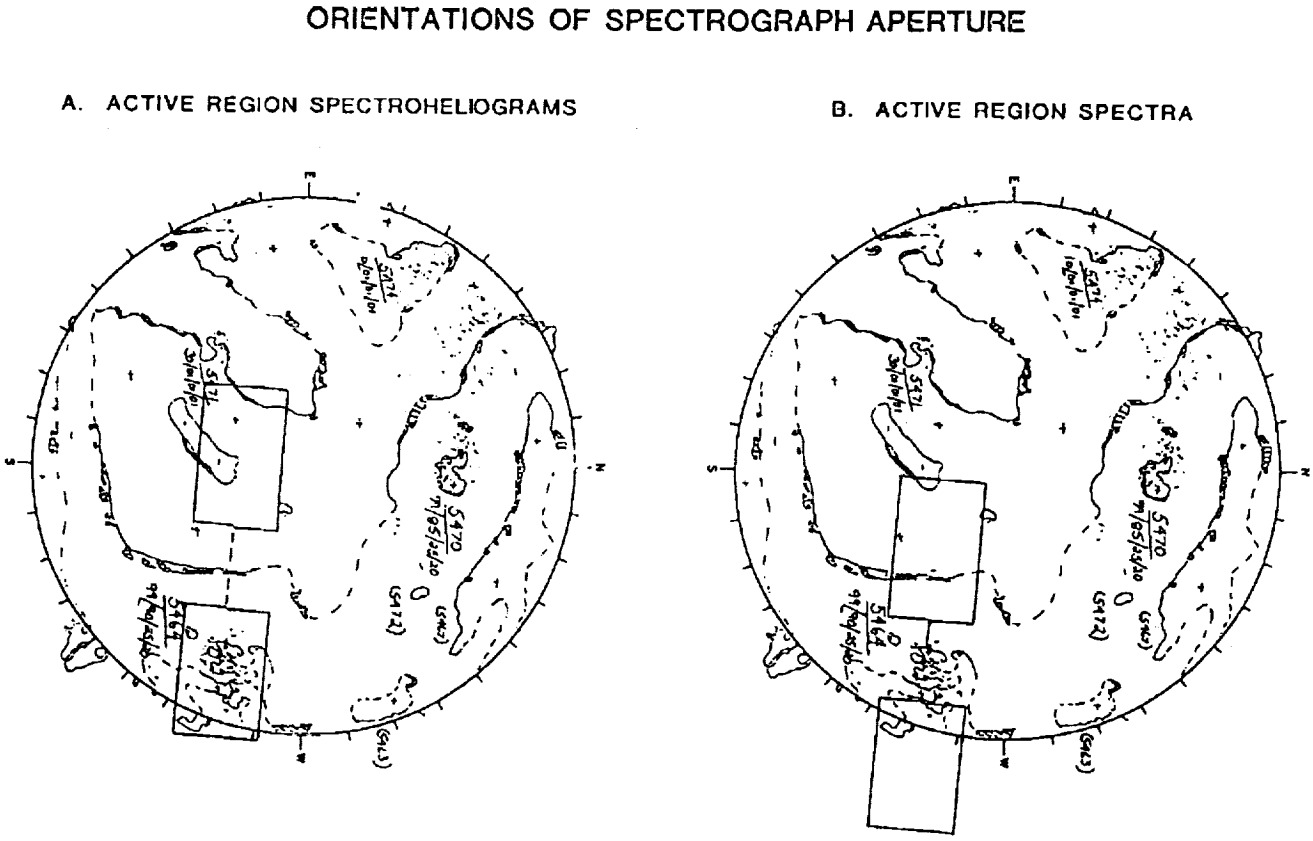


Figure 3.5. The two pointing positions from the SERTS 1989 flight [43]. The observations analyzed are for the active region spectra (3.5b). The solar drawing is of the magnetic neutral lines ($B_z = 0$). (Magnetic Neutral Line Drawing Courtesy of David Speich, NOAA)

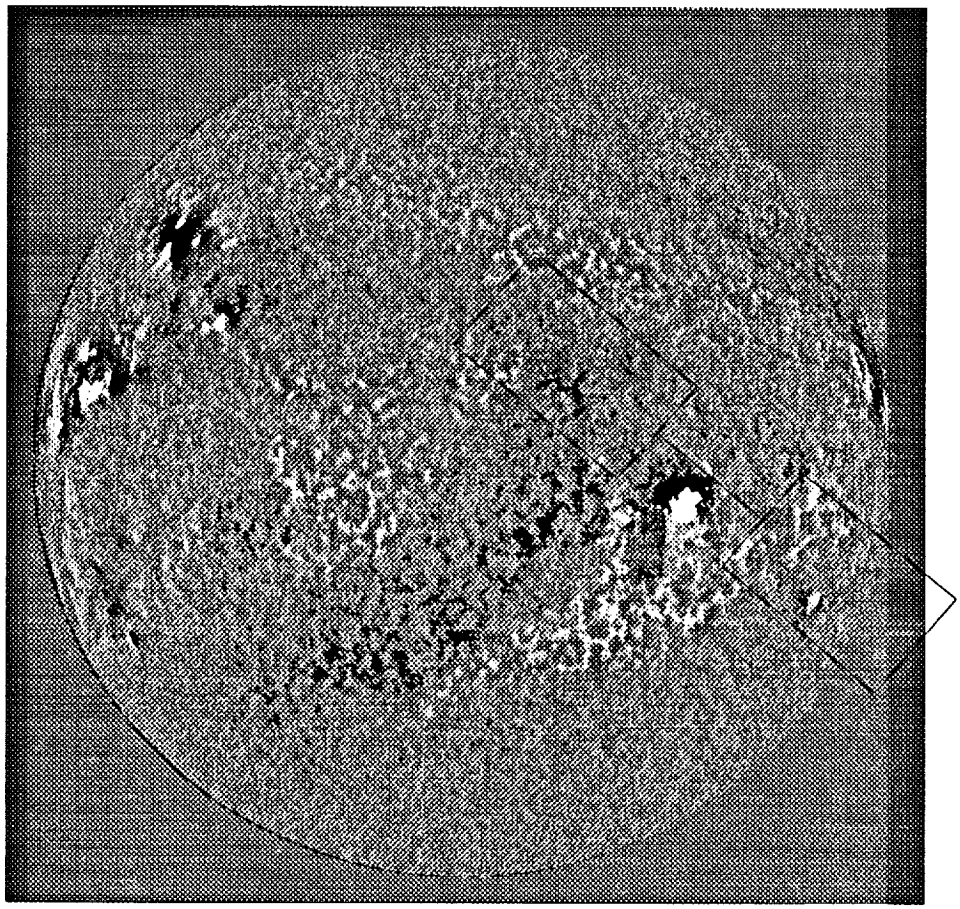

Figure 3.6. The SERTS 1991 pointing position superimposed on a solar magnetogram [8]. The second pointing position was shifted along the main axis of the lobes to extend further off the solar limb. The white and black regions on the magnetogram indicate the sign of the line-of-sight component of the photospheric magnetic field.

## 3.3 Observations

Next, we describe the conditions which existed off the solar limb during the two flights for the regions observed. The result comes from ground-based coronagraph observations [64, 65, 66], solar disk observations from a few days earlier [64, 65, 66], and the SERTS lobe images from different spectral lines.

### 3.3.1 SERTS 1989

The SERTS 1989 flight had only one of the two pointing positions partially off the limb Figure 3.5. Since only one exposure in this pointing position was made, this was the only exposure considered. Both edges of the off the Sun lobe were used for this study. The southernmost edge will be referred to as SERTS 1989 southern edge while the other edge is the SERTS 1989 northern edge, as shown in Figure 3.5 in some figures these were called the short-wavelength and long-wavelength edges. The solar sunspot activity is shown in Figure 3.7. The middle plot in Figure 3.7 shows the sunspot map for the day of the flight. The plot on the left shows the sunspot map from a quarter of a solar rotation earlier, to show the general nature of the solar activity which is behind the limb on the day of the flight. The sunspot maps show that there are two active regions (AR 5464 and AR 5460) which lie near the line of sight. The plot on the right shows the Fe XIV Sacramento Peak coronagram; no Fe X coronagram was made for the flight date. This indicates that the two observed regions analyzed here should be classified as quiet Sun.

### 3.3.2 SERTS 1991

The SERTS 1991 flight had two different pointing positions, each with 4 exposures of different duration. In the first pointing position, the lower (outer) lobe was completely off the solar limb with a part of the narrow slit off the disk. In the second pointing position, only a fraction of the outer lobe was off the disk. The longest exposure in both pointing positions was used in this analysis and where some lines were overexposed, the second longest exposures were used.

Only the southern edge of the lobe was used for this study for reasons which will be discussed later. This edge is called SERTS 1991 southern edge (see Figure 3.6). While no active regions exist at the solar limb, active regions exist in the foreground and others have rotated around the solar limb, as can be seen in the Boulder Sunspot Map from a quarter of a solar rotation earlier (see Figure 3.8). The Fe XIV coronagram shows larger emission than from the SERTS 1989 flight. A hot loop in Figure 3.3 is visible near the southern edge of the lobe in the images from hotter emission lines. A number of foreground and background active regions exist. The coronagrams taken for the day of the flight show both Fe X and Fe XIV emissions off the solar limb. These observations are classified as coming from a more active quiet sun region, since more emission from the active regions is seen along the line of sight.

April 28, 1989

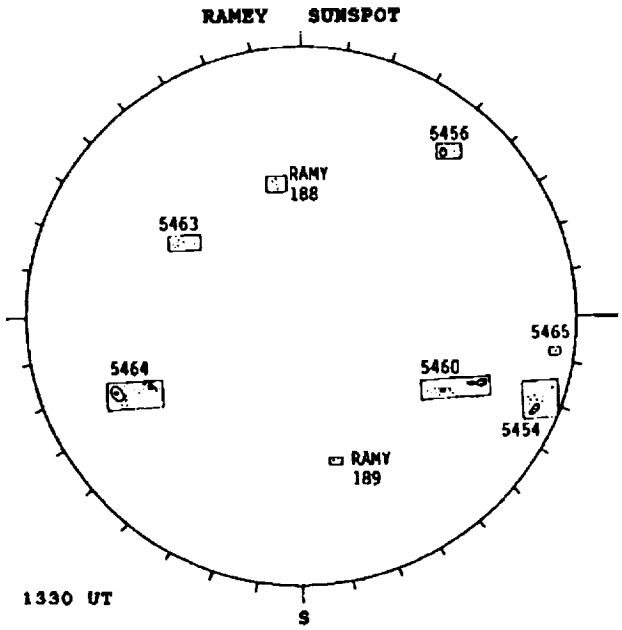


May 5, 1989

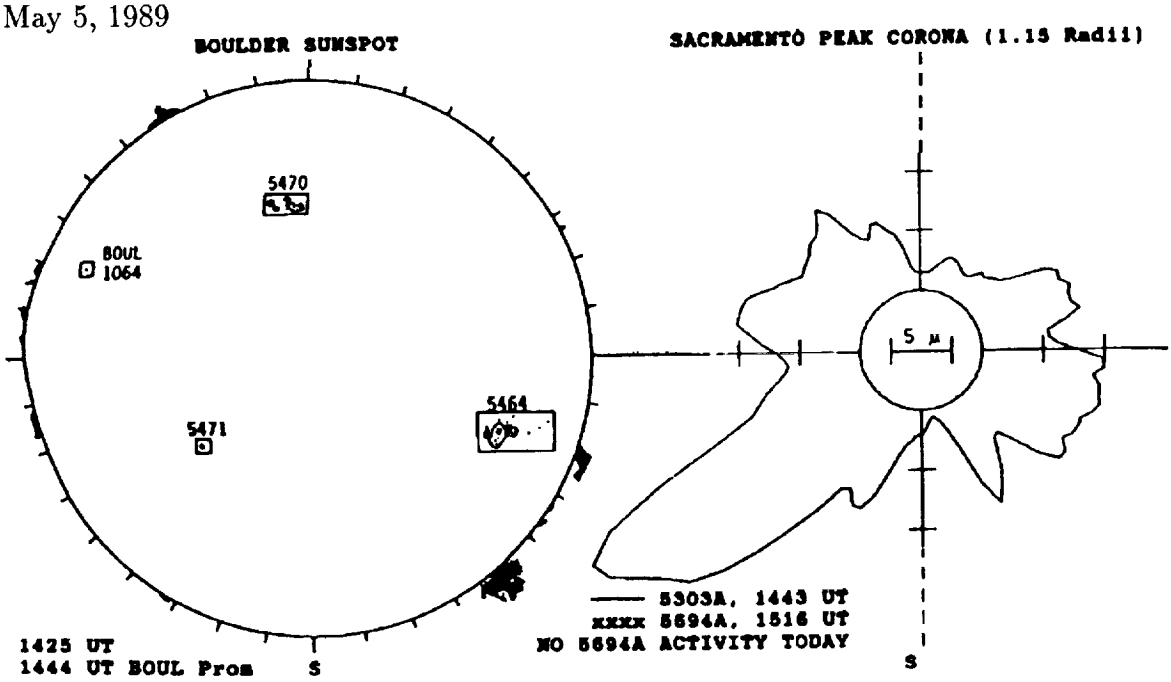


Figure 3.7. The schematic on the left shows the active regions on the Sun from a quarter of a solar rotation before the flight [64, 65]. The center one shows the location of the active regions on the day of the flight. The one on the right shows a coronagram from the day of the flight. The location of the edges of the lobe can be seen on Figure 3.5b.

April 30, 1991

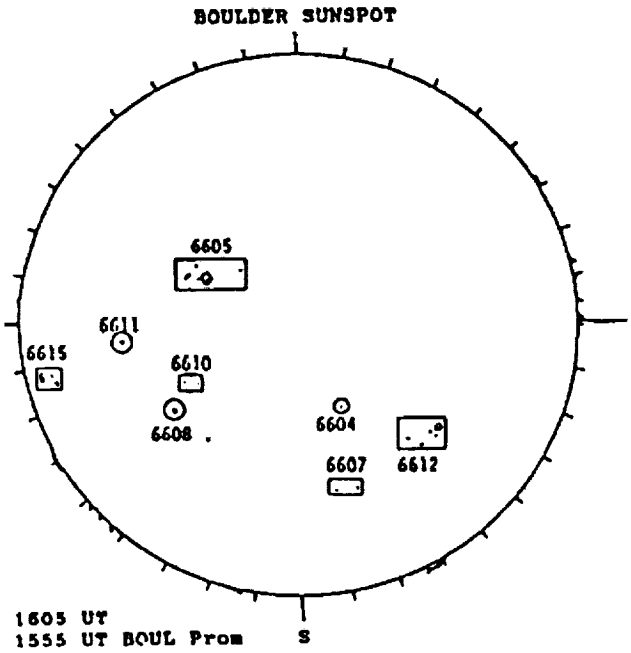


May 7, 1991

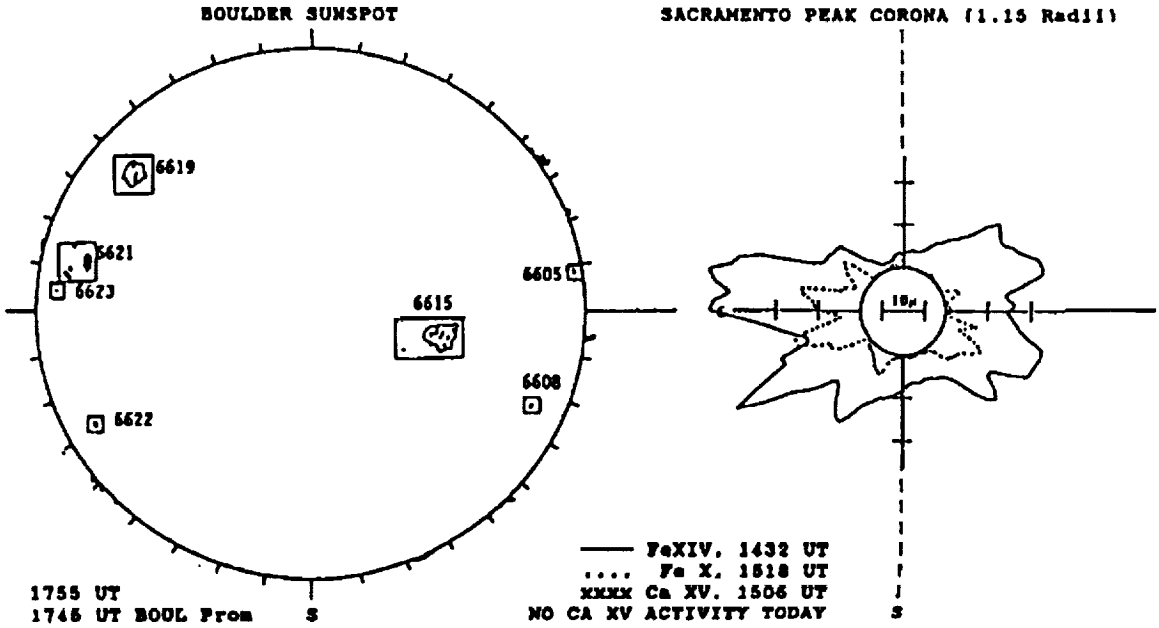


Figure 3.8. Description the same as Figure 3.7. The location of the edges of the lobe can be seen on Figure 3.6. The source is the Solar-Geophysical Data [66].

# Chapter 4

# Analysis

In this chapter, the analysis of the SERTS data is discussed using the theoretical tools developed in Chapter 2. First the criteria for line selection are explained. Next the density scale height of these lines is determined. Limits on the line-ratio densities are determined; then the line-ratio temperature is determined as a function of height. The line-ratio temperature is compared to the scale-height temperature after the effect of the radial dependence of the contribution function has been removed from the scale-height temperature as was discussed in Section 2.6. Finally, the emission measure and relative elemental abundance are determined.

## 4.1 Line Selection and Determination of Spectral Line Intensity

The edges of the lobes from different spectral lines (Section 3.3) were used to analyze the solar corona off the solar limb. By comparing the edges of the lobe to an adjacent section of the film, the spectral line intensity as a function of position was determined. The process of obtaining spectral line intensity as a function of radius will be shown. Then the data sets from both flights will be analyzed.

In order for the analysis of the SERTS off-the-limb data to be accurate, a line should meet the following conditions:

- The line should be strong compared to the background in order to minimize uncertainties in the line intensity.

- Adjacent lines must be resolved spectrally. When two ions emit at nearly the same wavelength, their emission lines are blended and only one spectral line is observed. Hence, this spectral line is a combination of the two emission lines which makes analysis of the combined radiation difficult because of the large uncertainties.

- The emission mechanism must be well understood. If the line emission mechanism is not well understood, or if the emission can be produced by multiple processes of similar strength (eg. electron collision, resonance scatter, and recombination), the analysis of the line will be uncertain. Such spectral lines were not included in this study.

- Any overlapping images should be weak since additional uncertainties in the spectral line intensity will occur where the lobe images overlap.

After the spectral lines were selected, the line intensities were determined by the following method. The location of the lobe edge for each spectral line was determined from the digitized images (Section 3.2). Since the 50 by 50 $\mu m$ pixels were smaller than the instrument spatial resolution, they were merged into 150 by 150 $\mu m$ pixels. The 150 by 150 $\mu m$ pixels were used

for the analysis in this dissertation. Thus, the intensity of the strip of 150 by 150 $\mu m$ pixels along the edge of the lobe is then the summation of the spectral line intensity and the background.

To determine the spectral line strength, the background is subtracted from each pixel . Since the instrument has some scatter which affects the pixels adjacent to the lobe as shown in Figure 4.1, the background strip was taken three 150 by 150 $\mu m$ pixels from the edge of the lobe. The spectral line intensity then is the intensity of the lobe's edge strip minus that of the background strip.

The solar coordinates for SERTS 1991 pixels were determined by Brosius et.al. [8]. Features observed in He II 304 Å by SERTS 1991 were compared to Kitt Peak observation of He I 10830 Å. The scale and orientation of the SERTS images compared to the Kitt Peak fixed coordinate system were then determined by a least squares fitting routine. The solar coordinates for SERTS 1989 pixels were determined by a similar method.

The relative uncertainty in the spectral line intensity is around 15% because of uncertainties in the intensity calibration, background subtraction, and the determination of where the edge of the lobe starts. Except for weak lines, the variation in the intensity of the spectral lines versus radius due to noise is normally less than the systematic uncertainties. So, the 15% uncertainty is the systematic uncertainty in the overall intensity of the spectral line and not for an individual spectral pixel on the line.

### 4.1.1 SERTS 1991

The southern edge of the off the limb portion of the lobes on the SERTS 1991 flight was found to have six spectral lines which satisfied the selection criteria. These lines were Al X 332 Å, Cr XIII 328 Å, Si XI 303 Å, Fe XIII 359 Å, Fe XIV 334 Å, and Fe XVI 361 Å. This data set is called SERTS 1991 southern edge. The northern edge had only one spectral line which met all requirements, the Fe XVI 335 Å line. Since the

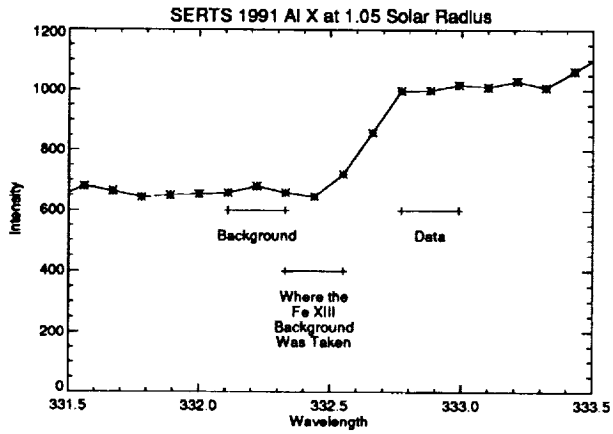


4.1a:

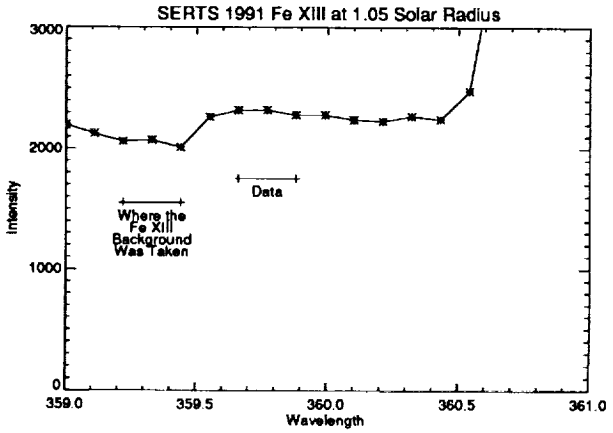


4.1b:

Figure 4.1. The spectrum shows a fraction of the lobe for the Al X 332 Å spectral line (4.1a). (The wavelength scale in the abscissa is aligned with the short-wavelength edge of the lobe.) Because of scatter in the instrument, the background needs to be taken from 4 to 6 pixels (50 by 50 $\mu m$ pixels) from the edge of the lobe. The Al X intensity is about 400 $erg/cm^2/s/sr$. For the Fe XIII 359 Å line (4.1b), the lobe from a nearby spectral line forces the background to be taken from between 2 to 4 pixels from the edge of the lobe. From analysis of different lines, we estimate that the background is raised by 5% of the spectral line intensity. The edge of the lobe from the Fe XVI 361 Å can be seen on the right at about 360.5 Å.

northern edge had so few lines, only the southern edge was analyzed.

The Fe XIII 359 Å had an additional complication of a nearby lobe overlapping the region where the background normally would be measured. Since the Fe XIII line was important for this analysis to obtain line-ratio temperature measurements, special treatment was given to this line. The background was determined using 150 by 150 $\mu m$ pixels which were only two pixels away from the lobe's edge instead of the normal three pixels. Since this background is not the true background, because it is also affected by scattered light from the Fe XIII line, the intensity of the Fe XIII is therefore underestimated. To determine the correction factor a study of other spectral lines was done by taking the background closer to the lobe's edge. As was done for Fe XIII, the correction factor was determined to be about 1.1 (Figures 4.1a and 4.1b). The Fe XIII line was then assigned an uncertainty of 25% instead of the normal 15% because of the extra uncertainty and other weak overlapping lobes.

In SERTS 1991, the overlapping portions of the lobe's edge from the two different pointing positions were merged. This technique allows analysis of the solar corona to greater heights than either one of the pointing positions alone. Since the spectral lines intensity did not align smoothly because of calibration uncertainties, a box car smoothing of five pixels (150 by 150 $\mu m$) was used.

### 4.1.2 SERTS 1989

The southern edge of the off-the-limb portion of the SERTS 1989 lobes was found to have five spectral lines which satisfied the selection criteria: Si XI 303 Å, Fe XIV 274 Å, Fe XIV 334 Å, Fe XV 284 Å, and Fe XVI 361 Å. The northern edge had four spectral lines, which were Fe XIV 274 Å, Fe XV 284 Å, Fe XV 417 Å, and Fe XVI 335 Å. The reasons for the changes in lines between the two flights were:

- The wider wavelength coverage in SERTS 1989,
- The increased efficiency and intensity of emission in SERTS 1991.

A list of the lines used, the ion that produces each line, and its wavelength, oscillator strength, transition array, and the sources of the two different sets of ionization balance calculations are given in Table 4.1.

### 4.1.3 Sets of Ionization Balance Calculations

Because the best ionization balance calculation for iron has not been determined, two different sets of calculations are used in this paper. The sources for the two ionization balance calculations for the different elements are given in Table 4.1. The only difference between these two sets is which ionization balance calculation for iron was used. For the first set of ionization balance calculations (IBAL1), the results for iron from Arnaud and Raymond [2] are used. For the second set of ionization balance calculations (IBAL2), the results for iron from Arnaud and Rothenflug [3] are used. The contribution functions for the spectral lines in Table 4.1 are given in Figure 4.2.

## 4.2 Scale Height

The spectral line intensities decreased exponentially with solar radius. The density scale height was determined for each line in all three data sets assuming electron collision excitation to be the line-formation mechanism for all lines (Section 2.4).

The scale-height temperatures determined from the density scale height using Equation 2.14 are shown in Figure 4.3 and given in Table 4.2. The first two numbers in the last row in each table are the average density scale height and the scale-height temperature for the observed lines.

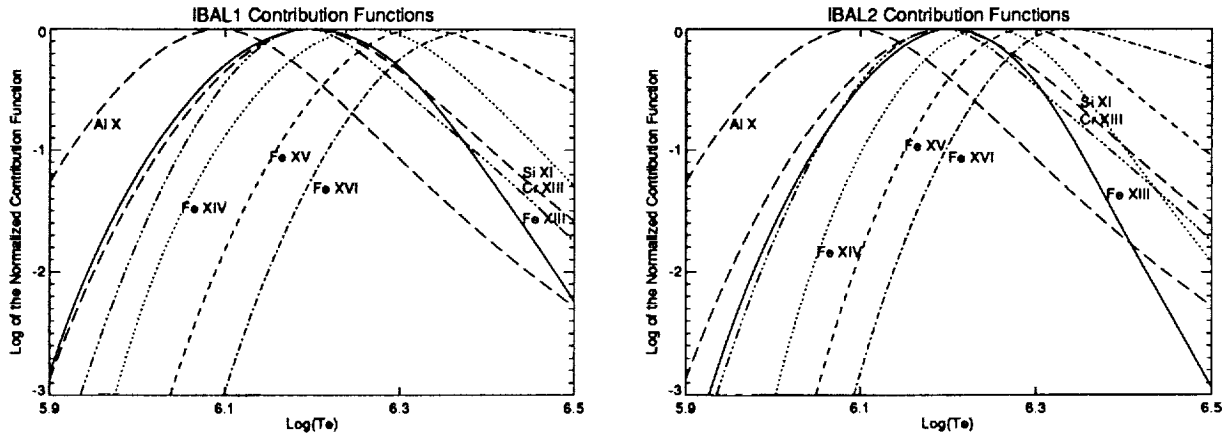


Figure 4.2. The normalized contribution functions are shown as functions of temperature for IBAL1 (4.2a), and IBAL2 (4.2b).

Table 4.1. Spectral Line Information

| Ion | $\lambda(\AA)$ | Oscillator Strength[a] | Transition Array[b] | IBAL1 | IBAL2 |
|---|---|---|---|---|---|
| Al X | 332.89 | 0.287[61] | $2s^2\ ^1S_0 - 2s2p\ ^1P_1^o$ | A+Ro | A+Ro |
| Cr XIII | 328.29 | 0.902[36] | $3s^2\ ^1S_0 - 3s3p\ ^1P_1^o$ | L+MF | L+MF |
| Si XI | 303.58 | 0.264[61] | $2s^2\ ^1S_0 - 2s2p\ ^1P_1^o$ | A+Ro | A+Ro |
| Fe XIII | 359.63 | 0.048[21] | $3s^23p^2\ ^3P_1 - 3s3p^3\ ^3D_2^o$ | A+Ra | A+Ro |
| Fe XIV | 274.203 | 0.200[21] | $3s^23p\ ^2P_{1/2}^o - 3s3p^2\ ^2S_{1/2}$ | A+Ra | A+Ro |
| Fe XIV | 334.171 | 0.077[21] | $3s^23p\ ^2P_{1/2}^o - 3s3p^2\ ^2D_{3/2}$ | A+Ra | A+Ro |
| Fe XV | 284.16 | 0.827[21] | $3s^2\ ^1S_0 - 3s3p\ ^1P_1^o$ | A+Ra | A+Ro |
| Fe XV | 417.258 | 0.032[21] | $3s^2\ ^1S_0 - 3s3p\ ^3P_1^o$ | A+Ra | A+Ro |
| Fe XVI | 335.407 | 0.270[21] | $3s\ ^2S_{1/2} - 3p\ ^2P_{3/2}^o$ | A+Ra | A+Ro |
| Fe XVI | 360.798 | 0.125[21] | $3s\ ^2S_{1/2} - 3p\ ^2P_{1/2}^o$ | A+Ra | A+Ro |

Notes:
a References for Oscillator Strength given in Brackets
b Transition Arrays from Kelly [30]
A+Ra. Arnaud and Raymond [2] ionization balance
A+Ro. Arnaud and Rothenflug [3] ionization balance
L+MF. Landini and Monsignori-Fossi [41] ionization balance

The Si XI density scale height temperature is the highest; this is probably caused by some contribution of resonance scattering to the total Si XI emission. The density scale heights from SERTS 1989 are larger than for SERTS 1991, with the largest density scale heights occurring for the SERTS 1989 northern edge.

The variation in density scale heights from different spectral lines can be explained by a combination of the change in the contribution function with radius because of a change in temperature and density of the emitting plasma, and, for some lines, resonance scattering (Section 2.6). Therefore, while the corona has an "actual" density scale height, the observed density scale height for each spectral line would vary depending on the radial dependence of the spectral line contribution function. In Section 4.4.4 the effect was modeled using the line-ratio temperature determined in Section 4.4. The result determined in Section 4.4.4 is given in the last two columns in Table 4.2 for IBAL1 and IBAL2. The values indicated by asterisk in the last row of each table are the "actual" density scale heights which were used in the model.

The density scale heights from the last two columns of Table 4.2 agree well with the observed density scale height for most spectral lines; therefore, the assumption that the observed spectral lines are emitted in the same coronal structures is reasonable.

## 4.3 Line-Ratio Electron Density

Limits on the line-ratio density will be determined in this section. The theory used in determining these limits was discussed in Section 2.5.1. The lower density limit on $N_e$ can be determined from comparing the ratio Fe XIII 359.63 Å and Fe XIII 359.84 Å intensities. The theoretical intensity ratio changes by a factor of 30 between electron densities of $10^8 cm^{-3}$ and $10^{10} cm^{-3}$. Since the Fe XIII 359.84 Å is either not observed or barely detected, the density needs to be greater than $10^9 cm^{-3}$ according to Figure 2.3. The absences of the detection of the Fe XIV 353 Å line while the Fe XIV 334 Å is observable indicate that the density needs to be less than $10^{10} cm^{-3}$. So for SERTS 1991 southern edge the electron density needs to be between $10^9$ and $10^{10} cm^{-3}$. These limits were determined below $1.1 R_\odot$. The density will decrease with height as shown in Section 2.1, so both of these limits will decrease with height.

An upper limit on the electron density for SERTS 1989 was determined by observing that the Fe XIV 264.82Å and the Fe XIV 274.203Å intensities were similar. This puts a strong upper limit of $10^{10} cm^{-3}$ on the density. The density is probably much less than this but, due to the large background noise near the 264.82Å line, it was not possible to determine a smaller upper limit.

## 4.4 Line-Ratio Temperature

Next, the line-ratio temperature was determined using the method described in Section 2.5.2 for spectral lines from different ionization stages of the same element. Densities consistent with the limits on the electron density determined in Section 4.3 were used in determining the line-ratio temperature. The line-ratio temperature was found to vary with height as will be discussed below.

### 4.4.1 SERTS 1991

The line-ratio temperature was derived for the SERTS 1991 southern edge data set. The results are shown in Figure 4.4a for an electron density of $10^{8.9} cm^{-3}$ and IBAL1 (see Section 4.4.3). Results using IBAL2 are shown in Figure 4.5a. A constant electron density was used, since the exact radial density dependence was not known. An electron density of $10^{8.9} cm^{-3}$ was chosen as

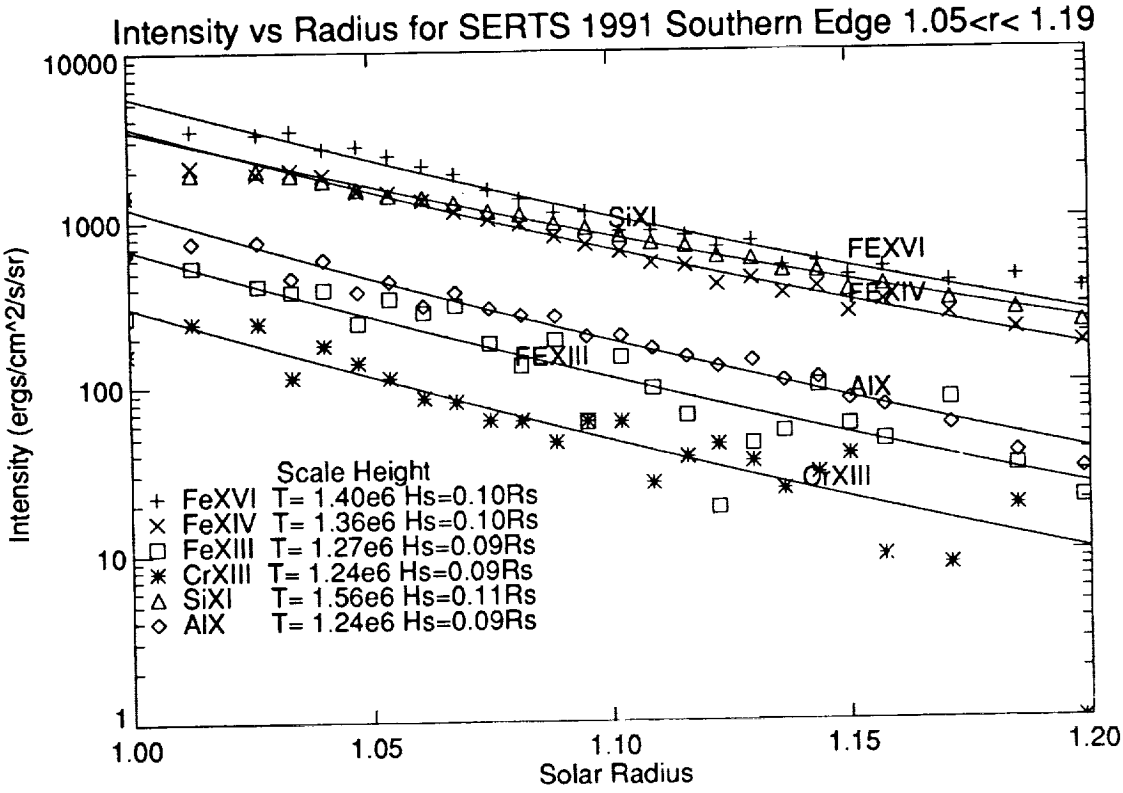


4.3a:

Figure 4.3. Plots of the log of the intensity vs. radius to determine the scale height for SERTS 1991 southern edge (4.3a), SERTS 1989 southern edge (4.3b) and SERTS 1989 northern edge (4.3c). The data from each ionization stage is marked by a different symbol. The fits used to determine the scale height are shown by the lines. The scale height and the scale-height temperature are given in a table on each figure. The systematic uncertainty in the intensity of the lines is 15% except for Fe XIII which is 25%.

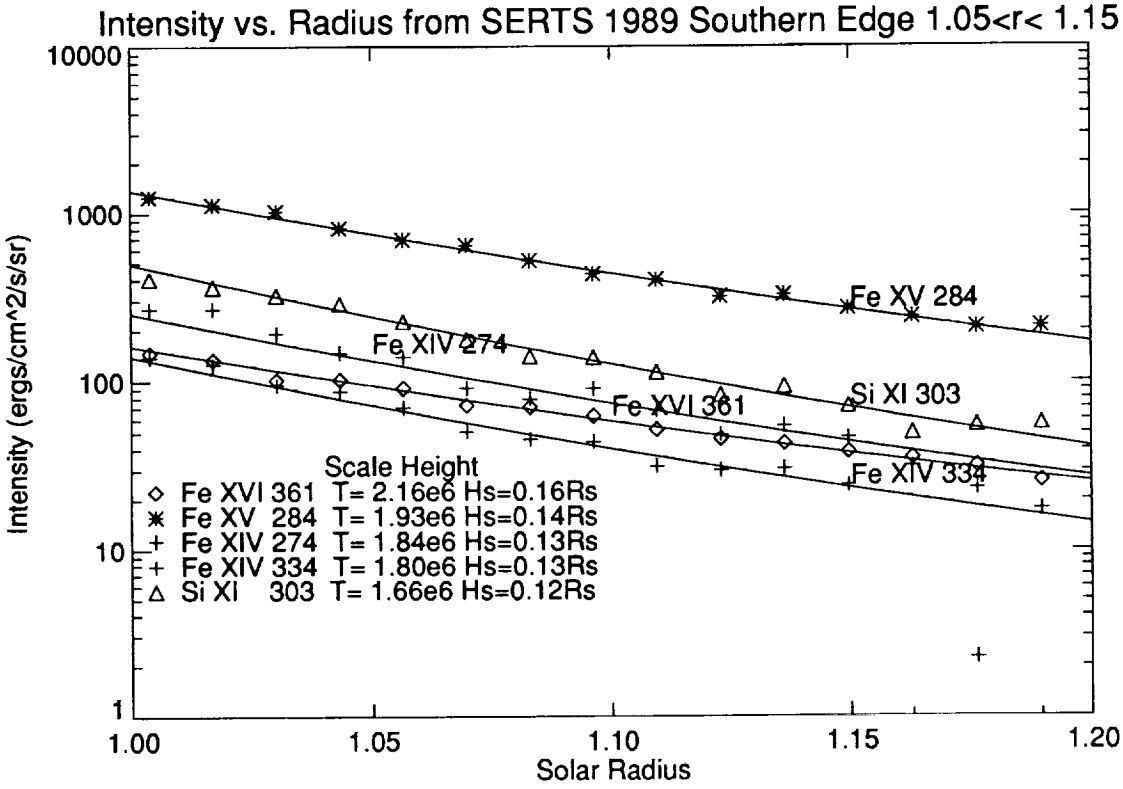
Intensity vs. Radius from SERTS 1989 Southern Edge 1.05<r< 1.15
Intensity (ergs/cm^2/s/sr)
Solar Radius
Fe XV 284
Fe XIV 274
Fe XVI 361
Si XI 303
Fe XIV 334
Scale Height
Fe XVI 361 T= 2.16e6 Hs=0.16Rs
Fe XV 284 T= 1.93e6 Hs=0.14Rs
Fe XIV 274 T= 1.84e6 Hs=0.13Rs
Fe XIV 334 T= 1.80e6 Hs=0.13Rs
Si XI 303 T= 1.66e6 Hs=0.12Rs

4.3b:

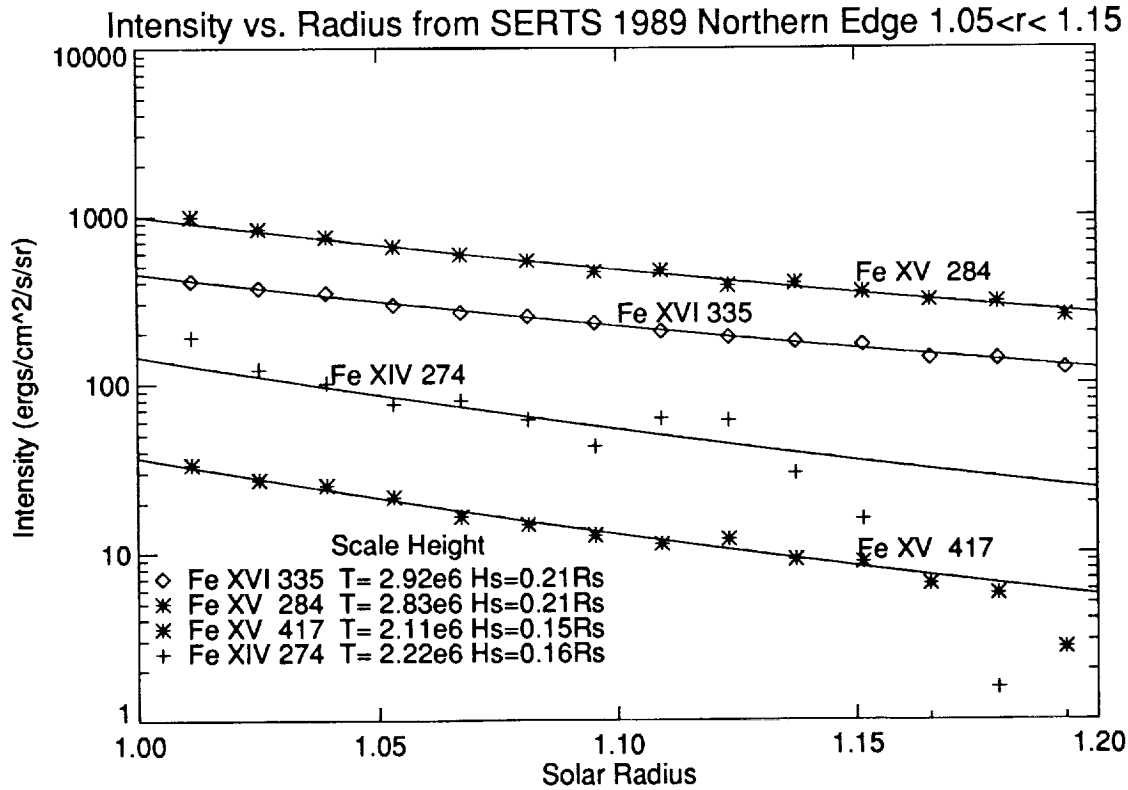
Intensity vs. Radius from SERTS 1989 Northern Edge 1.05<r< 1.15
Intensity (ergs/cm^2/s/sr)
Solar Radius
Fe XV 284
Fe XVI 335
Fe XIV 274
Fe XV 417
Scale Height
Fe XVI 335 T= 2.92e6 Hs=0.21Rs
Fe XV 284 T= 2.83e6 Hs=0.21Rs
Fe XV 417 T= 2.11e6 Hs=0.15Rs
Fe XIV 274 T= 2.22e6 Hs=0.16Rs

4.3c:

Table 4.2. Temperature from Scale Height

Table 4.2a: SERTS 1991 Southern Edge(1.05 to 1.19$R_\odot$)

| Ion $\lambda$(Å) | Log(T) Max Abundance | Density Scale Height | Scale-Height Temperature | Predicated Density Scale Height[e] IBAL1[d] | IBAL2[d] |
|---|---|---|---|---|---|
| Fe XVI 361 | 6.41(2.57e6)[a] | 0.10$R_\odot$ | 1.4e6 | 0.11 | 0.11 |
| Fe XIV 334 | 6.26(1.82e6)[a] | 0.10$R_\odot$ | 1.4e6 | 0.10 | 0.10 |
| FeXIII 359 | 6.20(1.58e6)[a] | 0.09$R_\odot$ | 1.3e6 | 0.09 | 0.09 |
| Si XI 303 | 6.20(1.58e6)[b] | 0.11$R_\odot$ | 1.6e6 | 0.09 | 0.09 |
| Cr XIII 328 | 6.19(1.55e6)[c] | 0.09$R_\odot$ | 1.2e6 | 0.09 | 0.09 |
| Al X 332 | 6.10(1.26e6)[b] | 0.09$R_\odot$ | 1.2e6 | 0.09 | 0.09 |
| | [Avg | 0.10±0.01$R_\odot$ | 1.3±0.1e6] | | |

NOTES:
a Calculated from ionization balance from Arnaud and Raymond [2].
b Calculated from ionization balance from Arnaud and Rothenflug [3].
c Calculated from ionization balance from Landini and Monsignori-Fossi [41].
d. IBAL1 and IBAL2 defined in Table 4.1.
e. A "actual" density scale height of 0.10$R_\odot$ was used to determine the predicted density scale heights discussed in Section 4.4.4.

Table 4.2b: SERTS 1989 Southern Edge(1.05 to 1.15$R_\odot$)

| Ion $\lambda$(Å) | Log(T) Max Abundance | Density Scale Height | Scale-Height Temperature | Predicated Density Scale Height[e] IBAL1[d] | IBAL2[d] |
|---|---|---|---|---|---|
| Fe XVI 361 | 6.41(2.57e6)[a] | 0.16$R_\odot$ | 2.2e6 | 0.16 | 0.15 |
| Fe XV 284 | 6.32(2.09e6)[a] | 0.14$R_\odot$ | 1.9e6 | 0.14 | 0.13 |
| Fe XIV 334 | 6.26(1.82e6)[a] | 0.13$R_\odot$ | 1.8e6 | 0.12 | 0.12 |
| Fe XIV 274 | 6.26(1.82e6)[a] | 0.13$R_\odot$ | 1.8e6 | 0.12 | 0.12 |
| Si XI 303 | 6.20(1.58e6)[b] | 0.12$R_\odot$ | 1.7e6 | 0.11 | 0.11 |
| | [Avg | 0.14±0.01$R_\odot$ | 1.9±0.2e6] | | |

NOTES:
a Calculated from ionization balance from Arnaud and Raymond [2].
b Calculated from ionization balance from Arnaud and Rothenflug [3].
c Calculated from ionization balance from Landini and Monsignori-Fossi [41].
d. IBAL1 and IBAL2 defined in Table 4.1.
e. A "actual" density scale height of 0.125$R_\odot$ was used to determine the predicted density scale heights discussed in Section 4.4.4.

Table 4.2c: SERTS 1989 Northern Edge(1.05 to 1.15$R_\odot$)

| Ion $\lambda$(Å) | Log(T) Max Abundance | Density Scale Height | Scale-Height Temperature | Predicated Density Scale Height[e] IBAL1[d] | IBAL2[d] |
|---|---|---|---|---|---|
| Fe XVI 335 | 6.41(2.57e6)[a] | 0.21$R_\odot$ | 2.9e6 | 0.20 | 0.20 |
| Fe XV 284 | 6.32(2.09e6)[a] | 0.21$R_\odot$ | 2.8e6 | 0.16 | 0.16 |
| Fe XV 417 | 6.32(2.09e6)[a] | 0.15$R_\odot$ | 2.1e6 | 0.16 | 0.16 |
| Fe XIV 274 | 6.26(1.82e6)[a] | 0.16$R_\odot$ | 2.2e6 | 0.13 | 0.13 |
| | [Avg | 0.18±0.03$R_\odot$ | 2.5±0.4e6] | | |

NOTES:
a Calculated from ionization balance from Arnaud and Raymond [2].
b Calculated from ionization balance from Arnaud and Rothenflug [3].
c Calculated from ionization balance from Landini and Monsignori-Fossi [41].
d. IBAL1 and IBAL2 defined in Table 4.1.
e. A "actual" density scale heights of 0.16$R_\odot$ for IBAL1 and 0.18$R_\odot$ for IBAL2 were used to determine the predicted density scale heights discussed in Section 4.4.4.

reasonable since it produces self-consistent plots for radial positions greater than 1.1 $R_\odot$.

The systematic temperature uncertainties due to instrumental and theoretical uncertainties (Section 2.5.2) are shown in Figures 4.4a and 4.5a as vertical error bars in the upper left-hand corner; they affect the overall normalization of the derived line-ratio temperature curves and do not denote relative uncertainties of each data point.

The fit was done for the line-ratio temperature for Fe XIII/Fe XVI above 1.1 $R_\odot$, because excess emission from the hot loop (Section 3.3.2) contributes to the Fe XVI emission below this height. The fits to Equation 2.48 for both the FeXIII/Fe XIV and Fe XIV/Fe XVI line-ratio temperatures are given in Table 4.3. The Fe XIV/Fe XVI temperature is considered to be more accurate because of additional noise due to background subtraction in the Fe XIII/Fe XIV line-ratio temperature above 1.1$R_\odot$. The fit for this ratio is plotted in Figures 4.4a and 4.5a. This fitted curve is used instead of the raw temperature versus radius data to determine the "actual" scale height (Section 4.4.4), the emission measure (Section 4.5), and radiative flux (Section 5.2).

### 4.4.2 SERTS 1989

Line-ratio temperatures were determined for SERTS 1989 southern and northern edges in the same way as for SERTS 1991 southern edge and the results are plotted in Figures 4.4b, 4.4c, 4.5b, and 4.5c. The line-ratio temperatures increase with radius.

SERTS 1989 data sets have a larger spread in line-ratio temperatures than SERTS 1991. This spread is within the uncertainties in the line-ratio temperature. The apparent spread in the line-ratio temperatures may be real (Section 4.4.3). The least-square fits to the line-ratio temperature are given in Table 4.4 for the SERTS 1989 southern edge, and in Table 4.5 for the SERTS 1989 northern edge.

For SERTS 1989 northern edge, the difference in the slope of the line-ratio temperature, $a$, for ratios involving Fe XV (Table 4.5) indicates that Fe XV 284 Å is affected by resonance scattering. This leads to more Fe XV 284 Å emission than would be predicted by electron collision excitation. Thus, the line-ratio temperature determined from the Fe XV 284 Å /Fe XVI 335 Å

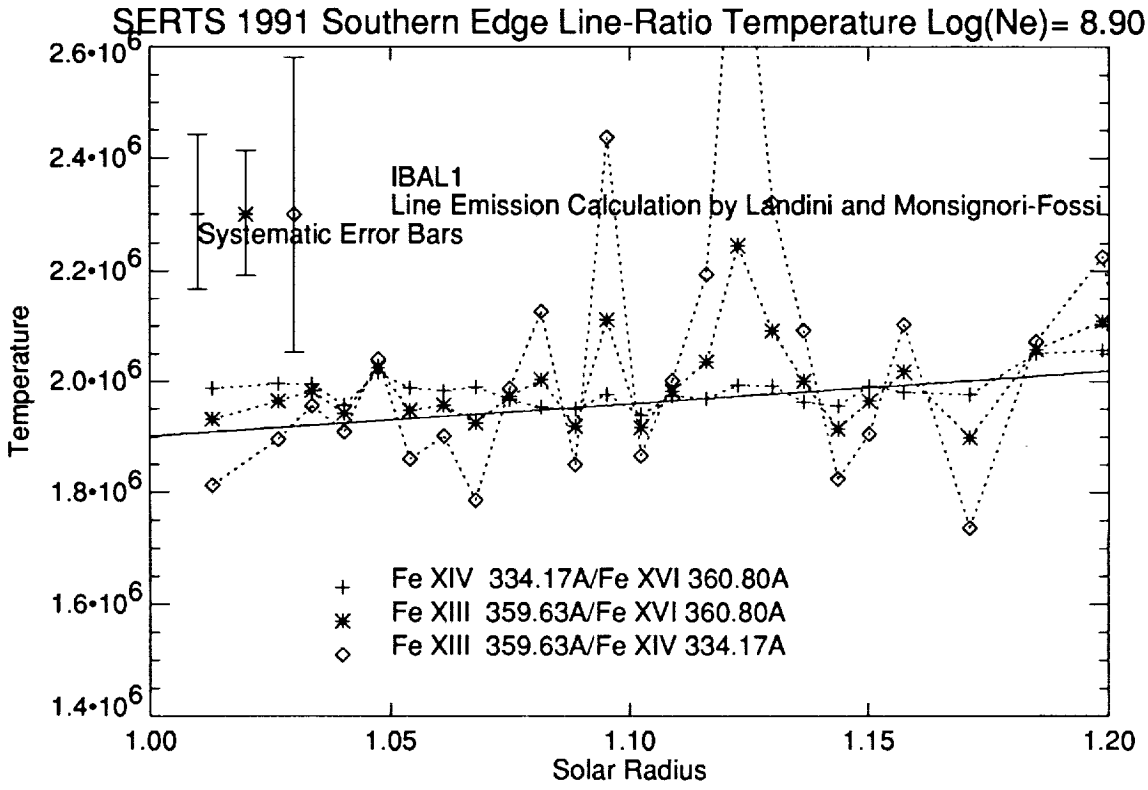


4.4a:

Figure 4.4. Plots of the line-ratio temperature vs. radius for SERTS 1991 southern edge (4.4a), SERTS 1989 southern edge (4.4b) and SERTS 1989 northern edge (4.4c) using IBAL1 and line emission calculations by Landini and Monsignori-Fossi [41]. Systematic error bars are shown for each line-ratio temperature in the upper left-hand corner of the figure, with the symbol on each error bar indicating the respective line ratio. The major source of the uncertainty is from the intensity calibration and would shift the whole line-ratio temperature curve up or down. The line-ratio temperature for Fe XIII 359 Å has two peaks near $1.1R_{\odot}$. These probably are not real, but are due to uncertainties in background subtraction.

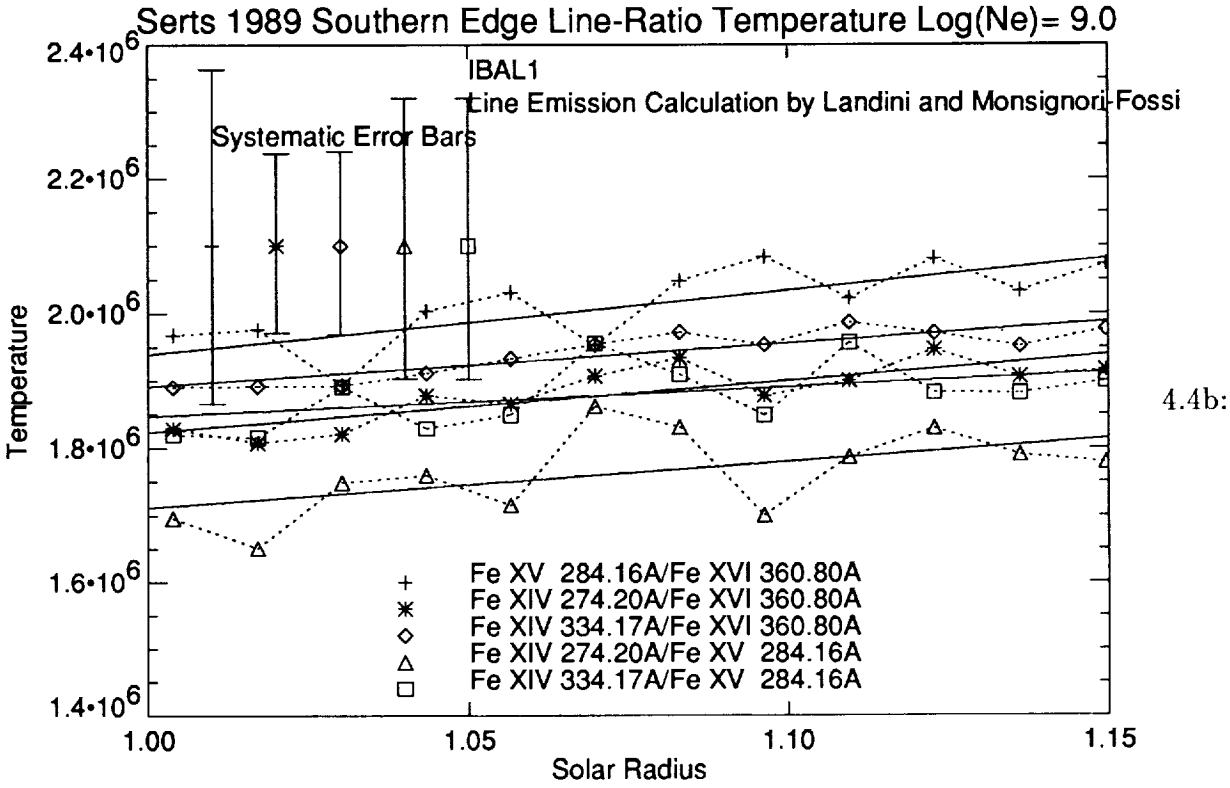


4.4b:

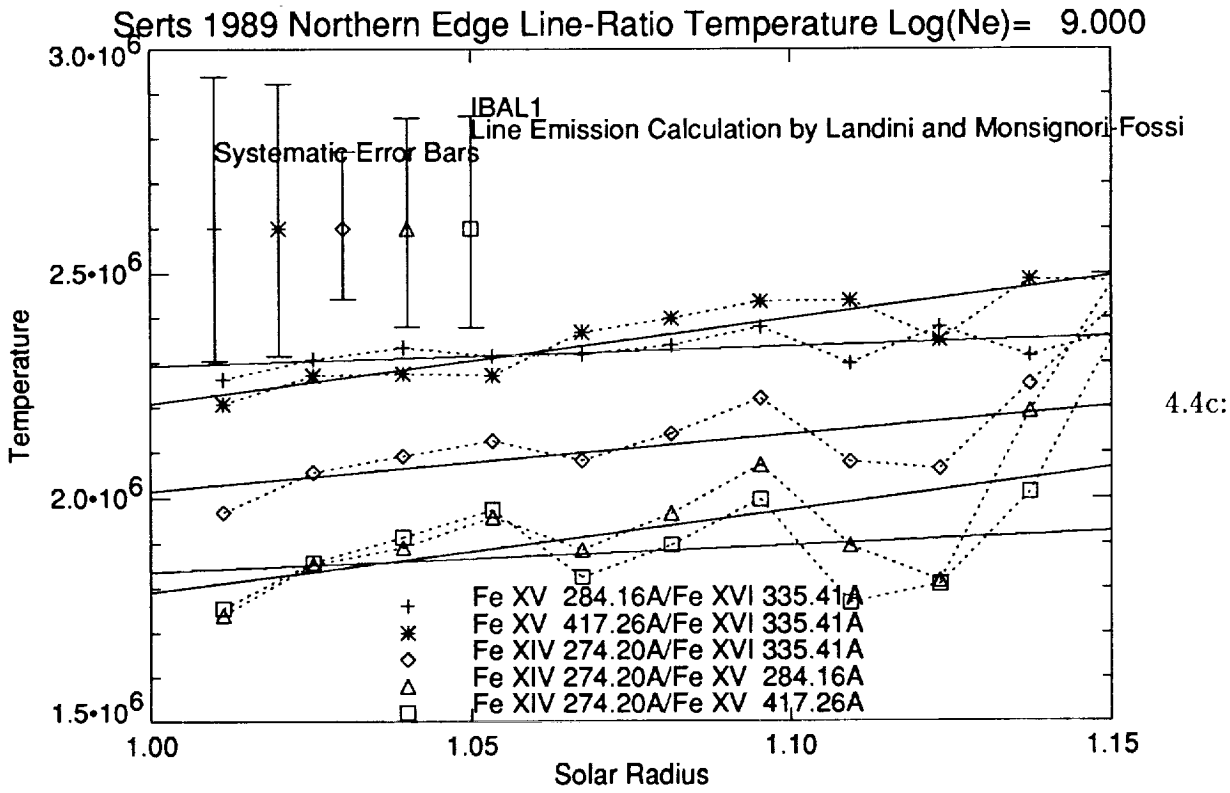


4.4c:

Figure 4.4 cont'd

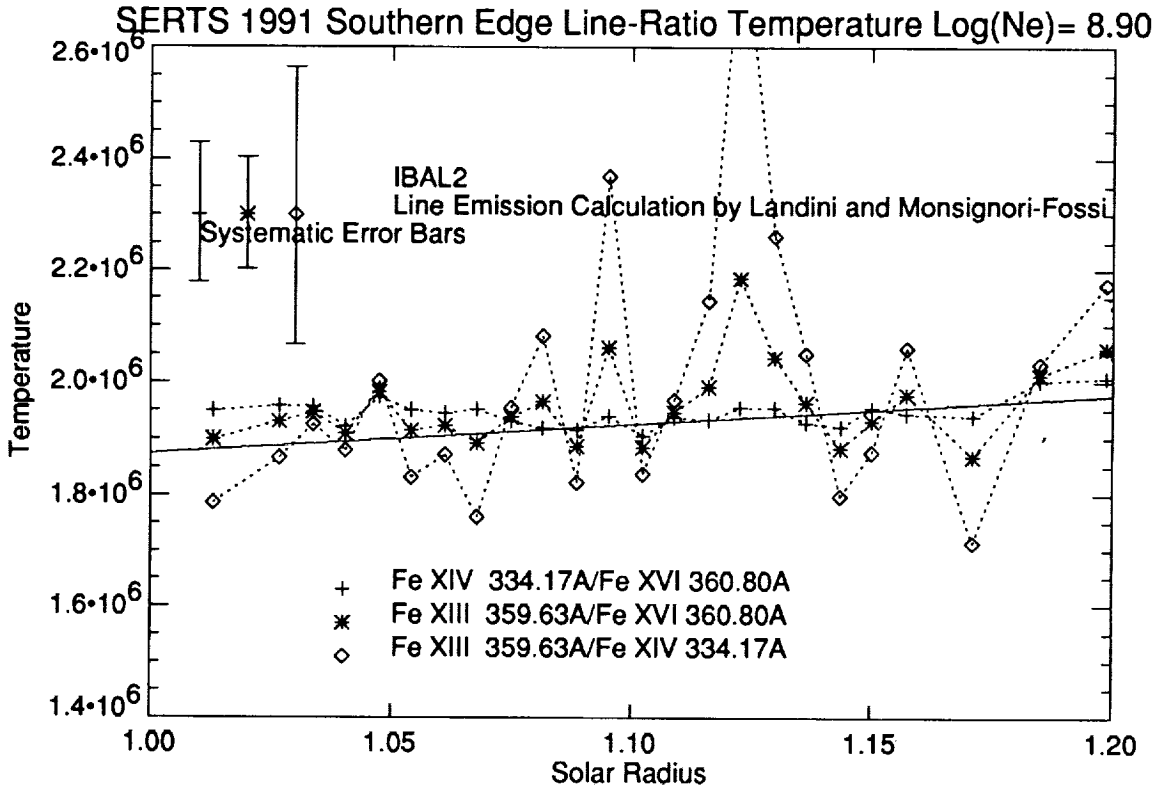


4.5a:

Figure 4.5. Same as Figure 4.4 using IBAL2. The differences between the two plots demonstrates the uncertainties due to the calculation of the contribution functions.

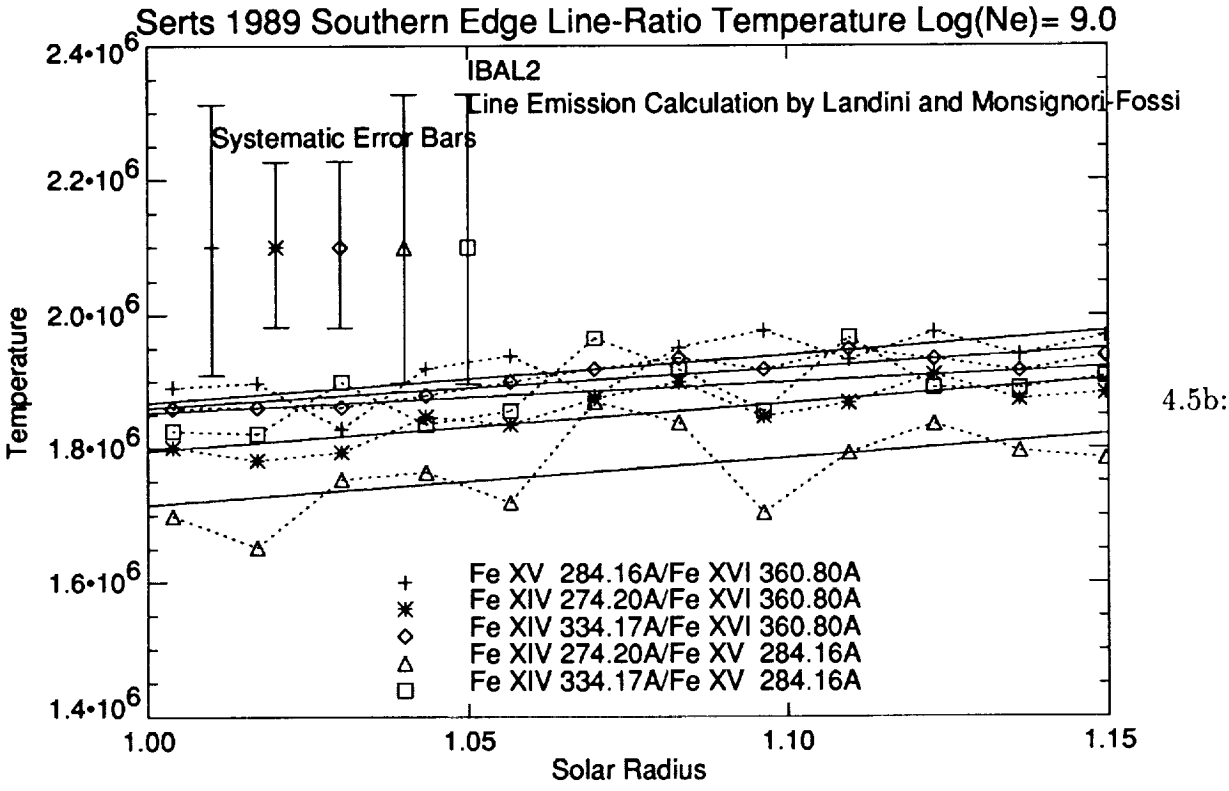


4.5b:

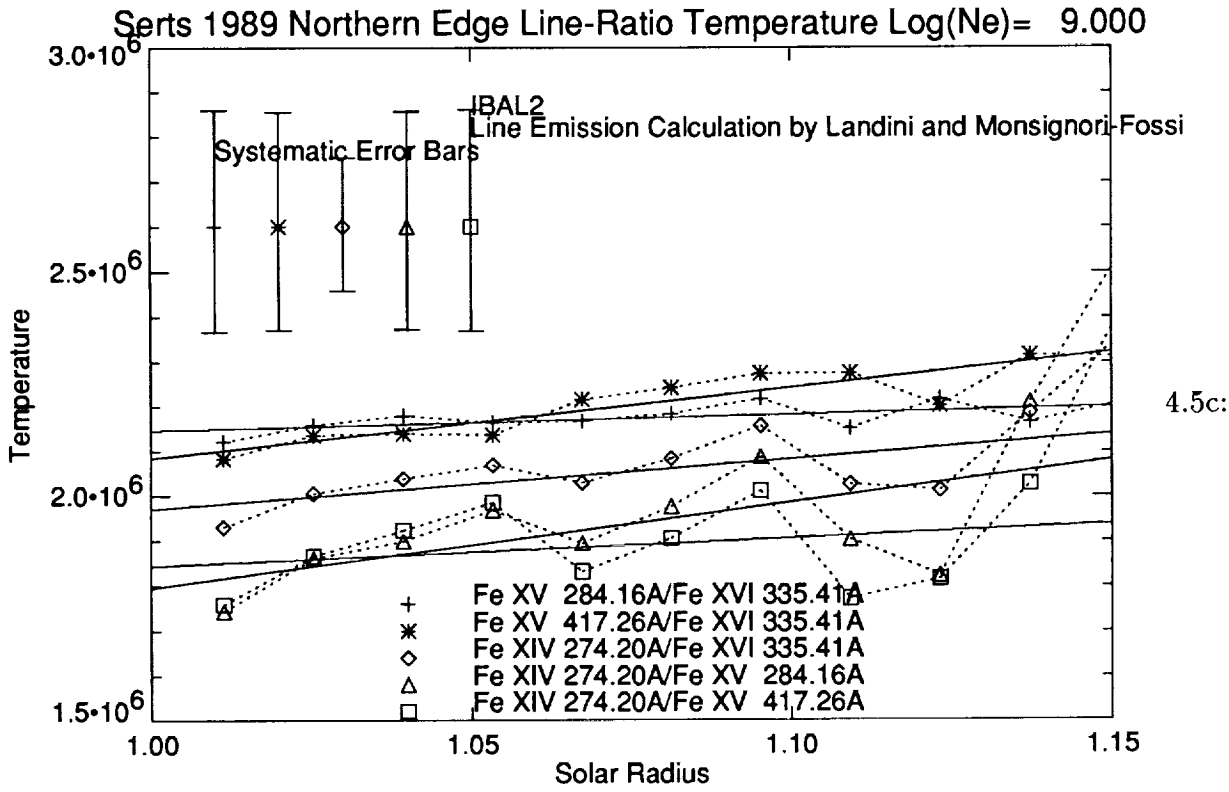


4.5c:

Figure 4.5 cont'd

ratio is decreased, and that determined from the Fe XIV 274 Å/Fe XV 284 Å ratio is increased compared to the same ratios containing Fe XV 417 Å. The effect of resonance scattering on Fe XV 284 Å is also discussed in Section 4.4.4.

The line-ratio temperature was also determined using the two Fe XIV lines from SERTS 1989 southern edge. Since the differences in the line-ratio temperatures are within the line-ratio temperature uncertainties (Figure 4.4b), the results are in reasonable agreement. The Fe XIV 274 Å spectral line would be influenced more by resonance scattering but line ratios involving Fe XIV 334 Å have a higher temperature and reduced slope. Therefore, there is no evidence that resonance scattering contributed to the differences in line-ratio temperatures containing Fe XIV.

For SERTS 1989 northern edge, the fit of the Fe XIV 274 Å to Fe XVI 335 Å line-ratio temperature was chosen as the best fit line-ratio temperature because of smaller uncertainties in $T_o$. For the southern edge, the average of the Fe XIV 334 Å to Fe XVI 361 Å and the Fe XIV 274 Å to Fe XVI 361 Å line-ratio temperature was used as the best fit line-ratio temperature. The uncertainties in $T_o$ and $a$ were similar except for the case of $a$ determined using IBAL2 (Table 4.4). In that case an uncertainty of $3 \times 10^5 K$ was used.

### 4.4.3 Comparison of Different Ionization Balance Calculations

Line-ratio temperatures determined by using either IBAL1 or IBAL2 are similar but do have systematic differences. For SERTS 1991 southern edge (Table 4.3), the line-ratio temperatures determined by using IBAL2 (compared to IBAL1) were on the average about 30,000K cooler. Also, it was found that the slope of the line-ratio temperature versus radius was smaller by 10-20%.

For SERTS 1989 data sets, the results are similar to that of the SERTS 1991. Except for the Fe XV/Fe XVI line-ratio temperature which was not available in the SERTS 1991 data set. The Fe XV/Fe XVI line-ratio temperature decreased more than other line-ratio temperatures when IBAL2 was used instead of IBAL1 (Tables 4.4 and 4.5). The result is a reduction in the spread of line-ratio temperatures when using IBAL2. Therefore, the line-ratio temperatures determined using IBAL2 are more self consistent. This would indicate that Arnaud and Rothenflug [3] ionization balance calculation for iron (IBAL2) is more accurate than the newer Arnaud and Raymond [2] ionization balance calculation (IBAL1). However, the uncertainties due to the possibility of temperature variation along the line of sight and also in the measurements are large enough so that IBAL1 can not be ruled out.

### 4.4.4 Comparison of Line-Ratio Temperatures and Scale Height

The variation in the density scale heights for different spectral lines (Table 4.2) can be reduced by removing the effect of the radial dependence of the line-ratio temperature. The next to the last column in Table 4.2 contains the predicted density scale height for each of the observed spectral lines using IBAL1, while the last column comes from IBAL2. The last row in each column is the "actual" density scale height which was used in modeling the predicted density scale heights.

The modeling was done as follows. The model first uses the least-squares fit of the line-ratio temperatures from Tables 4.3, 4.4, and 4.5 (parameters $T_o$ and $a$, defined in Equation 2.48) to calculate the contribution function, $Q$, of the different spectral lines as a function of radius. The observed density scale height from the spectral line for which the contribution function was nearly constant with radius was used as an initial guess to the "actual" density scale height. This "guess" was then used to predict the appar-

Table 4.3: Line-Ratio Temperature From SERTS 1991 Southern Edge

| Line Ratio | Avg. Temperature of Max. Abundance | | Range ($R_\odot$) | IBAL1[a,b,c] | | IBAL2[a,b,c] | |
|---|---|---|---|---|---|---|---|
| | T ($\times 10^6$) | Log(T) | | $T_o$ ($\times 10^6$) | $a$ ($\times 10^6$) | $T_o$ ($\times 10^6$) | $a$ ($\times 10^6$) |
| FeXIV 334/FeXVI 361 | 2.19 | 6.34 | 1.10-1.19 | 1.90±0.14 | 0.59±0.25 | 1.87±0.13 | 0.51±0.22 |
| FeXIII 359/FeXIV 334 | 1.70 | 6.23 | 1.05-1.19 | 1.98±0.34 | 0.68±1.69 | 1.95±0.32 | 0.62±1.56 |
| Best Fit | | | | 1.90±0.14 | 0.59±0.25 | 1.87±0.13 | 0.51±0.22 |

NOTES:

a. IBAL1 and IBAL2 defined in Table 4.1.

b. See Sections 2.5.2 and 4.4 for determination of error bars.

c. $N_e = 10^{8.9} cm^{-3}$

Table 4.4 Line-Ratio Temperature From SERTS 1989 Southern Edge

| Line Ratio | Avg. Temperature of Max. Abundance | | Range ($R_\odot$) | IBAL1[a,b,c] | | IBAL2[a,b,c] | |
|---|---|---|---|---|---|---|---|
| | T ($\times 10^6$) | Log(T) | | $T_o$ ($\times 10^6$) | $a$ ($\times 10^6$) | $T_o$ ($\times 10^6$) | $a$ ($\times 10^6$) |
| FeXV 284/FeXVI 361 | 2.19 | 6.36 | 1.02-1.15 | 1.94±0.25 | 0.95±0.33 | 1.87±0.20 | 0.72±0.25 |
| FeXIV 274/FeXVI 361 | 2.19 | 6.34 | 1.02-1.15 | 1.82±0.13 | 0.77±0.19 | 1.80±0.12 | 0.72±0.20 |
| FeXIV 334/FeXVI 361 | 2.19 | 6.34 | 1.02-1.15 | 1.89±0.14 | 0.64±0.19 | 1.71±0.12 | 0.70±0.43 |
| FeXIV 274/FeXV 284 | 1.95 | 6.29 | 1.02-1.15 | 1.71±0.21 | 0.69±0.19 | 1.85±0.23 | 0.46±0.33 |
| FeXIV 334/FeXV 284 | 1.95 | 6.29 | 1.02-1.15 | 1.85±0.22 | 0.45±0.19 | 1.85±0.22 | 0.46±0.33 |
| Best Fit | | | | 1.85±0.13 | 0.70±0.19 | 1.75±0.12 | 0.71±0.30 |

NOTES:
a. IBAL1 and IBAL2 defined in Table 4.1.
b. See Sections 2.5.2 and 4.4 for determination of error bars.
c. $N_e = 10^{9.0}$

Table 4.5 Line-Ratio Temperature From SERTS 1989 Northern Edge

| Line Ratio | Avg. Temperature of Max. Abundance | | Range ($R_\odot$) | IBAL1[a,b,c] | | IBAL2[a,b,c] | |
|---|---|---|---|---|---|---|---|
| | T ($\times 10^6$) | Log(T) | | $T_o$ ($\times 10^6$) | $a$ ($\times 10^6$) | $T_o$ ($\times 10^6$)[b] | $a$ ($\times 10^6$) |
| FeXV 284/FeXVI 335 | 2.29 | 6.36 | 1.02-1.15 | 2.29±0.33 | 0.44±0.26 | 2.15±0.26 | 0.36±0.21 |
| FeXV 417/FeXVI 335 | 2.29 | 6.36 | 1.02-1.15 | 2.21±0.30 | 1.91±0.44 | 2.08±0.24 | 1.59±0.34 |
| FeXIV 274/FeXVI 335 | 2.19 | 6.34 | 1.02-1.15 | 2.02±0.17 | 1.25±0.52 | 1.97±0.15 | 1.13±0.49 |
| FeXIV 274/FeXV 284 | 1.95 | 6.29 | 1.02-1.15 | 1.79±0.24 | 1.84±0.89 | 1.80±0.25 | 1.91±0.92 |
| FeXIV 274/FeXV 417 | 1.95 | 6.29 | 1.02-1.15 | 1.84±0.25 | 0.60±0.75 | 1.84±0.26 | 0.63±0.78 |
| Best Fit | | | | 2.02±0.17 | 1.25±0.52 | 1.97±0.15 | 1.13±0.49 |

NOTES:

a. IBAL1 and IBAL2 defined in Table 4.1.

b. See Sections 2.5.2 and 4.4 for determination of error bars.

c. $N_e = 10^{9.0}$

ent density scale height for the different spectral lines. The initial guess was adjusted until the differences between the apparent and observed density scale heights were minimized after allowances were made for the effect of resonance scattering (which acts to increase the apparent density scale height) on some lines.

The SERTS 1989 southern edge gave the best agreement, where differences between the observed and apparent density scale height were no greater than 0.01 $R_\odot$. The SERTS 1991 southern edge yielded similar agreement, except for Si XI, where the observed density scale height was 0.02 $R_\odot$ larger than was predicted. The SERTS 1989 northern edge had a larger observed density scale height than predicted from both Fe XV 284 and Fe XIV 274. The Fe XV 284, the Si XI 303, and to a lesser extent the Fe XIV 274 Å lines are the most susceptible to resonance scattering. "Actual" density scale heights from calculations using both IBAL1 and IBAL2 were the same except for the SERTS 1989 northern edge. The latter had the highest line-ratio temperatures, for which the differences between IBAL1 and IBAL2 were greatest.

For each observed region using IBAL1 and IBAL2, Table 4.6 gives the "actual" density scale height, the scale-height temperature, and the line-ratio temperature at 1.1 $R_\odot$. In these results the scale-height temperatures and the line-ratio temperatures are similar, but they can differ from each other by at least half a million degrees. In two of the cases the line-ratio temperature is higher, while in the third the scale-height temperature is larger. The primary reason for these differences is probably due to the assumption of spherical symmetry which is not completely correct. Secondary reasons for these differences can be turbulence, non-hydrostatic conditions such as flows, and divergence of the magnetic field, all of which are nonthermal effects which can change the "actual" density scale height. It should be pointed out that, except for determining the spectral line contribution functions, that the two temperatures were independently determined.

The results from this section indicate that the best lines for obtaining density scale heights are spectral lines that have a contribution function with at most a weak temperature dependence in the range of interest, and which are not strongly affected by resonance scattering. Then radial variation of the coronal temperature will have minimal effect on the inferred scale height. The scale-height temperatures from such lines, for example Fe XIII and Fe XIV in these data sets, can be used to give a reasonable estimate of the coronal temperature.

## 4.5 Emission Measure

The emission measure defined earlier in Equation (2.39) can now be determined for each observed spectral line in the three data sets as described in Section 2.5.3. The contribution function was evaluated using the least-squared fit line-ratio temperature given in Table 4.3, using IBAL1. The error factor of the emission measure is given for each spectral line and is not dependent on which elemental abundance is assumed. The effects of using IBAL2 will also be discussed.

The emission measures are plotted in Figure 4.6. Meyer's 1985 set of elemental abundances [38] was used except for the chromium elemental abundances where Stone's elemental abundance [53] was used, since Meyer does not provide the chromium abundance. The emission measures at 1.05 $R_\odot$ are given in Table 4.7 for four different sets of elemental abundances. The main difference is that the emission measures determined from Meyer's 1992 set of elemental abundances [40] are 3.5 times smaller than for the other three sets of elemental abundances.

For the SERTS 1991 southern edge the emission measures determined for Fe XIII and Fe XIV (Figure 4.6a) are in good agreement. The emission measure from Fe XVI above 1.08 $R_\odot$ was also in good agreement with the Fe XIII and Fe XIV emission measures, but it was larger be-

Table 4.6: Comparison of Scale-Height Temperature and Line-Ratio Temperature

| Observation | IBAL1[a] | | | IBAL2[a] | | |
|---|---|---|---|---|---|---|
| | "Actual" Scale Height[b] | Scale-Height Temperature | Line-Ratio Temperature | "Actual" Scale Height[b] | Scale-Height Temperature | Line-Ratio Temperature |
| SERTS 1991 South | 0.100 | $1.4\times10^6$ | $1.96\pm0.05\times10^6$ | 0.100 | $1.4\times10^6$ | $1.93\pm0.05\times10^6$ |
| SERTS 1989 South | 0.125 | $1.7\times10^6$ | $1.91\pm0.05\times10^6$ | 0.125 | $1.7\times10^6$ | $1.88\pm0.05\times10^6$ |
| SERTS 1989 North | 0.160 | $2.2\times10^6$ | $2.14\pm0.08\times10^6$ | 0.180 | $2.5\times10^6$ | $2.08\pm0.08\times10^6$ |

NOTES:

a. IBAL1 and IBAL2 defined in Table 4.1.

b. No uncertainties were assigned to the "actual" scale heights which were determined from modeling.

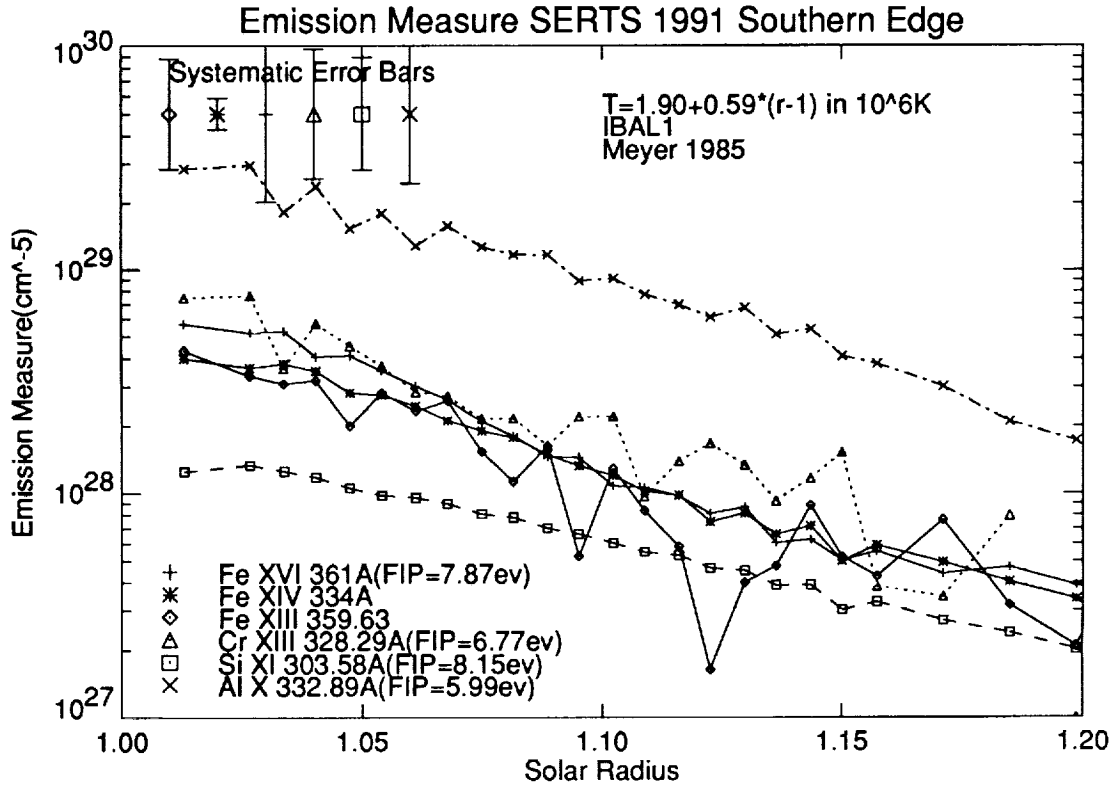


4.6a:

Figure 4.6. The emission measures plotted as a function of radius are shown for SERTS 1991 southern edge (4.6a), SERTS 1989 southern edge (4.6b), and SERTS 1991 northern edge (4.6c). This plot uses the line-ratio temperature determined from Figure 4.4 using IBAL1. The systematic error bars for each emission measure are shown in the upper left hand corner with a symbol in the center corresponding to the appropriate emission line. In Figure 4.6, the emission measure for Fe XVI is larger than for the other iron lines due to the hot loop. The dips in the Fe XIII emission measure near 1.09 and $1.12 R_{\odot}$ are probably due to the uncertainties in the background subtraction.

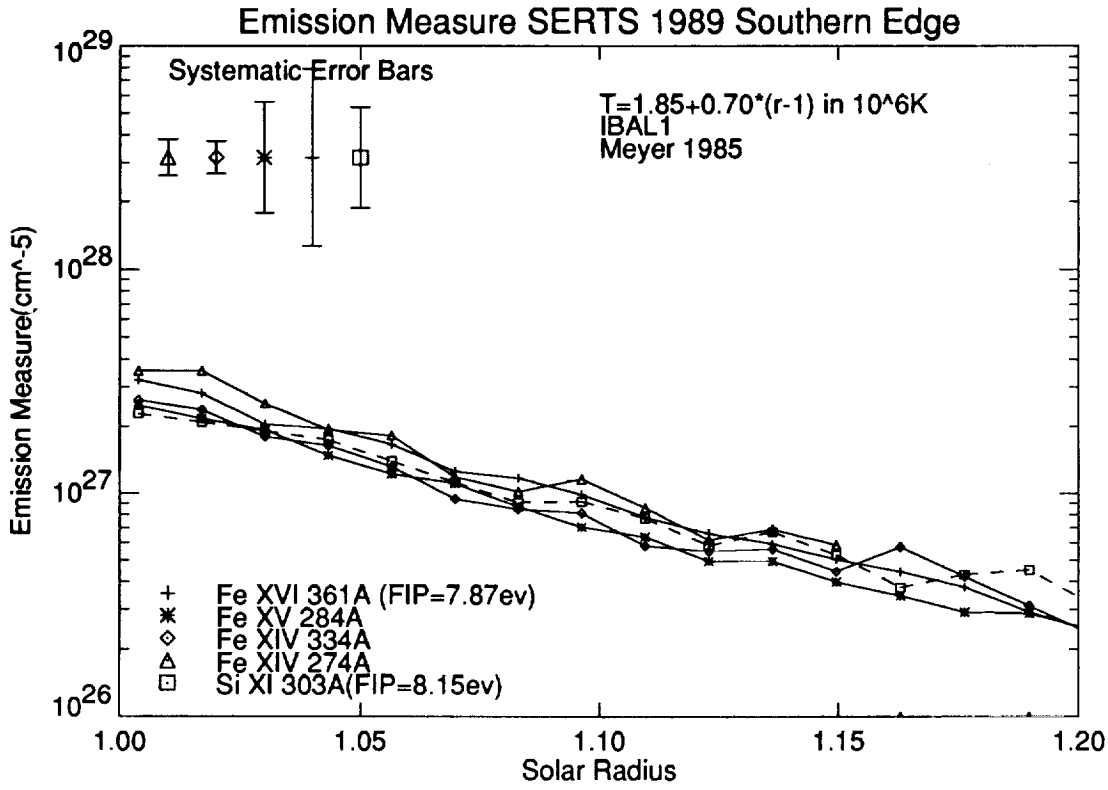


4.6b:

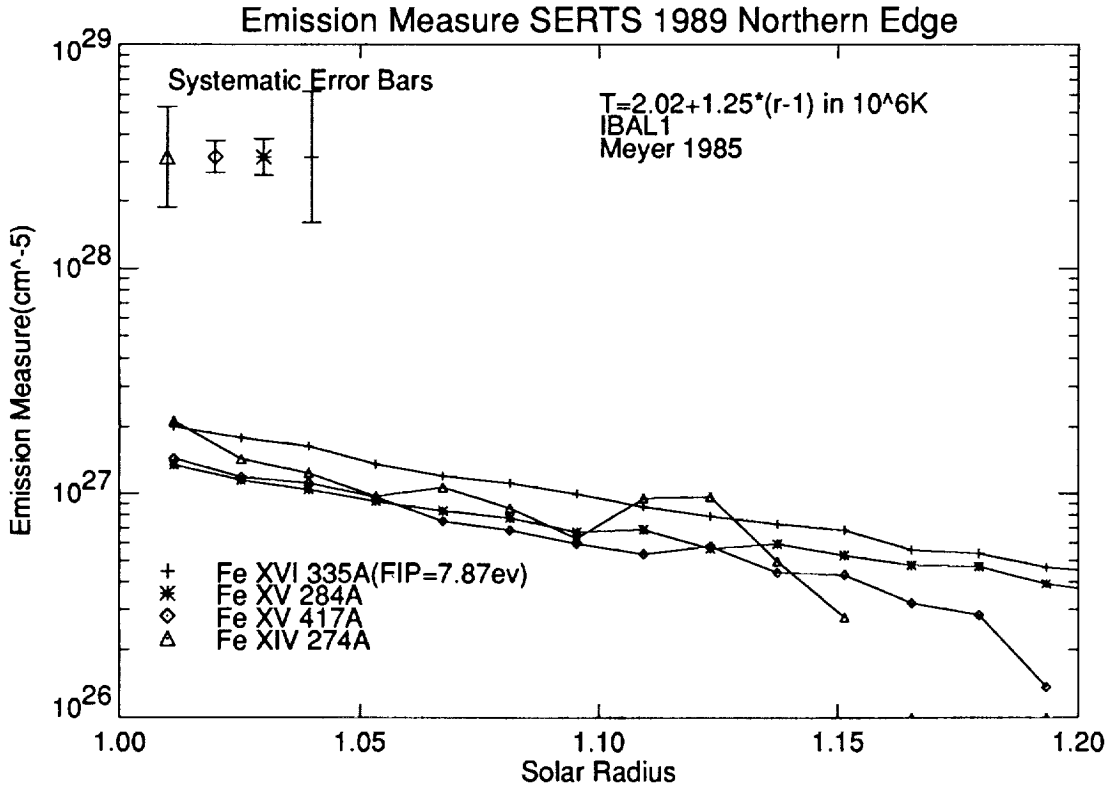


4.6c:

Figure 4.6 cont'd

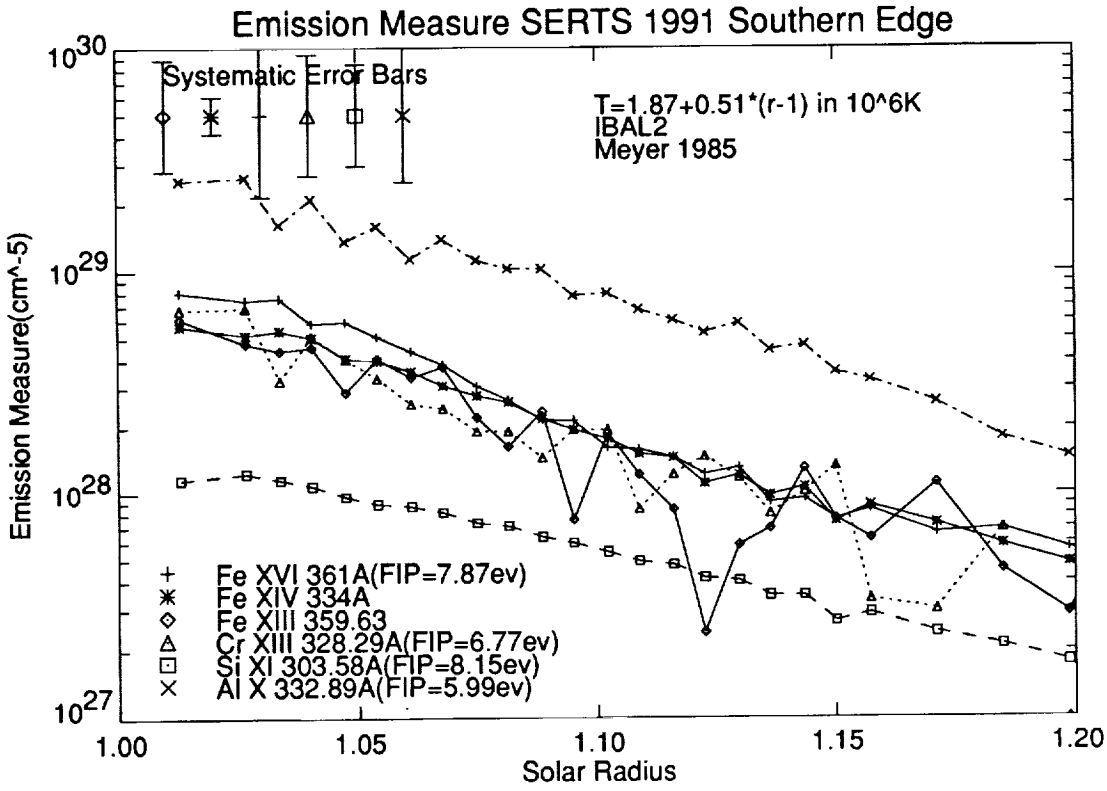


4.7a:

Figure 4.7. The same as Figure 4.6 except IBAL2 was used.

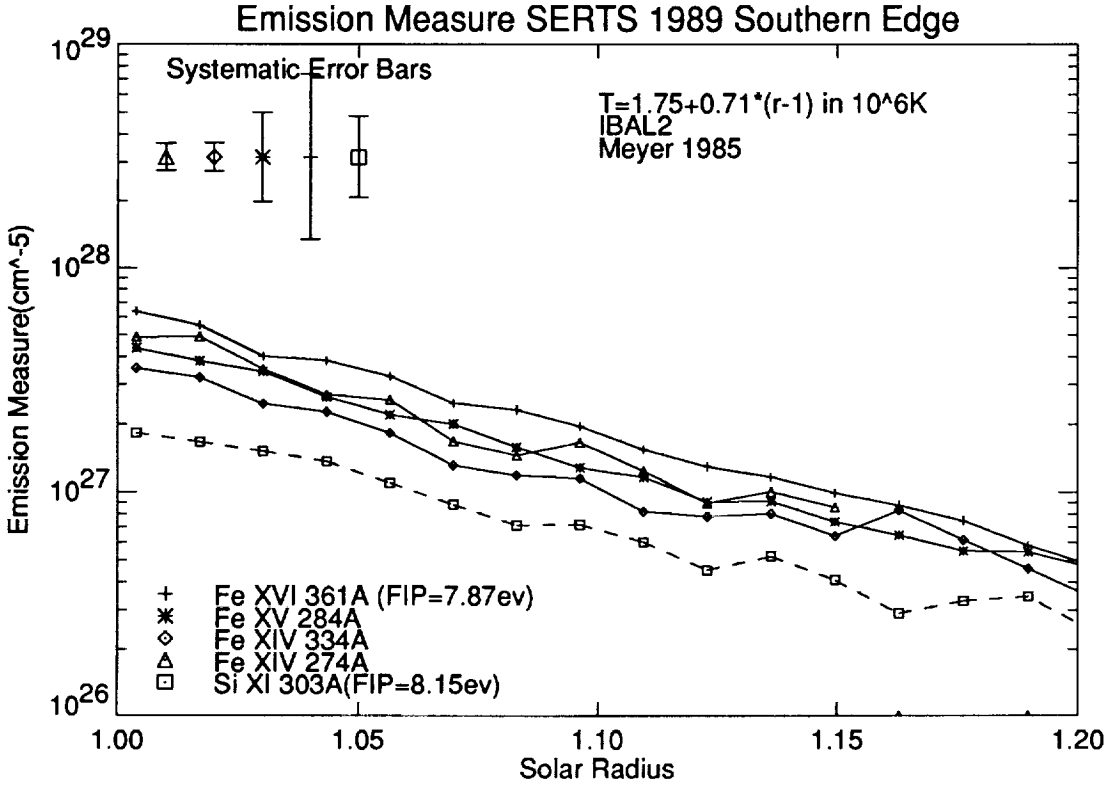


4.7b:

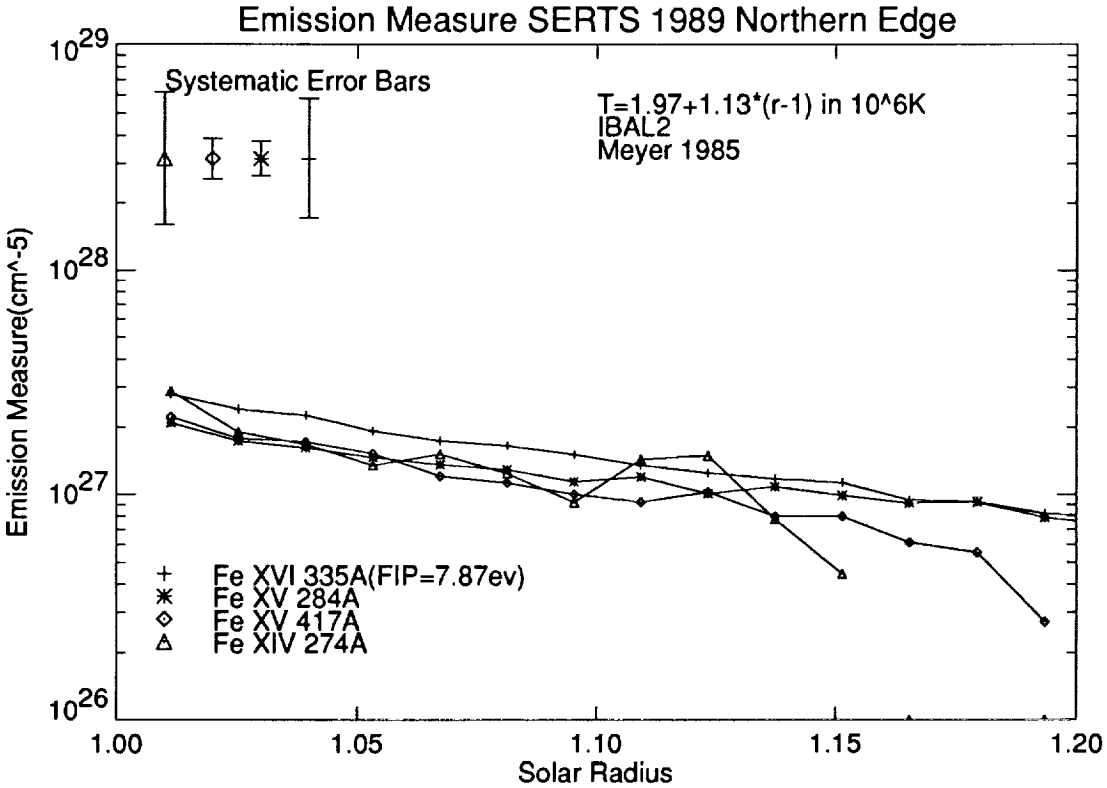


4.7c:

Figure 4.7 cont'd

low 1.08 $R_\odot$. This increase in emission measure of Fe XVI close to the Sun is due to the hot loop (Section 3.3.2) which emits weakly in the other "cooler" spectral lines. The emission measures from spectral lines from other elements show the same general radial dependence as iron, but have different overall normalizations. This result will be discussed in greater detail in Section 4.6.

Emission measures for SERTS 1989 are plotted in Figures 4.6b and 4.6c. The spread of the iron emission measures is less than the relative calibration uncertainties shown in the figure. The silicon emission measure from SERTS 1989 southern edge agrees well with the iron emission measures.

Calculations using IBAL2 produced an iron emission measure 30% larger than for IBAL1. Since the line-ratio temperatures determined from IBAL1 are systematically higher than for IBAL2, the emission measures of the other elements decreased by 10% for a total change of roughly 40% for IBAL1 compared to IBAL2.

## 4.6 Relative Elemental Abundances

The most probable explanation for the SERTS 1991 southern edge having different emission measures for different elements was that the observed coronal elemental abundances were different from those given by Meyer 1985 [38] (for Si and Al) and Stone [53] (for Cr), which were used in deriving the emission measures. If we divide all the emission measures as a function of radius by the Fe XIV 334 emission measure we have Figure 4.8a (IBAL1) and Figure 4.9a (IBAL2) (see Section 2.5.4 for method and discussion of uncertainties). In this representation, differences from Meyer 1985 set of elemental abundances show up as offsets from a horizontal straight line at y=1.0. For SERTS 1991 southern edge (Figure 4.8a and 4.9a) the Cr XIII and the Al X elemental abundances are high, while the silicon relative abundance is low. The chromium and aluminum relative elemental abundances are roughly constant with radius, while the silicon elemental abundance appears to increase with radius. This later apparent increase is probably due to the increasing importance of resonance scattering with height for the Si XI line (Section 4.4.4), rather than a real change of relative elemental abundance with height. The observed relative elemental abundances are given in Table 4.8 for both IBAL1 or IBAL2, and compared with other published abundances for Si, Fe, Cr, and Al.

One possible explanation for the apparent overabundance of aluminum in SERTS 1991 was a large amount of cooler ($\approx 1 \times 10^6$ $K$) plasma along the line of sight. One problem with this explanation is that cool plasma would also cause excess emission of Cr XIII, Si XI, and Fe XIII spectral lines, which is not seen. Also, the scale height of the cool, unobserved plasma, would need to be the same as for the observed plasma. Some rough estimates to explain just the aluminum abundance would require an emission measure of approximately the same amount at $1 \times 10^6$ $K$ as at $2 \times 10^6$ $K$, which can be ruled out based on the low flux in the other low-temperature spectral lines.

For the SERTS 1989 flight, only the relative abundance of silicon-to-iron can be determined because the lines from other elements were too weak to observe. The results are given in Figure 4.8b for IBAL1 and Figure 4.9b for IBAL2. The silicon-to-iron ratio does agree with Meyer 1985 [38], using the same emission lines for which SERTS 1991 implied a low silicon-to-iron ratio.

An estimate of the aluminum to iron relative abundance can be made for SERTS 1989 southern edge. In Figure 4.10, SERTS 1989 spectra at 1.1 $R_\odot$ are compared to the SERTS 1991 spectra scaled by the relative emission measures and taking into account the different line-ratio temperatures. The SERTS 1989 aluminum emission shows up at the three sigma level of the background noise which is the solid horizontal line crossing the figure. The aluminum intensity is

Table 4.7. Emission Measure

At $1.05R_{\odot}$ in units of $10^{27}cm^{-5}$ assuming IBAL1[d]

Table 4.7a: SERTS 1991 Southern Edge for T(r)=1.90e6+0.59e6*(r-1)

| Elemental Abundances | Fe XVI | Fe XIV | Fe XIII | Cr XIII | Si XI | Al X |
|---|---|---|---|---|---|---|
| Allen [1] | 10.7 | 11.9 | 12.7 | 17.9 | 7.1 | 102. |
| Meyer 1992 [40] | 3.2 | 3.6 | 3.8 | —-[c] | 1.7 | 21.1 |
| Meyer 1985 [38] | 10.8 | 12.0 | 12.9 | —-[c] | 6.0 | 91.5 |
| Stone [53] | 10.7 | 11.9 | 12.7 | 22.1 | 7.5 | 95.7 |
| Error Factor[a] | 1.23 | 1.15 | 1.26 | 1.17 | 1.18 | 1.19 |

NOTES

a. The error factor ("within a factor of ...") is a combination of the instrument uncertainty and the uncertainty due to the line-ratio temperature. It does not include the absolute flux uncertainty of a factor of 2. In addition, the ionization balance calculations and emissivity calculations could have a worst case uncertainty as large as a factor of 2, which is not included in Table 4.7. This latter uncertainty however, will not be independent of the temperature uncertainties. Since the uncertainties in the temperature and in the ionization balance and the emissivity are interconnected, we can reasonable replace the error factor in the above table by a factor of 2, which can then be viewed as an upper limit on the total uncertainty.

b. The Stone set of elemental abundances [53] does not contain hydrogen, $\log(N_{Fe}/N_H)$ was set to the value in Allen [1] of -4.4 for comparison.

c. The Meyer papers [38, 40] do not have an abundance for chromium.

d. IBAL1 defined in Table 4.1.

Table 4.7 cont'd: Emission Measure

At $1.05R_{\odot}$ in units of $10^{27}cm^{-5}$ assuming IBAL1[d]

Table 4.7b: SERTS 1989 Southern Edge for T(r)=1.84e6+0.70e6*(r-1)

| Elemental Abundances | Fe XVI 361 | Fe XV 284 | Fe XIV 274 | Fe XIV 334 | Si XI |
|---|---|---|---|---|---|
| Allen | 1.03 | 0.72 | 0.94 | 0.72 | 1.06 |
| Meyer 1992 | 0.31 | 0.22 | 0.28 | 0.22 | 0.26 |
| Meyer 1985 | 1.04 | 0.73 | 0.95 | 0.73 | 0.90 |
| Stone[c] | 1.03 | 0.72 | 0.94 | 0.72 | 1.12 |
| Error Factor[a] | 1.56 | 1.31 | 1.15 | 1.16 | 1.27 |

Table 4.7c: SERTS 1989 Northern Edge for T(r)=2.02e6+1.25e6*(r-1)

| Elemental Abundances | Fe XVI 335 | Fe XV 284 | Fe XV 417 | Fe XIV 274 |
|---|---|---|---|---|
| Allen | 0.985 | 0.662 | 0.586 | 0.619 |
| Meyer 1992 | 0.295 | 0.198 | 0.176 | 0.185 |
| Meyer 1985 | 0.997 | 0.671 | 0.594 | 0.627 |
| Stone[b] | 0.985 | 0.662 | 0.586 | 0.619 |
| Error Factor[a] | 1.63 | 1.24 | 1.22 | 1.48 |

NOTES

a. The error factor ("within a factor of ...") is a combination of the instrument uncertainty and the uncertainty due to the line-ratio temperature. It does not include the absolute flux uncertainty of a factor of 2. In addition, the ionization balance calculations and emissivity calculations could have a worst case uncertainty as large as a factor of 2, which is not included in Table 4.7. This latter uncertainty however, will not be independent of the temperature uncertainties. Since the uncertainties in the temperature and in the ionization balance and the emissivity are interconnected, we can reasonable replace the error factor in the above table by a factor of 2, which can then be viewed as an upper limit on the total uncertainty.

b. The Stone set of elemental abundances [53] does not contain hydrogen, $\log(N_{Fe}/N_H)$ was set to the value in Allen [1] of -4.4 for comparison.

c. IBAL1 defined in Table 4.1.

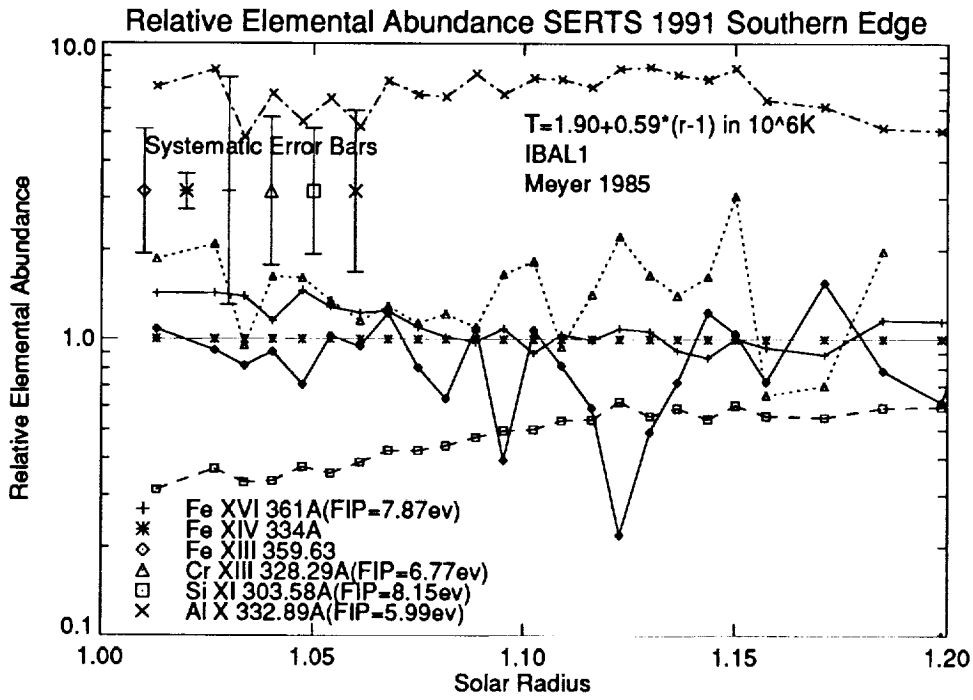


4.8a:

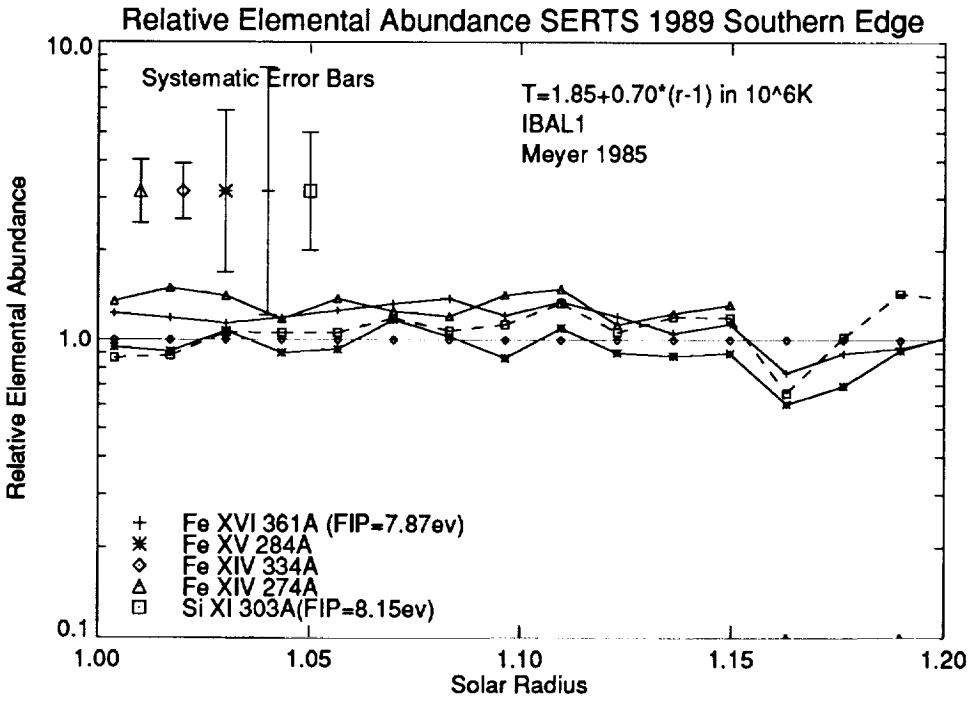


4.8b:

Figure 4.8. Plots of the relative elemental abundance for SERTS 1991 southern edge (4.8a), and SERTS 1989 southern edge (4.8b) using IBAL1. These plots used the emission measures determined earlier divided by the emission measure of the Fe XIV line for Figure 4.8a and the Fe XV for Figure 4.8b. The systematic error bars are shown in the upper left hand corner.

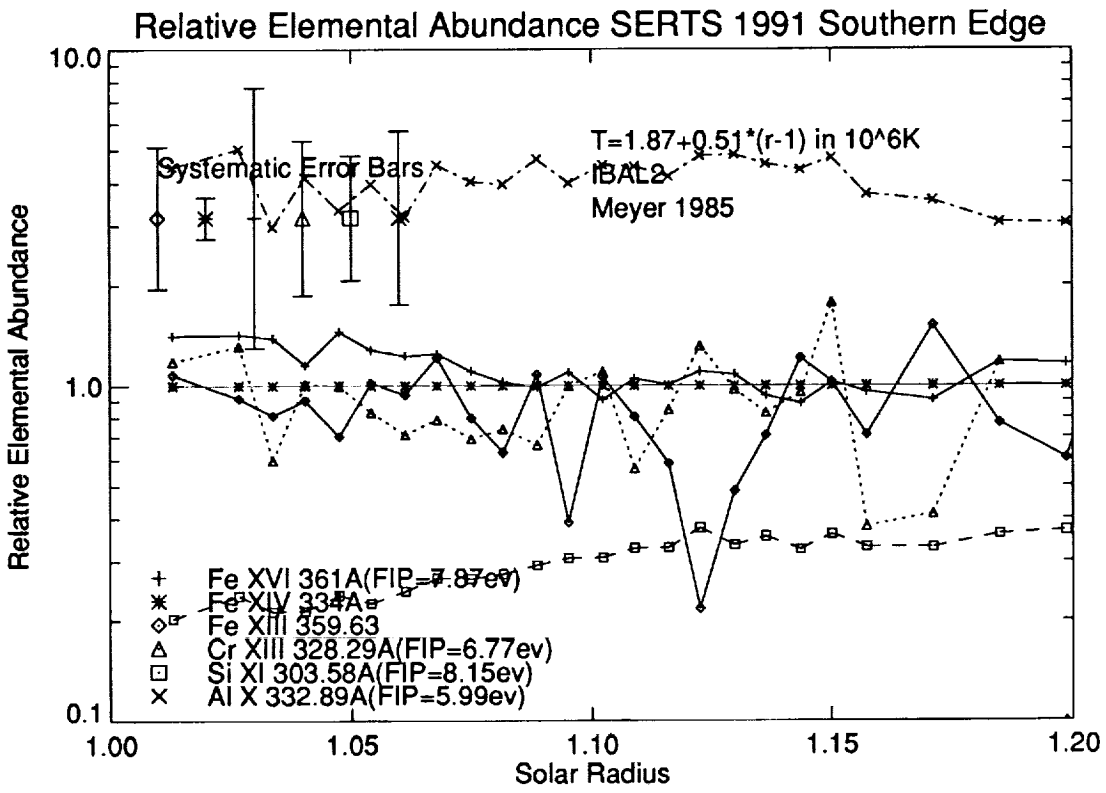


4.9a:

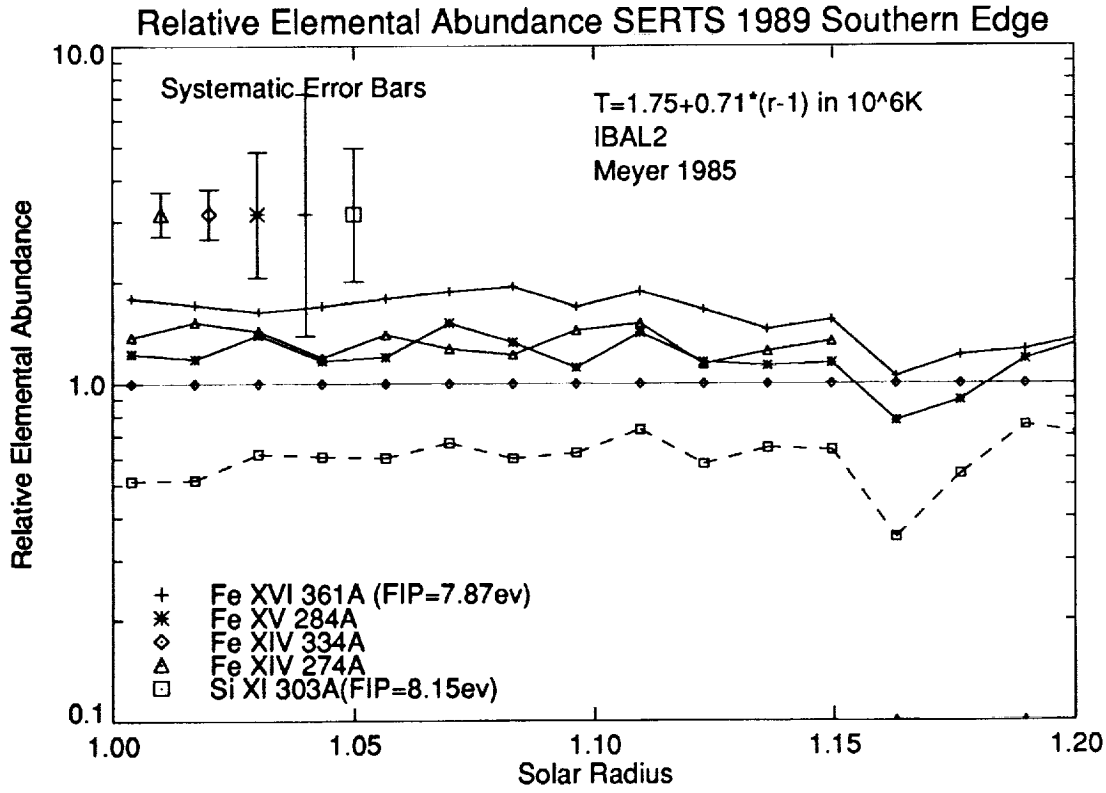


4.9b:

Figure 4.9. The same as Figure 4.8 except using IBAL2.

$0.63 \pm 0.21$ of the scaled SERTS 1991 aluminum intensity. Part of the SERTS 1989 aluminum intensity probably comes from cooler emissions which can be determined by noting that the SERTS 1989 emission in the 320 to 325 Å region is greater than the scaled SERTS 1991 intensity in the same region. The 320 to 325 Å region has lobes from Si VIII and Mg VIII lines which have temperatures of maximum abundance at 800,000K. Plasma at this temperature would also emit Al X 332 Å. Therefore, the SERTS 1989 southern edge aluminum abundance is probably even less than the upper limit ($0.63 \pm 0.21$ of the aluminum abundance determine for SERTS 1991) determined from Figure 4.10.

We discussed the importance of the FIP of different elements and why one might expect a differential abundance between high and low FIP elements separated in the chromosphere, in Section 2.2. It is interesting that, for the SERTS 1991 southern edge, the relative elemental abundances increase for elements of decreasing FIP. The Meyer 1985 set of coronal abundances [38] has low-FIP elements (below $< 10eV$) more abundant than the high-FIP elements by a constant enhancement factor, when compared to photospheric abundances. All of the spectral lines analyzed come from low-FIP elements, but instead of a simple step function describing the abundance variations as Meyer suggested, an enhancement dependent on FIP exists for the SERTS 1991 southern edge. However, the SERTS 1989 southern edge set of elemental abundances indicates a constant enhancement factor.

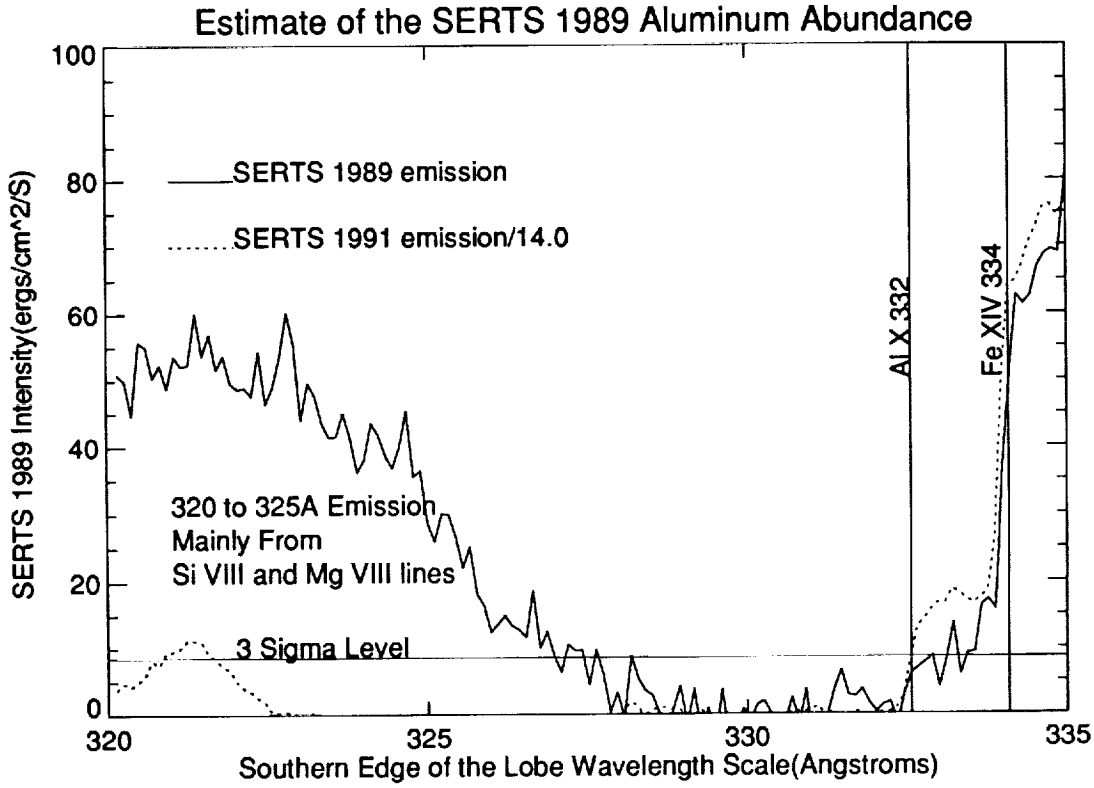


Figure 4.10. The 320 Å to the 335 Å spectrum from SERTS 1989 (solid) and SERTS 1991 (dotted), where the SERTS 1991 intensity was divided by a factor of 14.0 due to the differences in the emission measures and the effect of the line-ratio temperatures on the aluminum contribution function. The Al X 332 Å and the Fe XIV 334 Å are detectable in both plots with a vertical line indicating the edge of the lobe. The horizontal line indicates the 3-sigma level detection above the background for a lobe which is nine pixels (50 by 50 $\mu m$ pixels) wide. If the aluminum abundances for the two flights were the same, the SERTS 1989 and the SERTS 1991 intensities would be in agreement. Since the SERTS 1989 intensity is less, the aluminum abundance is less for SERTS 1989. The aluminum line can be efficiently produced by a one million degree plasma. The SERTS 1989 seems to have relatively more million degree plasma than SERTS 1991, since the 320 to 325 Å region has relatively more emissions where a number of Si VIII and Mg VIII spectral-line lobes exist. Therefore, this is an upper limit on the SERTS 1989 aluminum abundance.

Table 4.8: Relative Elemental Abundances

| Element | FIP (eV) | Observed | | | | Literature | | | |
|---|---|---|---|---|---|---|---|---|---|
| | | IBAL1[b] | | IBAL2[b] | | | | | |
| | | SERTS 1991 | SERTS 1989 | SERTS 1991 | SERTS 1989 | Allen [1] | Meyer[c] 1992 [40] | Meyer 1985 [38] | Stone [53] |
| Silicon | 8.15 | 345(1.24) | 709(1.28) | 221(1.23) | 489(1.28) | 832 | 1000 | 1031 | 787 |
| Iron | 7.87 | 1000 | 1000 | 1000 | 1000 | 1000 | 1000 | 1000 | 1000 |
| Chromium | 6.77 | 21.1(1.24) | — | 12.7(1.23) | — | 17.8 | —[a] | —[a] | 14.4 |
| Aluminum | 5.55 | 496(1.25) | — | 295(1.24) | — | 62 | 70 | 90 | 66 |



NOTES:

a. Meyer [38,40] does not list the chromium elemental abundance

b. IBAL1 and IBAL2 defined in Table 4.1.

c. Private Communication

d. The error factor ("within a factor of ...") are in the parentheses. The error factor is a combination of the instrument uncertainty and the uncertainty due to the line-ratio temperature. It does not include the absolute flux uncertainty of a factor of 2. The ionization balance calculations and emissivity calculations could have an uncertainty of as large as a factor of 2.8 which is not included and would replace the above uncertainty since they would not be entirely independent.

# Chapter 5

# Implications of the Coronal Parameters

The coronal parameters determined in Chapter 4 have implications for determining the filling factor, minimum electron density, and heating requirements for the solar corona, and will be discussed in the following sections.

## 5.1 Filling Factor and Minimum Electron Density

Since the emission measure is determined over a field of view times a depth, the small scale structures are averaged in this observed volume. While the line-ratio density determines the weighted average density of the emitting structures, the latter may not completely fill the potentially observed volume. The filling factor is the volume of the emitting structures divided by the observed volume. If the filling factor is less than unity, then only a fraction of the observed volume is filled with plasma emitting in the observed wavelength. If the filling factor is one, the observed volume is uniformly filled.

The average of the electron density squared, $\overline{N_e^2}$, is related to the emission measure by Equation (2.41), which can be rearranged as

$$\overline{N_e^2}(r') = \frac{\eta(r')}{f(r')L(r')}. \tag{5.1}$$

The minimum electron density necessary to explain the observed emission measure will then be

$$(N_e)_{min} \equiv \sqrt{\frac{\eta}{L}}. \tag{5.2}$$

The minimum electron density at 1.05 $R_\odot$ is given in Table 5.1. In the table the emission measures, $\eta$, determined in Section 4.5, and the density scale heights used to calculate $L$ were determined in Section 4.4.4, IBAL1, and the Meyer 1985 elemental abundances [38] were used. The minimum electron density using Meyer 1992 elemental abundances [40] would be reduced by a factor of 0.55.

The limits on the filling factor can be determined by comparing the minimum electron density and the limits on line-ratio density (Section 4.3). The line-ratio density is an average density along the line-of-sight and not the density at a single radial position. For an exponential atmosphere with a density scale height of less than 0.2 $R_\odot$, the line-ratio density times $\sqrt{2}$ would be the electron density at the point along a line-of-sight closest to the center of the Sun (Equation 2.37). Substituting Equation (5.2) into (5.1), the filling factor would then be

$$f = \frac{1}{2}\left(\frac{(N_e)_{min}}{\overline{N_e}}\right)^2 \tag{5.3}$$

where $\overline{N_e}$ is the line-of-sight density determined from the line-ratio density (Equation 2.36). The limits on the filling factor are given in the last column of Table 5.1.

Since the line-ratio density for SERTS 1991 below 1.1 $R_\odot$ was determined to be between $10^9$ and $10^{10} cm^{-3}$ (Section 4.3), this implies a filling factor between $6 \times 10^{-4}$ to $6 \times 10^{-2}$, for IBAL1 and Meyer 1985 elemental abundances [38]. The

filling factors for both SERTS 1989 southern and northern edges need to be greater than $3 \times 10^{-5}$ because of an upper limit on the line-ratio density of $10^{10} cm^{-3}$. The filling factors for SERTS 1989 are probably much greater than the lower limit, because the maximum density estimate is probably too high.

## 5.2 Heating

Since the corona is much hotter than the photosphere, the corona requires a source of energy to be deposited in it by some non-radiative mechanism or mechanisms. To estimate the energy deposited in the corona, one has to assess the energy leaving the corona by heat conduction to the transition region, the energy radiated away in the electromagnetic spectrum, and that deposited into the solar wind. If a steady state exists, the known energy leaving a region of the corona is equal to the energy deposited in that region. This estimate of the required energy deposition will then impose constraints on coronal heating models.

The temperature gradient in the lower corona causes heat conduction to transport energy to the transition region. Electron heat conduction ($F_c$) dominates the conduction at coronal temperatures, and along the magnetic field line. The conductive flux, according to Spitzer [51], is

$$F_c \approx 10^{-6} T^{2.5} \frac{dT}{dz} (ergs\ cm^{-2} s^{-1}) \qquad (5.4)$$

for a Maxwellian particle distribution. In equation (5.4) $T$ is the temperature, and $z$ is the distance along the magnetic field line. Across the field lines, the heat conduction is negligible. For example for $N_e = 10^9 cm^{-3}$, $B = 10$ gauss, and $T = 2 \times 10^6\ K$ the ratio of the conductive flux across magnetic field lines to along the field line is $10^{-10}$.

For the SERTS data, any change of heat conduction over the height observed was less than the uncertainty of the measurement. Limits on the change in heat conduction were determined by the following means. The electron heat conduction equation as a function of height can be written as a linear equation

$$F_c(z) = F_o + z\ F_c'. \qquad (5.5)$$

Substituting equation (5.4) for $F_c$

$$10^{-6} T^{2.5} \frac{dT}{dz} \approx F_o + z\ F_c' \qquad (5.6)$$

and integrating with respect to $z$

$$\frac{10^{-6}}{3.5} T^{3.5} \approx F_o z + z^2 \frac{F_c'}{2} + const \qquad (5.7)$$

$F_o$ can be determined from Equation 5.7 and the line-ratio temperature determined in Section 4.4. Then an upper limit on the divergence of heat flux, $F_c'$, (though zero change of heat conduction fits the data) can be determined. The results are given in Table 5.2.

Next, the radiation per unit volume must be estimated from the observations. The radiative power, $F_r$, can then be estimated from

$$F_r = \varepsilon_T(T) \overline{N_e^2}\ (erg\ cm^{-3} s^{-1}), \qquad (5.8)$$

where $\varepsilon_T$ is the total radiative loss function, which is a function of the temperature and the elemental abundances [9]. Substituting equation (5.1) for $\overline{N_e^2}$, equation (5.8) becomes

$$F_r = \varepsilon_T \eta(r) / f L(r, H_s). \qquad (5.9)$$

Unlike heat conduction, the radiation per unit volume of a structure depends on the filling factor, as indicated explicitly in the last column of Table 5.2.

The radiative loss function is tabulated by Cook [9] who used Meyer 1985 elemental abundances [38]. The radiative loss function can be relatively easily determined, using Cook's paper, for other sets of elemental abundances. Since iron is the primary emitter in the $2 \times 10^6$K temperature range, the value of $F_r$ will change by only 5-10% for the different sets of elemental abundances used in this dissertation.

Table 5.1. Minimum Electron Density and Filling Factor

| Data Set | Minimum Electron Density[a,b] | Line-Ratio Density | Filling Factor[a,b] |
|---|---|---|---|
| SERTS 1991 Southern Edge | $3.6 \pm 0.6 \times 10^8$ | $10^9$-$10^{10}$ | $0.0006 - 0.06$ |
| SERTS 1991 Southern Edge | $8.3 \pm 1.3 \times 10^7$ | $< 10^{10}$ | $> 3 \pm 1 \times 10^{-5}$ |
| SERTS 1989 Northern Edge | $7.4 \pm 1.2 \times 10^7$ | $< 10^{10}$ | $> 3 \pm 1 \times 10^{-5}$ |

NOTES:
a: For Meyer 1985 elemental abundances [38] and IBAL1.
b: A systematic uncertainty of a factor of 2.0 in the filling factor, and a factor of 1.4 for the minimum electron density exist because of the absolute calibration (Section 3.2.)

Table 5.2. Comparison of Radiation to the Divergence of the Heat Flux

| | range $R_\odot$ | $F_o \times 10^4$ $(erg/cm^2/s)$ | $F_c' \times 10^{-6}$ $(erg/cm^3/s)$ | $F_r \times 10^{-6}/f$ $(erg/cm^3/s)$ |
|---|---|---|---|---|
| SERTS 1991 south side | 1.1-1.2 | $6 \pm 2$ | $0 \pm 2$ | $45. \pm 9.$ |
| SERTS 1989 south side | 1.02-1.15 | $5 \pm 1$ | $0 \pm 1$ | $1.8 \pm 0.4$ |
| SERTS 1989 north side | 1.02-1.15 | $14 \pm 2$ | $0 \pm 2$ | $0.98 \pm 0.28$ |

Note: $F_r$ determined at 1.05 $R_\odot$. $F_o$, $F_c'$, and $F_r$ are respectively the constant part of the divergence of the heat conduction, divergence of the heat conduction, and the radiative power.

Since the temperature increases with radius (Figure 4.4), heating above the observed height range is needed. The energy deposited in the solar wind is an extra energy requirement of the energy deposited above the observed region.

In Figure 5.1, heating is shown to be necessary for at least part of the observed range for a filling factor of unity for SERTS 1989 southern edge and SERTS 1991 southern edge. Heating over the entire observed range for all three cases would be required for a filling factor of 0.1 or less. An upper limit on the filling factor of 0.06 was determined for SERTS 1991 southern edge (Table 5.1), while no upper limit for SERTS 1989 was determined. A filling factor of 0.1 or less is reasonable. For more discussion of the filling factor see Section 5.1.

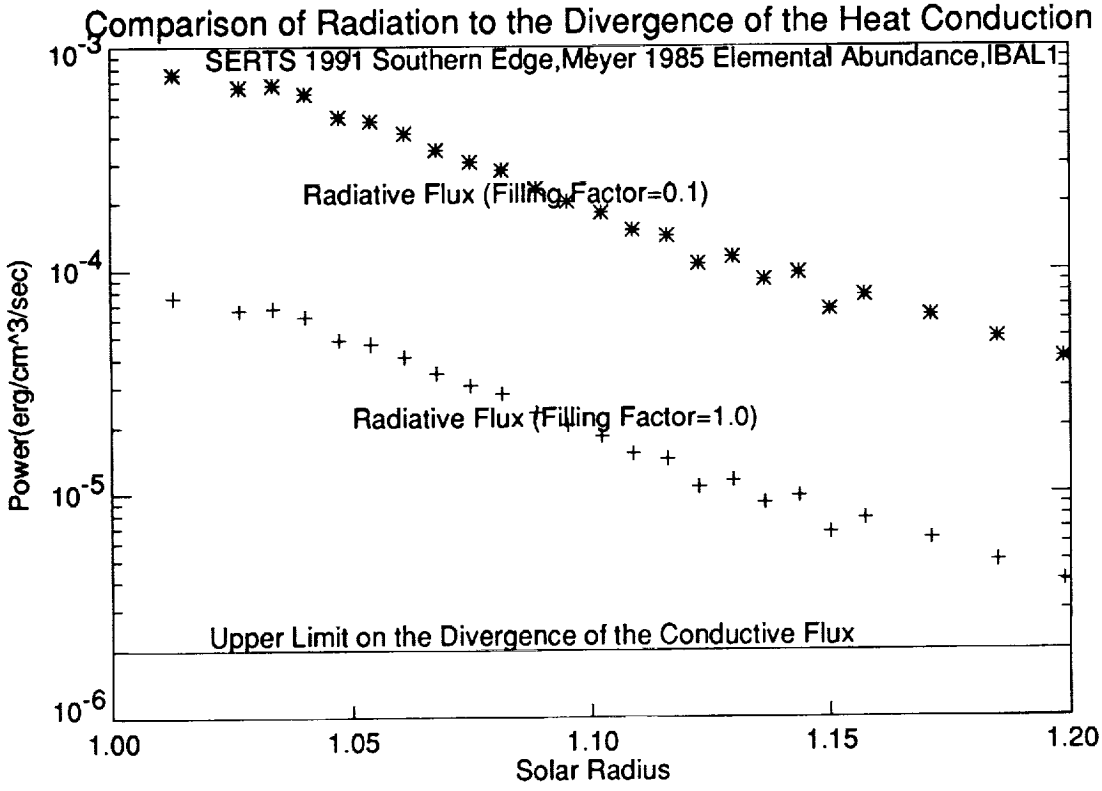


5.1a:

Figure 5.1. Heating Constraints
The heating constraints are shown for SERTS 1991 southern edge (5.1a), SERTS 1989 southern edge (5.1b), and SERTS 1989 northern edge (5.1c). The maximum heating of the corona by heat conduction (horizontal line) is compared to the radiative flux as a function of radius for a filling factor of unity (+) and 0.1 (asterisk).

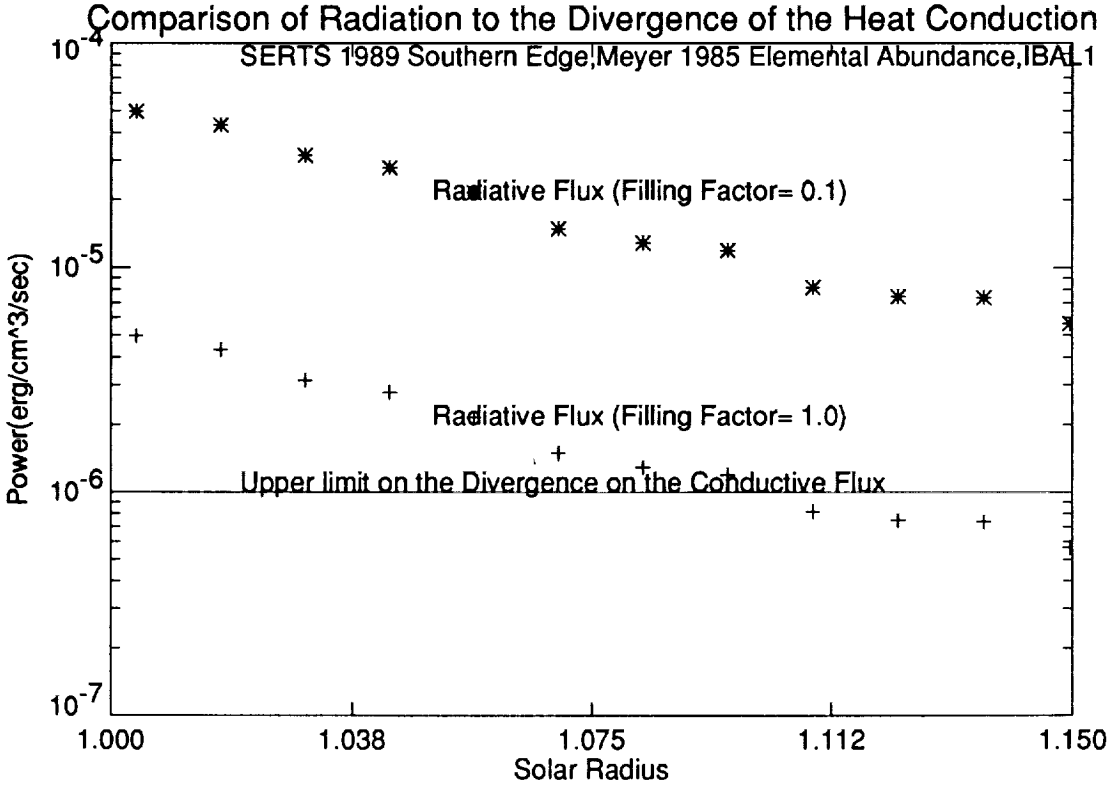
Comparison of Radiation to the Divergence of the Heat Conduction
SERTS 1989 Southern Edge,Meyer 1985 Elemental Abundance,IBAL1
Radiative Flux (Filling Factor= 0.1)
Radiative Flux (Filling Factor= 1.0)
Upper limit on the Divergence on the Conductive Flux
Power(erg/cm^3/sec)
Solar Radius
10^-4
10^-5
10^-6
10^-7
1.000
1.038
1.075
1.112
1.150

5.1b:

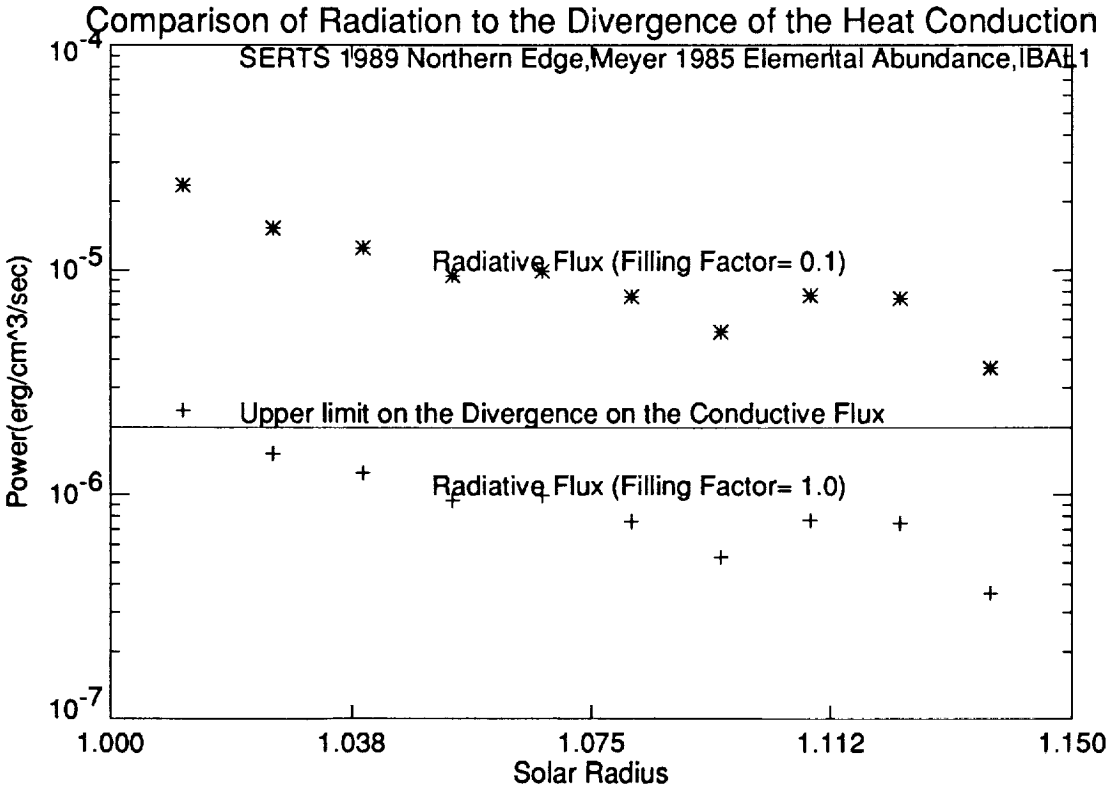
Comparison of Radiation to the Divergence of the Heat Conduction
SERTS 1989 Northern Edge,Meyer 1985 Elemental Abundance,IBAL1
Radiative Flux (Filling Factor= 0.1)
Upper limit on the Divergence on the Conductive Flux
Radiative Flux (Filling Factor= 1.0)
Power(erg/cm^3/sec)
Solar Radius
10^-4
10^-5
10^-6
10^-7
1.000
1.038
1.075
1.112
1.150

5.1c:

# Chapter 6

# Upper Limits on Bi-Maxwellian Electrons

A Maxwellian distribution for the electrons velocities has been assumed in the previous chapters of this dissertation since, given enough time, the electrons will reach a Maxwellian distribution in an isolated plasma. In this section we will determine if this is a good assumption for our analysis.

Bi-Maxwellian distributions can be produced if high-energy electrons, produced in one region of the atmosphere, travel to another region without undergoing collisions. This is due to their longer mean-free path. The mean-free path is

$$\lambda_{mfp} = \frac{1}{N\sigma} \tag{6.1}$$

where $\sigma$ is the cross section and $N$ is the density of particles. Scattering due to many cumulative small-angle scatterings is dominant. According to Krall and Trivelpiece [31] the cross section for 90° scattering due to many cumulative small-angle scattering events is

$$\sigma \approx \frac{2.6 \times 10^{-12}}{E^2} cm^2, \tag{6.2}$$

where $E$ is the particle kinetic energy in eV. So we get

$$\lambda_{mfp} \approx \frac{3.8 \times 10^{11} E^2}{N} cm. \tag{6.3}$$

The higher the energy of the electrons, the longer the mean free path will be. So, the high energy electrons produced by flares, nanoflares, or by other means in one region of the corona can propagate to another region of the corona about the distance of one mean-free-path. In the corona typical nonflaring kinetic energy for electrons is on the order of $200eV$; these electrons would have a mean-free-path of 150 $km$ for $N_e = 10^9 cm^{-3}$. Electrons produced in flaring regions where the thermal electrons could have kinetic energies of $1000eV$ would have a mean-free-path of 3800 $km$ for the same electron density this is still small compared to the hydrostatic scale height of $0.1R_\odot$ or 64,000 $km$. The high energy electrons then can have a nonlocal origin compared to the lower energy electrons.

This process could lead to a local bi-Maxwellian distribution of electrons with an excess number of high energy electrons for the local "mean" temperature. An upper limit on the excess number of high energy electrons can be determined both from theory and from observations. Limits determined from both methods are provided in this chapter.

The high-temperature electrons will loose energy by collisions on the time scale given by Spitzer [51] as the time of equipartition, reproduced below as Equation (6.28). For coronal conditions, this cooling time is on the order of tenth of a second. Since an equilibrium situation is assumed and the ionization balance time scales are on the order of tens of minutes, the limits apply to a continuous injection of high-energy electrons and not a single, transient injection of electrons.

## 6.1 Symbols

This chapter uses the same sets of symbols that are used in the rest of the dissertation except for the following. $Q_{X,Z}$ is the ionization cross section, $E$ is the kinetic energy of the electron, $a$ is the mixing fraction, $C$ and $D$ are fitting parameters, and $\overline{T_i}$ is the measured line-ratio temperature.

## 6.2 Observations

The effect of an excess number of high-energy electrons on the spectra will be analyzed to develop a diagnostic test. When an electron collides with an ion, in general, one or a combination of four things can happen to the ion:

1. The electron is elastically scattered with only kinetic energy transferred;
2. the ion can be excited;
3. the electron can be captured so the ionization stage of the ion will decrease; or
4. the electron can ionize the ion so the ionization stage of the ion will increase.

The higher the energy of the electron, the more likely possibility 4 will occur. So the addition of high-energy electrons will preferentially increase the ratio of a higher ionization stage compared to a lower ionization stage. This would have the effect of raising the apparent temperature of the plasma determined by line-ratio diagnostics (described in Section 2.5.2).

To model the effect on the ratio of intensities of spectral lines from different ionization stages we will make the following assumptions. The electron distribution will be modeled as a sum of two Maxwellian distributions

$$F_t(E, T_1, T_2, a) = (1 - a)F(E, T_1) + aF(E, T_2), \tag{6.4}$$

where $T_1$ and $T_2$ are the temperatures of a cool and a hot component respectively, and $a$ is the

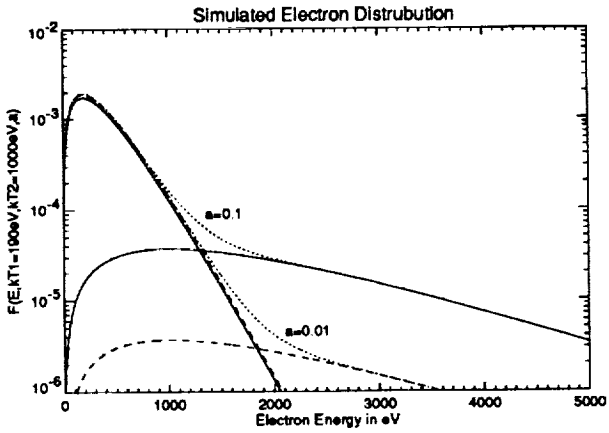


Figure 6.1. The net electron distributions for two Maxwellian components with $kT_1 = 190eV$ and $kT_2 = 2000eV$, respectively, for two mixing fractions ($a = 0.1$ is shown with a solid line and $a = 0.01$ with a dashed line, and the summations are shown as dotted lines).

mixing fraction of the two components (i.e., the fraction of the total number of electrons in the hotter component) (see Figure 6.1). $F(E, T_1)$ is a normal Maxwellian distribution written in energy space as

$$F(E, T_1) = \frac{E}{(kT_1)^2} exp\left(\frac{-E}{kT_1}\right). \tag{6.5}$$

A two-component electron distribution where each component is a Maxwellian makes the analysis readily tractable, and so is adopted only for illustration and to obtain a rough estimate on the excess number of electrons.

In steady state the number of ions being ionized needs to match the number of ions recombining, so neglecting double ionization or recombination (see Section 2.3.2) we have

$$N_{X,Z} q_{X,Z}(F(E)) = N_{X,Z+1} \alpha_{X,Z+1}(F(E)), \tag{6.6}$$

where $N_{X,Z}$ is the density of ionization stage $Z$ for element $X$, $q_{X,Z}(F(E))$ is the ionization rate, and $\alpha_{X,Z+1}F(E)$ is the recombination rate. Both $q_{X,Z}$ and $\alpha_{X,Z+1}$ are dependent on the electron energy distribution. Equation (6.6) can be rear-

ranged as

$$\frac{N_{X,Z+1}}{N_{X,Z}} = \frac{q_{X,Z}(F(E))}{\alpha_{X,Z+1}(F(E))}. \quad (6.7)$$

The addition of an excess number of high energy electrons will change $q_{X,Z}$ and $\alpha_{X,Z+1}$, so the ratio of densities of adjacent ionization stages will change. The ionization rate (see, e.q., Arnaud and Rothenflug [3]) is given by

$$q_{X,Z}(F(E)) = \int_0^\infty Q_{X,Z}(E)F(E)dE, \quad (6.8)$$

where F(E) is the electron distribution and $Q_{X,Z}$ is the total ionization cross section (Figure 6.2). Next, using the electron distribution given in Equation (6.4), we get

$$q_{X,Z}(T_1, T_2, a) = (1-a)\int_0^\infty Q_{X,Z}(E)F(E,T_1)dE + a\int_0^\infty Q_{X,Z}(E)F(E,T_2)dE. \quad (6.9)$$

Each integral can now be replaced using Equation (6.8) giving

$$q_{X,Z}(T_1, T_2, a) = (1-a)q_{X,Z}(T_1) + a\, q_{X,Z}(T_2), \quad (6.10)$$

where $q_{X,Z}(T_1)$ and $q_{X,Z}(T_2)$ are the ionization rates over a single Maxwellian distribution and can be determined, for example, by using Arnaud and Rothenflug [3] or Arnaud and Raymond [2] calculations and $q_{X,Z}(T_1, T_2, a)$ is the ionization rate for the electron distribution given in Equation (6.4).

Equation (6.10) can be rearranged to give

$$\frac{q_{X,Z}(T_1, T_2, a)}{q_{X,Z}(T_1)} = 1 + a\left(\frac{q_{X,Z}(T_2)}{q_{X,Z}(T_1)} - 1\right). \quad (6.11)$$

Next, $\gamma_q$ is defined as

$$\gamma_q(T_1, T_2) = \frac{q_{X,Z}(T_2)}{q_{X,Z}(T_1)} - 1. \quad (6.12)$$

So, Equation (6.11) becomes

$$\frac{q_{X,Z}(T_1, T_2, a)}{q_{X,Z}(T_1)} = 1 + a\gamma_q(T_1, T_2). \quad (6.13)$$

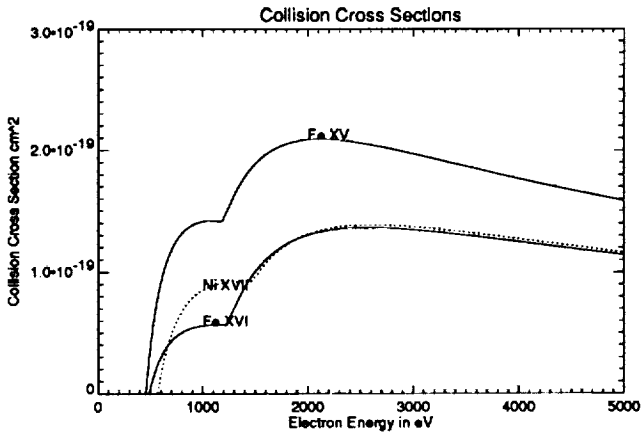


Figure 6.2. The ionization cross section as a function of energy shown for Fe XV, Fe XVI (solid) and Ni XVII(dotted).

A similar relationship for the recombination rate can be derived , giving

$$\frac{\alpha_{X,Z+1}(T_1, T_2, a)}{\alpha_{X,Z+1}(T_1)} = 1 + a\gamma_\alpha(T_1, T_2), \quad (6.14)$$

where $\gamma_\alpha$ is defined as

$$\gamma_\alpha(T_1, T_2) = \frac{\alpha_{X,Z}(T_2)}{\alpha_{X,Z}(T_1)} - 1. \quad (6.15)$$

In both cases the mixing ratio of the two components has been separated from the temperature dependence.

The ionization rate is primarily determined by the fraction of the electrons with energy larger than the ionization energy of the ion, so $\gamma_q$ is positive. The recombination rate is primarily determined by $T_1$ since it depends on some inverse power of $T$ (see, e.g., Arnaud and Rothenflug [3]). So, $\gamma_\alpha$ is negative and less than 1. It is small compared to $\gamma_q$ and also varies less, which follows from evaluating Equations (6.12) and (6.15). (That $\gamma_q$ is larger $\gamma_\alpha$ makes physical sense, since $\gamma_q$ is strongly affected by the high temperature component where $\gamma_\alpha$ is only perturbed by the high temperature component.)

With the bi-Maxwellian distribution, Equation (6.7) becomes

$$\frac{N_{X,Z+1}}{N_{X,Z}} = \left(\frac{N_{X,Z+1}}{N_{X,Z}}\right)_{T_1} \frac{q_{X,Z}(T_1,T_2,a)}{q_{X,Z}(T_1)} \times \frac{\alpha_{X,Z+1}(T_1)}{\alpha_{X,Z+1}(T_1,T_2,a)}, \quad (6.16)$$

where

$$\left(\frac{N_{X,Z+1}}{N_{X,Z}}\right)_{T_1} = \frac{q_{X,Z}(T_1)}{\alpha_{X,Z+1}(T_1)}, \quad (6.17)$$

and will be taken from Arnaud and Raymond [2] or Arnaud and Rothenflug [3] at temperature $T_1$. From Equations (6.13) and (6.14), the ratio of the ionization stage densities for the bi-Maxwellian case can be written in terms of the single Maxwellian case as

$$\frac{N_{X,Z+1}}{N_{X,Z}} = \frac{1+a\gamma_q(T_1,T_2)}{1+a\gamma_\alpha(T_1,T_2)} \left(\frac{N_{X,Z+1}}{N_{X,Z}}\right)_{T_1}. \quad (6.18)$$

Since $\mid \gamma_\alpha \mid << \gamma_q$ ($\gamma_\alpha \approx -0.8$, while $\gamma_q > 10$), Equation (6.18) can be written

$$\frac{N_{X,Z+1}}{N_{X,Z}} \Big/ \left(\frac{N_{X,Z+1}}{N_{X,Z}}\right)_{T_1} \approx 1 + a\gamma_q(T_1,T_2). \quad (6.19)$$

The ion densities in Equation (6.19) can be replaced by the spectral line intensities as in

$$\frac{I_{X,Z+1}}{I_{X,Z}} \Big/ \left(\frac{I_{X,Z+1}}{I_{X,Z}}\right)_{T_1} \approx \frac{N_{X,Z+1}}{N_{X,Z}} \Big/ \left(\frac{N_{X,Z+1}}{N_{X,Z}}\right)_{T_1}, \quad (6.20)$$

since to first order the emissivities will cancel. (For example, for Fe XVII/Fe XVI this ratio is incorrect by 6%, using calculations of Brickhouse et al. [7] and an $a = 0.05$).

The line-ratio temperature diagnostic, for which a typical example is shown in Figure 6.3 can often be fitted over a small range of temperature by

$$Log\left(\frac{I_{X,Z+1}}{I_{X,Z}}\right) = C\ Log(T) + D. \quad (6.21)$$

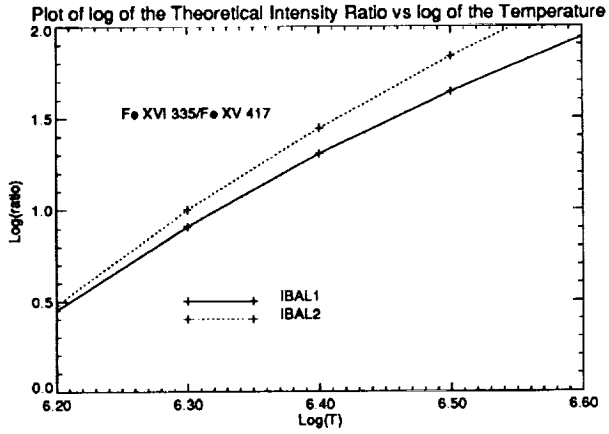


Figure 6.3. The log of the theoretical ratio of intensity of Fe XVI 335Å/Fe XVI 417Å vs. log of the temperature is approximately linear over a broad range of temperature. The plotted curves are given for two sets of ionization balances, as discussed in Section 6.2.

For most cases $C$ depends only on the two ionization stages involved while $D$ depends on both the pair of ionization stages and the particular spectral lines used. Both $C$ and $D$ are determined from theoretical line ratios and assumed not to be dependent on $a$. The effect of the addition of excess high energy electrons is to increase the intensity ratio $\frac{I_{X,Z+1}}{I_{X,Z}}$, so the apparent temperature will also increase. If we subtract Equation (6.21) evaluated with a pure Maxwellian distribution at temperature $T_1$ from Equation (6.21) evaluated with the two-component electron distribution with line-ratio temperature $\overline{T}$, we get

$$Log\left[\frac{I_{X,Z+1}}{I_{X,Z}} \Big/ \left(\frac{I_{X,Z+1}}{I_{X,Z}}\right)_{T_1}\right] = C\,[Log(\overline{T}) - Log(T_1)], \quad (6.22)$$

since $D$ is canceled.

Equations (6.19) and (6.20) can be substituted into Equation (6.22) to produce

$$Log(1+a\gamma_q) \approx C\,[Log(\overline{T}) - Log(T_1)]. \quad (6.23)$$

Next, we use the relationship $Log(x) = Ln(x)/Ln(10)$ and expand $Ln(1+x) \approx x$ for

$x << 1$. For small $a\gamma_q$, we get

$$a\gamma_q / Ln(10) \approx C\,[Log(\overline{T}) - Log(T_1)], \quad (6.24)$$

which can be rewritten as

$$a\beta = [Log(\overline{T}) - Log(T_1)], \quad (6.25)$$

where

$$\beta = \frac{\gamma_q}{C\,Ln(10)}. \quad (6.26)$$

Now $a$ can be determined from two different sets of line-ratio temperatures (since $T_1$ is the same for emission from the same plasma but the measured temperature $T$ will differ depending on $\beta$) by

$$a = \frac{Log(\overline{T_i}) - Log(\overline{T_j})}{\beta_i - \beta_j}, \quad (6.27)$$

where the subscripts $i$ and $j$ indicate the different sets of line ratios.

In Table 6.1, $\beta$ is given for different ionization stages using Equation (6.26) and $C$ is evaluated by fitting the theoretical ratio of intensities as a function of the temperature. In Table 6.2 the $\beta$ of the two iron transitions is subtracted from the $\beta$ for nickel. In both cases the values and the uncertainties were determined for $kT_1 = 190 \pm 20eV$ and $kT_2 = 1000 \pm 200eV$. $T_1$ is chosen to give two distinct components (a larger value for $T_2$ does not significantly alter the result, as will be shown in Figure 6.4). The line-ratio temperatures given in Table 6.3 are determined for both IBAL1 and IBAL2, using the intensities reported by Thomas and Neupert [54]. Then Equation (6.27) is used to determine the mixing ratio. The mixing ratio in all cases is within the uncertainty, and $a$ is consistent with 0 or a small positive number in all cases. The assumption that $Ln(1+a) \approx a$ is invalid for large $a$ and this would cause $a$ to be underestimated by up to a factor of 2. Still, the observations indicate the mixing fraction is less than 0.25.

Multiple temperatures along the line of sight could also produce a similar effect, making the mixing fraction lower. Since a stronger upper limit on the mixing fraction will be determined in Section 6.3 the effect of multiple temperatures along the line of sight was not investigated. The mixing fraction derived from the observed line ratios should be regarded as an upper limit on any bi-Maxwellian distribution.

Table 6.1. Values of Parameter $\beta$

| Lower Stage | Upper Stage | IBAL1 | IBAL2 |
|---|---|---|---|
| Ni XVII | Ni XVIII | $2.58 \pm 1.26$ | $2.58 \pm 1.26$ |
| Fe XV | Fe XVI | $1.57 \pm 0.62$ | $1.38 \pm 0.66$ |
| Fe XVI | Fe XVII | $1.45 \pm 0.63$ | $1.32 \pm 0.53$ |

Notes: $\beta$ and the uncertainty in $\beta$ were determined from assuming $kT_1 = 190 \pm 20eV$, $kT_2 = 1000 \pm 200eV$. IBAL1 and IBAL2 defined in Table 4.1.

In Table 6.1, the $\beta$ for Fe XV/Fe XVI is larger than for Fe XVI/Fe XVII. This occurs because $C$ increases more than $\gamma_q$, so the ratio actually decreases slightly in Equation 6.26. For a given $a$, according to Equation 6.25 the Fe XV/Fe XVI line-ratio temperature would be larger than the Fe XVI/Fe XVII line-ratio temperature, which is counter intuitive. The normal expectation would be that the measured line-ratio temperature from the set of higher ionization levels would be higher. Actually the increase of the observed intensity ratio would be higher but the increase of the line-ratio temperature may be less depending on $C$.

## 6.3 Theoretical Limit

A theoretical upper limit on the mixing fraction $a$ can be determined from the case where the cooling of the high energy electrons is the sole heat source of the corona. Then the total radiative flux emitted by the corona is equal to the energy released from the cooling of the high energy electrons. This should give a reasonable estimate of

Table 6.3. Temperature

| Ratio | IBAL1 | IBAL2 |
|---|---|---|
| Fe XVI 335.400/Fe XV 417.500 | $6.45 \pm 0.09$ | $6.41 \pm 0.07$ |
| Fe XVI 360.800/Fe XV 417.500 | $6.43 \pm 0.09$ | $6.39 \pm 0.07$ |
| Fe XVII 350.500/Fe XVI 335.400 | $6.50 \pm 0.07$ | $6.37 \pm 0.05$ |
| Fe XVII 350.500/Fe XVI 360.800 | $6.52 \pm 0.08$ | $6.38 \pm 0.06$ |
| Ni XVIII 292.000/Ni XVII 249.200 | $6.45 \pm 0.14$ | $6.45 \pm 0.14$ |

Notes: The line-ratio temperatures were calculated using the intensities given by Thomas and Neupert [54], assuming Landini and Monsignori-Fossi [41] emissivities. The uncertainties includes the fitting uncertainty, and the instrument uncertainty described by Thomas and Neupert. The uncertainty also includes the ionization balance uncertainty and the emissivity uncertainty.

Table 6.4. Mixing Fraction, $a$

| Ratio | IBAL1 | IBAL2 |
|---|---|---|
| Fe XVI 335.400/Fe XV 417.500 | $0.00 \pm 0.16$ | $0.03 \pm 0.13$ |
| Fe XVI 360.800/Fe XV 417.500 | $0.02 \pm 0.16$ | $0.05 \pm 0.14$ |
| Fe XVII 350.500/Fe XVI 335.400 | $-0.04 \pm 0.14$ | $0.06 \pm 0.12$ |
| Fe XVII 350.500/Fe XVI 360.800 | $-0.06 \pm 0.15$ | $0.06 \pm 0.12$ |

Table 6.2. Values of Parameter $(\beta_{Ni} - \beta_{Fe})$

| Lower Stages | Upper Stages | $\beta_{Ni} - \beta_{Fe}$ IBAL1 | IBAL2 |
|---|---|---|---|
| Fe XV | Fe XVI | $1.02 \pm 0.64$ | $1.20 \pm 0.71$ |
| Fe XVI | Fe XVII | $1.13 \pm 0.64$ | $1.26 \pm 0.68$ |

Notes: The uncertainties in the difference in $\beta$ were determined assuming $kT_1 = 190 \pm 20eV$, $kT_2 = 1000 \pm 200eV$. (The uncertainty is less than would be determined by taking the square root of the sum of the squared uncertainties in Table 6.1 since they are not independent.)

the mixing fraction if conduction, which is neglected, is not too important and if the plasma is in a steady state.

The time for equipartition for two sets of Maxwellian particles with different temperatures is given by Spitzer (1961) [51] as

$$t_{eq} = 5.87 \frac{A_1 A_2}{N_1 Z_1^2 Z_2^2 ln(\Lambda)} \left( \frac{T_1}{A_1} + \frac{T_2}{A_2} \right)^{1.5} sec, \tag{6.28}$$

where $\Lambda$ is the ratio of the Debye shielding distance to the impact parameter, $T_i$ is the temperature of distribution $i$, $A_i$ is the atomic mass of the particles of group $i$ and $N_1$ is the bulk plasma density. For the case where both sets of particles are electrons and

$$N_1 = N_e(1 - a), \tag{6.29}$$

we get

$$t_{eq} = 5.87 \frac{A^{0.5}}{N_1 ln(\Lambda)} (T_1 + T_2)^{1.5} sec. \tag{6.30}$$

(For electrons with $N_1 = 10^9 cm^{-3}$, $T_1 = 2 \times 10^6 K$, and $T_2 = 10^7 K$ we get $t_{eq} \approx 0.3 sec.$) We take $T_2$ and $N_2$ to be the temperature and density of the high-temperature component and use

$$N_2 = N_e a. \tag{6.31}$$

Then the exponential decay rate is

$$\tau = t_{eq}(1 - a) \tag{6.32}$$

if $T_1$ and $N_1 T_1 + N_2 T_2$ are constant (steady state).

Each electron which is transferred from the high-temperature component to the low-temperature component would release an amount of energy given by $k(T_2 - T_1)$. Thus, the total heating of the bulk plasma in steady state would be

$$F_h = \frac{k(T_2 - T_1)N_2}{\tau}. \tag{6.33}$$

Substituting Equations (6.30) and (6.32) in Equation (6.33) we get

$$F_h = \frac{k(T_2 - T_1)N_1 N_2 \, ln(\Lambda)}{5.87 A^{0.5}(T_1 + T_2)^{1.5}(1 - a)}. \tag{6.34}$$

Replacing $N_1$ and $N_2$ in Equation (6.34) then gives

$$F_h = \frac{k(T_2 - T_1)N_e^2 a \, ln(\Lambda)}{5.87 A^{0.5}(T_1 + T_2)^{1.5}}. \tag{6.35}$$

The radiative flux, discussed in Section 5.2, is given by

$$F_r = \varepsilon N_e^2. \tag{6.36}$$

Where the plasma emissivity is primarily dependent on the bulk plasma temperature $T_1$. If equilibrium exists and conduction is not important, then heating for the high-energy electrons needs to be equal to or less than the radiative flux. So an upper limit on the mixing fraction, $a$, can be determined, by setting $F_h \geq F_r$ yielding

$$\varepsilon N_e^2 \geq \frac{k(T_2 - T_1)N_e^2 a \, ln(\Lambda)}{5.87 A^{0.5}(T_1 + T_2)^{1.5}}, \tag{6.37}$$

or

$$\varepsilon \geq \frac{k(T_2 - T_1) a \, ln(\Lambda)}{5.87 A^{0.5}(T_1 + T_2)^{1.5}}, \tag{6.38}$$

which can be rearranged as

$$a \leq \frac{5.87 \varepsilon A^{0.5}(T_1 + T_2)^{1.5}}{ln(\Lambda) k(T_2 - T_1)}. \tag{6.39}$$

For coronal conditions $ln(\Lambda)$ is nearly constant. According to tables in Spitzer (1961) on pg 128 [51], $ln(\Lambda) = 19.3$ for $T = 10^6 K$ and $N_e = 10^9/cm^3$. Cook [9] gives $\varepsilon = 2.35 \times 10^{-23} erg \ cm^3$ for $log(T) = 6.4$, and $\varepsilon = 6.735 \times 10^{-23} erg \ cm^3$ for $log(T) = 6.3$, using Meyer 1985 [37] elemental abundances. (If Meyer 1992 [40] composition is used, then the emissivities, and consequently the upper limits on $a$, will increase by roughly a factor of 3.5.) Thus, using Meyer 1985, for $log(T_1) = 6.4$, we get

$$a = \frac{1.21 \times 10^{-9}(T_1 + T_2)^{1.5}}{T_2 - T_1}; \tag{6.40}$$

and, for $log(T_1) = 6.3$,

$$a = \frac{3.46 \times 10^{-9}(T_1 + T_2)^{1.5}}{T_2 - T_1}. \tag{6.41}$$

Both curves for $a$ are plotted in Figure 6.4 versus $T_2$. As can be seen in the figure, for $T_2 > 10^7 K$ the upper limit on the mixing fraction is relatively flat. Any additional heating mechanism would cause $a$ to be smaller. If heat conduction is included the upper limit could be increased by about a factor of 2, but it will still be small for the steady state case

The theoretical upper limit on $a$ of less than $10^{-5}$ does indicate that the previous results Maxwellian assumption is reasonable for Chapters 2, 4 and 5. With a typical $\beta$ of 20 the temperature changes by less than one tenth of a percent, which is small compared to the other errors.

Since the upper limit on $a$ is small, trying to observe it will be extremely difficult experimentally. The best possibility will be to look at the ratio of intensities between helium-like ionization stages and hydrogen-like ionization stages where the ionization energy is high. For example Si XIII is helium like and has an ionization energy

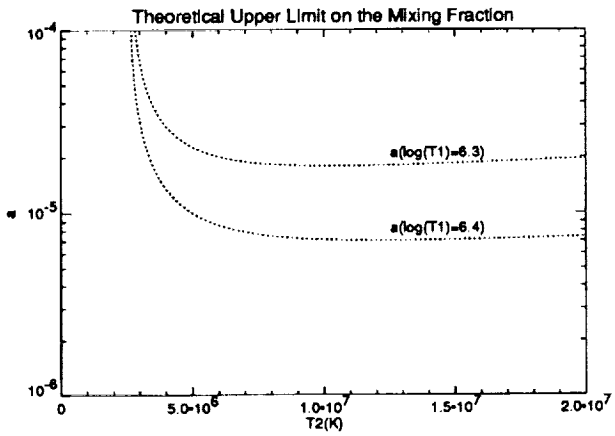


Figure 6.4. The upper limits on $a$ as a function of $T_2$ for $log(T_1) = 6.3$ and $log(T_1) = 6.4$ are shown. This assumes that heating done by the high-temperature component is radiated away with no other heat source, and that conduction is negligible

of 523.52 eV, while Si XIV has an ionization energy of 2437.76 eV according to Cowan [10]. According to Arnaud and Rothenflug [3] $10^{-0.24}$ of the silicon should be Si XIII while $10^{-5.97}$ should be Si XIV. Both have spectral lines between 4-7Å. Using $kT_1 = 190eV$ and $kT_2 = 1000eV$ the amount of Si XIV will double for an $a = 10^{-3}$. This effect will increase for elements with higher Z elements. In the case of S XV and S XVI the effect will be similar for $a = 10^{-4}$. For lower Z elements such as Ne IX to Ne X, an $a = 0.1$ will approximately double the amount of Ne X. The effect of $a$ is stronger on the higher Z elements, at any given temperature $T_1$. The trouble is that often the hydrogen-like lines are very weak compared to the helium-like lines and will be hard to detect. Any significant quantity of $10^7K$ plasma along the line of sight would make the analysis impossible, since it will be the stronger emitter of the Si XIV and S XVI spectral lines.

# Chapter 7

# Conclusions

## 7.1 Relative Elemental Abundances

The present understanding of coronal elemental abundance is discussed in Section 2.2. In Section 4.6 the set of relative elemental abundances for silicon, aluminum, chromium, and iron was determined. The relative elemental abundance for silicon to iron for SERTS 1989 using IBAL1 agrees within uncertainties with either photospheric (Allen [1]) or coronal elemental abundances given by Meyer [38, 40].

However, The relative elemental abundance for SERTS 1991 differs from elemental abundances given in the literature for both photospheric and coronal elemental abundances. For SERTS 1991, the lower the First Ionization Potential (FIP) of the element the larger the enhancement of the element compared to photospheric or coronal abundances. A tilt in the upper level of the step function in Figure 2.1 would explain this result.

The differences between SERTS 1989 and SERTS 1991 sets of elemental abundances indicate that the solar coronal elemental abundance can vary. A simple step function would not explain all solar coronal conditions. Both Saba and Strong [48] and McKenzie and Feldman [34] reported variations in the relative elemental abundances for low FIP elements (Section 2.2). Additional observations might determine how best to model the coronal elemental abundance.

The difference in the SERTS 1989 and 1991 elemental abundance is real. The Si XI 303Å, Fe XVI 361Å, and the Fe XIV 334Å spectral lines were used for both flights. The measured line-ratio temperatures were similar. Any change in the ionization balance calculations would change the Fe to Si abundance for both flights by similar amounts. The difference in relative elemental abundance between the two flights would still remain.

The most likely explanation would be that the observed regions of the solar corona were different. Both were observed off the solar limb. Both were quiet solar regions with some active regions near the line of sight. The primary difference between the two flights was that for SERTS 1991 the emission measure was a factor of ten times larger than for SERTS 1989, a hot loop was nearby, and the Sun was more active near the line of sight. The two flights were 2 years apart so temporal variations of coronal abundances could also explain the result.

## 7.2 Radial Dependence of Coronal Parameters

The three observation sites examined in this dissertation all have line-ratio temperatures which increase with height, where as the line-ratio densities, emission measures, and spectral line intensities decrease with height above 1.03 $R_{\odot}$. The decrease of the emission measure is roughly exponential. The line-ratio temperature increase appears to be linear, with any second-order depen-

dence being smaller than the uncertainty in the measurement of its dependence. These smoothly varying radial dependencies allowed the use of simple coronal models with spherical symmetry.

The line-ratio temperatures and scale-height temperatures agree to within approximately 25% (Table 4.6). The scale-height temperature was derived from the radial dependence of the intensity. The line-ratio temperature was determined from the ratio of the intensities of different spectral lines. These two temperature measurements were nearly independent. Since the line-ratio temperature requires fewer assumptions and can be used to determine the radial temperature dependence, it is the preferred method for determining the coronal temperature. Reliable determination of the line-ratio temperature requires many spectral lines from different ionization stages of the same element, where none of the lines is strongly affected by resonance scattering.

## 7.3 Heating

In all cases, the line-ratio temperature increases with height. To supply the heat which would be conducted downward due to the temperature gradient and radiation, a source of heat is required at some location above the maximum observed height (1.15 $R_\odot$ for SERTS 1989 and 1.2 $R_\odot$ for SERTS 1991).

The maximum divergence of heat flux was determined from the radial dependence of the temperature. The total radiative power was obtained from the emission measure and line-ratio temperature (Section 5.2). By comparing the divergence of heat flux and the total radiative power, for a filling factor of 1.0, heating was shown to be necessary for two of the three cases over some of the region below 1.15 $R_\odot$, with the third case being inconclusive. For a filling factor of 0.1, heating is necessary for all three cases over the entire region observed.

## 7.4 Bi-Maxwellian

For a bi-Maxwellian electron distribution to affect the ionization balance, we have shown (Section 6.3) that, under steady-state conditions, the mixing fraction must greatly exceed the value of $2 \times 10^{-5}$ that we determined to be an upper limit for the corona, assuming that the cooling of high energy electrons is the sole source of energy radiated away. Therefore, any bi-Maxwellian mixing fraction that can exist under solar coronal steady-state conditions will not affect the ionization balance.

# Chapter 8

# Future Applications of SERTS and SOHO

## 8.1 SERTS

Additional off-the-limb SERTS observations are highly desirable for the study of the coronal elemental abundances and heating requirements. Use of a narrower lobe (because there would be fewer overlapping emission lines) should increase the number of usable lines on both sides of the lobe. Additional iron spectral lines from different stages of ionization should lead to a better determination of the temperature or temperature profile along the line of sight. This would allow stronger constraints to be placed on heating. Additional spectral lines from different elements would allow better determination of the relative elemental abundances.

Joint observations from Yohkoh and other space platforms would allow a more extensive analysis of coronal temperature structure and composition. The Yohkoh satellite observes hotter plasma along the line of sight. Coronagraph measurements would allow large-scale coronal structures to be studied.

## 8.2 SOHO CDS/NIS

The type of analysis done in this dissertation could also be applied to data obtained from the planned SOHO satellite (Solar and Heliospheric Observatory). For example, using the 4 by 240 arcsec slit of the SOHO CDS/NIS instrument (Coronal Diagnostic Spectrometer/Normal Incidence Spectrometer), and rastering the slit off the limb to form images from a number of spectral lines, would provide a useful data set for this kind of analysis. The 4 by 240 slit would have a resolution of 0.168 Å, which is larger than the SERTS narrow slit, and is smaller than the lobes. Therefore, more lines would be usable than were used in this study. This would allow better determinations of emission measure, density, and temperature. These results would allow the determination of the relative elemental abundances and imposing of further heating constraints.

The addition of more spectral lines would allow a differential emission measure to be determined. A differential emission measure determines the emission measure distribution over a range of temperatures by using emissivity of the different spectral lines as a function of temperature, and finding the best overall fit to the data. This was not done for this dissertation, because there were insufficient resolvable lines from the same element to give a well constrained result. For the cases studied, an uniform temperature gave a reasonable fit to the data.

# Appendix A

# Solar Plasma Parameters

| Region | Temperature | Density | $H_s$ | $\omega_p$ |
|---|---|---|---|---|
| Photosphere | 6,000K | $10^{16} cm^{-3}$ | 300km | $2\pi \times 10^{12} Hz$ |
| Chromosphere | $10^4 K$ | $10^{11} cm^{-3}$ | 500km | $6\pi \times 10^9 Hz$ |
| Corona | $2 \times 10^6 K$ | $10^9 cm^{-3}$ | 90,000km | $6\pi \times 10^8 Hz$ |

Useful Equations

Plasma Frequency, $\omega_p = \left(\frac{4\pi N_e e^2}{m}\right)^{0.5} \approx 10^4 N^{0.5} (rad/sec)$

Mean-Free-Path for fully ionized plasma, $\lambda_{mfp} \approx 3.8 \times 10^9 \frac{W(ev)^2}{N}\ m$

Hydrostatic Scale Height, $H_s \approx \frac{T}{1.4 \times 10^7 K} R_\odot$

Temperature $10^4 K \approx 1\ eV$

Time for Equipartition for Two Sets of Maxwellian Particles with Different Temperatures (Equation 6.28)

$$t_{eq} = 5.87 \frac{A_1 A_2}{N_1 Z_1^2 Z_2^2 ln(\Lambda)} \left(\frac{T_1}{A_1} + \frac{T_2}{A_2}\right)^{1.5} sec, \tag{A.1}$$

Example $N_1 = 10^9 cm^{-3}$, $T_1 = 2 \times 10^6 K$, and $T_2 = 10^7 K$

For Electrons ($t_{eq} \approx 0.3 sec$)

For Protons ($t_{eq} \approx 10 sec$)

For Protons ($T_1$) and Electrons ($T_2$) ($t_{eq} \approx 10 minutes$)

# Glossary of Symbols

| Symbol | Description | Page First used in |
|---|---|---|
| $A$ | Area | 9 |
| $A_i$ | Mass of particle $i$ in amu | 76 |
| $a$ | 2nd fitting parameter for line-ratio temperature | 41 |
| $C$ | Correction factor from line intensity equation | 17 |
| $F(E,T_1)$ | Maxwellian Electron Distribution | 72 |
| $F_c$ | Electron heat conduction | 66 |
| $F_c'$ | Divergence of the heat conduction | 66 |
| $F_h$ | total heating Flux | 77 |
| $F_o$ | Constant part of the divergence of the heat conduction | 66 |
| $F_r$ | Radiative power | 66 |
| $F_t$ | Electron Distribution | 72 |
| $G$ | Universal constant of gravity ($6.67 \times 10^{-8} dyn\ cm^2\ g^{-2}$) | 9 |
| $g$ | Acceleration due to gravity | 9 |
| $H_{os}$ | Observed density scale height | 21 |
| $H_s$ | Density scale height | 10 |
| $H_s'$ | Effective density scale height | 10 |
| $k$ | Boltzmann constant($8.617 \times 10^{-5} eV\ K^{-1}$) | 10 |
| $M_\odot$ | Solar mass ($1.989 \times 10^{33}$ gm) | 9 |
| $N_e$ | Electron density | 10 |
| $\overline{N_e^2}$ | Average of the electron density squared | 17 |
| $N_i$ | Density of Particle Distribution $i$ | 76 |
| $P$ | Pressure | 9 |
| $R_\odot$ | Solar Radius ($6.9599 \times 10^{10}$ cm) | 10 |
| $r$ | Radius (distance from Sun Center) | 9 |
| $r_o$ | Reference radius (Section 2.1.1) | 10 |
| $r'$ | Line-of-sight radius | 17 |
| $T$ | Temperature | 10 |
| $T_e$ | Electron temperature | 13 |
| $T_i$ | Temperature of Particle Distribution $i$ | 76 |
| $T_o$ | 1st fitting parameter for line-ratio temperature | 20 |
| $t_{eq}$ | time for equipartition | 76 |
| $y$ | $(\frac{1}{r_o} - \frac{1}{r'})$ | 21 |
| $z$ | Length along the magnetic field line | 66 |
| $Z_i$ | number of protons of Participle i | 76 |

| Symbol | Description | Page First used in |
|---|---|---|
| $\gamma_q$ | Correction Term for Ionization Rate | 73 |
| $\gamma_\alpha$ | Correction Term for Recombination Rate | 73 |
| $\varepsilon_T$ | Total plasma emissivity | 66 |
| $\zeta$ | Correction factor from line intensity equation | 17 |
| $\Lambda$ | the ratio of the Debye shielding distance to the impact parameter | 76 |
| $\lambda_{mfp}$ | Mean Free Path | 71 |
| $\mu$ | Average atomic weight | 10 |
| $\rho$ | Mass density of the gas | 9 |
| $\beta$ | Conversion Factor | |
| $I_{X,Z}$ | Spectral line intensity | |

(Following symbols are defined along line of sight)

| Symbol | Description | Page First used in |
|---|---|---|
| $f$ | Filling factor | 17 |
| $L$ | Effective line-of-sight length | 17 |
| $\overline{N_e}$ | Line-of-sight density | 16 |
| $\overline{Q_{X,Z,i,j}}$ | Density weighted average contribution function | 16 |
| $\overline{T_e}$ | Line-of-sight temperature | 16 |
| $x$ | Path length along the line of sight | 16 |
| $\eta$ | Column emission measure | 17 |

For the following, $X$=element, $Z$=ionization stage,
$i$ is an excitation level, and $j$ is a second excitation level

(Following symbols are defined along line of sight)

| Symbol | Description | Page First used in |
|---|---|---|
| $A_{X,Z,i,j}$ | Einstein spontaneous emission rate | 13 |
| $b_{X,Z,i,j}$ | Branching ratio | 15 |
| $C_{i,j}$ | Electron collision excitation rate ($j > i$) | 14 |
| $C_{j,i}$ | Collision de-excitation rate ($j > i$) | 14 |
| $E_{X,Z,i}$ | Energy of an excitation level | 14 |
| $E_{X,Z,i,j}$ | Energy per photon | 13 |
| $I_{X,Z,i,j}$ | Spectral line intensity | 15 |
| $N_{X,Z,i}$ | Density | 13 |
| $q_{X,Z}$ | Ionization rate coefficient | 15 |
| $Q_{X,Z,i,j}$ | Contribution function for a spectral line | 13 |
| $\alpha_{X,Z}$ | Radiative recombination rate coefficient | 15 |
| $\overline{\gamma_{ji}}$ | Effective collision strength | 14 |
| $\epsilon_{X,Z,i,j}$ | Emission per unit volume | 13 |
| $\omega_j$ | Statistical weight for level $j$ | 14 |

NOTES:
dummy indices not listed

The general notation used to indicate the spectral line or atomic energy level in question needs to be introduced. Since this thesis compares lines from different elements, ionization stages, levels of excitation, and solar radial positions, the notation needs up to four subscripts. An example of the notation is given by $E_{Fe,XV,5,1}$, where $E$ indicates the energy per photon, Fe is the element, XV is the ionization stage, 5 denotes the initial level and 1 the ground state too which the ion de-excites. The general case of an arbitrary emission line produced by an arbitrary transition in an arbitrary element would be written $E_{X,Z,i,j}$ where $X$ is the element and $Z$ is the ionization stage. Densities are specified with three subscripts or less, for example with $N_{Fe,XV,5}$ indicating the volume density of Fe XV in the fifth excitation level. The density of an element in a particular ionization stage, summed over all excitation levels will be $N_{X,Z}$, where

$$N_{X,Z} = \sum_j N_{X,Z,j}. \tag{A.2}$$

Finally radial position is denoted in the common way as an argument in parenthesis. For example $N_X(r)$ is the volume density of element X at radius r.

(Following symbols are defined along line of sight)

| Symbol | Description | Page First used in |
|---|---|---|
| | Different | |
| $Q_{X,Z}$ | Ionization Cross Section | 73 |
| $E$ | Kinetic Energy of the Particle | 71 |
| $a$ | Mixing Fraction | 72 |
| $C$ | Fitting Parameters | 72 |
| $D$ | Fitting Parameters | 72 |
| $\overline{(T_i)}$ | Measured Line-ratio temperature of line-ratio $i$ | 74 |

# Bibliography


[1] Allen, C.W., 1973 *Astrophysical Quantities*, The Athlone Press, University of London.

[2] Arnaud, M., and J. Raymond, 1992, *Ap.J.*, 398, p. 394.

[3] Arnaud, M., and R. Rothenflug, 1985, *Astr. & Ap. Suppl.*, 60, pp. 427-457.

[4] Arnaud, M., 1994, private communication.

[5] Ayres, T.R., and L. Testerman, 1981, *Ap.J.*, 245, p. 1124.

[6] Bhatia, A.K., 1992-1994, private communication.

[7] Brickhouse, N.S., J.C. Raymond, and B.W. Smith to be published.

[8] Brosius, J.W., J.M. Davila, W.T. Thompson, R.J. Thomas, G.D. Holman, N. Gopalswamy, S.M. White, M.R. Kundu and H.P. Jones, 1993, *Ap.J.*, 411, pp. 310-417.

[9] Cook, J.W., C.-C. Chenh, V.L. Jacobs and S.K. Antiochos, 1989, *Ap.J.*, 338, pp. 1176-1183.

[10] Cowan, R.D., 1981, *Theory of Atomic Structure and Spectra*, University of California Press, Berkeley.

[11] Crannell, C.J., 1987, In *Encyclopedia of Physical Science and Technology* **12**, Ed. Robert A.Meyers, Academic Press, pp. 782-792.

[12] Davila, J.M., 1985, *Ap.J.*, 291, p. 328.

[13] Davila, J.M., 1994, private communication.

[14] Doschek, G.A., 1985 *Autoionization*, Ed. A. Temkin Plenum Press: New York, pp. 171-257.

[15] Doschek, G.A., U. Feldman and J.F. Seely, 1985, *M.N.R.A.S.*, 217, p. 317.

[16] Feldman, U., and K.G. Widing, 1990, *Ap.J.*, 363, p. 292.

[17] Feldman, U., 1992, *Physica Scripta*, 46, pp. 202-220.

[18] Feldman, U., 1994, private communication.

[19] Fludra, A., and J.T. Schmelz, 1994, submitted.

[20] Fontenla, J.M., E.H. Averett and R. Loeser, 1993, *Ap.J.*, 406, pp. 319-345.

[21] Fuhr, J.R., G.A. Martin and W.L. Wiese, 1988, *Journal of Physical and Chemical Reference Data*, 17 no 4, pp. 194-214 (1988).

[22] Gabriel, A.H., 1971, *Solar Physics*, 21, pp. 392-400.

[23] Gabriel, A.H., and Carole Jordan, 1972, eds E.W.Mcdaniel and M.R.C. Mcdowell *Case Studes in Atomic Collision Physics II* (North-Holland Publishing Company-Amsterdam).

[24] Giovanelli, R., 1984, *Secrets of the Sun*, Cambridge University Press.

[25] Guhathakurta, M., G.J. Rottman, R.R. Fisher, F.Q. Orrall and R.C. Altrock, 1992, *Ap.J.*, 388, pp. 633-643.

[26] Hedin, A.E., 1987, *JGR*, 92, p. 4649.

[27] Ionson, J.A., 1982, *Ap.J.*, 254, p. 318.

[28] Kato, T., 1976, *Ap.J. Suppl.*, 30, pp. 397-449.

[29] Keenan, F.P., 1992, *Newsletter on Analysis of Astronomical Spectra*, 17, p. 9.

[30] Kelly, R.L., 1987, *J.Phys & Chem. Ref. Data Suppl.*, 16 no 1, p. 1371.

[31] Krall, N.A., and A.W. Trivelpiece, 1986, *Principles of Plasma Physics*, San Francisco Press, San Francisco.

[32] Kundu, M.R., 1965, *Solar Radio Astronomy*, Interscience, New York.

[33] Landini, M., and B.C. Monsignori-Fossi, 1990, *Astron. & Ap.*, 82, pp. 229-260.

[34] McKenzie, D.L., and U. Feldman, 1992, *Ap.J.*, 389, pp. 764-776.

[35] Mewe, R., E.H.B.M. Gronenschild and G.H.J. Van den Oord, 1985, *Astr. & Ap. Suppl.*, 62, pp. 197-254.

[36] Martin, G.A., J.R. Fuhr and W.L. Wiese, 1988, *Journal of Physical and Chemical Reference Data*, 17 no 3, p. 370.

[37] Meyer, Jean-Paul, 1985, *Ap. J. Suppl.*, 57, pp. 151-171.

[38] Meyer, Jean-Paul, 1985, *Ap. J. Suppl.*, 57, pp. 173-204.

[39] Meyer, Jean-Paul, 1993, *Advances in Space Research*, 13 no 9, pp. 377-390.

[40] Meyer, Jean-Paul, 1993-1994, Private communication.

[41] Monsignori-Fossi, B.C., 1993-1994, private communication.

[42] Nakada, M.P., R.D. Chapman, W.M. Neupert and R.J. Thomas, 1975 *Solar Physics*, 43, pp. 337-350.

[43] Neupert, W.M., G.L. Epstein, R.J. Thomas and W.T. Thompson, 1992, *Sol. Phys.*, 137, p. 87.

[44] Parker, E.N., 1974, *Solar Physics*, 37, p. 127.

[45] Parker, E.N., 1985, *Solar Physics*, 100, p. 599.

[46] Phillips, K.J.H., and U. Feldman, 1991, *Ap.J.*, 379, p. 401.

[47] Raymond, J., 1994, private communication.

[48] Saba, J.L.R., and K.T. Strong, 1993, *Advances in Space Research*, no 9, pp. 391-399.

[49] Sakuri, T., 1982, *Sol. Phys.*, 76, p. 301.

[50] Schmelz, J.T., 1993, *Ap.J.*, 408, pp. 373-381.

[51] Spitzer, Lyman Jr., 1962, *Physics of Fully Ionized Gases*, Interscience Publishers: New York.

[52] Stix, M., 1989, *The Sun*, Springer-verlag, Berlin, ch 4-5.

[53] Stone, E.C., 1989, "Cosmic Abundance of Matter", *AIP Conference Proceedings 183, ed C.Jake Waddington*, American Institute of Physics:New York, p. 72.

[54] Thomas, R.J., and W.M. Neupert, 1994, *Ap. J. Suppl.*, 91, pp. 461-482.

[55] Thomas, R.J., R.A.M. Keski-Kuha, W.M. Neupert, C.E. Condor and J.S. Gum, 1991, *Appl. Opt.*, 30, p. 2245.

[56] Thompson, W.T., W.M. Neupert, S.D. Jordan, H.R. Jones, R.J. Thomas and B. Schmieder, 1993, *Solar Physics*, 147, pp. 29-46.

[57] Ulmschneider, P., E.R. Priest, R. Rosner Eds., 1991, "Mechanisms of Chromospheric and Coronal Heating," *Proceedings of International Conference,* Springer-Verlag:New York.

[58] Veck, N.J., and J.H. Parkson, 1981, *M.N.R.A.S.*, 197, p. 41.

[59] Widing, K.G., and U. Feldman, 1989, *Ap.J.*, 344, p. 1046.

[60] Widing, K.G., and U. Feldman, 1992, *Ap.J.*, 392, p. 715.

[61] Wiese, W.L., M.W. Smith and B.M. Miles, 1969, *Atomic Transition Probabilities Vol II Sodium through Calcium*, National Bureau of Standards: Washington D.C..

[62] Zirker, J.B., 1993, *Solar Phys.*, 148, p. 43.

[63] Zirin, H., 1988, *Astrophysics of the Sun*, Cambridge University Press, Cambridge.

[64] Solar-Geophysical Data, 538 part 1, 84, June 1989. U.S. Department of Commerce, (Boulder, Colorado, U.S.A. 80303).

[65] Solar-Geophysical Data, 539 part 1, 63-67, July 1989. U.S. Department of Commerce, (Boulder, Colorado, U.S.A. 80303).

[66] Solar-Geophysical Data, 563 part 1, 62-68. July 1991. U.S. Department of Commerce, (Boulder, Colorado, U.S.A. 80303).

# REPORT DOCUMENTATION PAGE

Form Approved
OMB No. 0704-0188



| 1. AGENCY USE ONLY *(Leave blank)* | 2. REPORT DATE | 3. REPORT TYPE AND DATES COVERED |
|---|---|---|
| | December 1994 | Technical Memorandum |

**4. TITLE AND SUBTITLE**

Relative Elemental Abundance and Heating Constraints Determined for the Solar Corona From SERTS Measurement

**5. FUNDING NUMBERS**

Grant # 879-11-38
Grant # 170-38-52

**6. AUTHOR(S)**

David A. Falconer

**7. PERFORMING ORGANIZATION NAME(S) AND ADDRESS (ES)**

Goddard Space Flight Center
Greenbelt, Maryland 20771

**8. PEFORMING ORGANIZATION REPORT NUMBER**

95B00027

**9. SPONSORING / MONITORING ADGENCY NAME(S) AND ADDRESS (ES)**

National Aeronautics and Space Administration
Washington, DC 20546-0001

**10. SPONSORING / MONITORING ADGENCY REPORT NUMBER**

NASA TM-104616

**11. SUPPLEMENTARY NOTES**

Falconer: Universities Space Research Association, Greenbelt, Maryland;
(Under the direction of Joseph Davila, Goddard Space Flight Center, Greenbelt, Maryland)

**12a. DISTRIBUTION / AVAILABILITY STATMENT**

Unclassified - Unlimited
Subject Category 92

Availability: NASA CASI (301)621-0390.

**12b. DISTRIBUTION CODE**

**13. ABSTRACT** *(Maximum 200 words)*

Intensities of EUV spectral lines were measured as a function of radius off the solar limb by two flights of Goddard's Solar EUV Rocket Telescope and Spectrograph (SERTS) for three quiet sun regions. The density scale height, line-ratio densities, line-ratio temperatures, and emission measures were determined. The line-ratio temperature determined from the ionization balances of Arnaud and Rothenflug (1985) were more self-consistent than the line-ratio temperatures obtained from the values of Arnaud and Raymond (1992). Limits on the filling factor were determined from the emission measure and the line-ratio densities for all three regions.

The relative abundances of silicon, aluminum, and chromium to iron were determined. Results did agree with standard coronal relative elemental abundances for one observation, but did not agree for another. Aluminum was overabundant, while silicon was underabundant.

Heating was required above 1.15 solar radii for all three regions studied. For two regions, local non-conductive heating is needed for any filling factor, and in all three regions for filling factor of 0.1.

**14. SUBJECT TERMS**

Solar Corona, Relative Elemental Abundance, Coronal Heating, Filling Factor, EUV, Spectroscopy, Plasma

**15. NUMBER OF PAGES**

106

**16. PRICE CODE**

| 17. SECURITY CLASSIFICATION OF REPORT | 18. SECURITY CLASSIFICATION OF THIS PAGE | 19. SECURITY CLASSIFICATION OF ABSTRACT | 20. LIMITATION OF ABSTRACT |
|---|---|---|---|
| Unclassified | Unclassified | Unclassified | UL |



END DATE FILMED - MAR 1, 1995